NEAR-INFRARED CHARACTERIZATION OF THE ATMOSPHERES OF ALIEN WORLDS

by

Bryce Croll

A thesis submitted in conformity with the requirements
for the degree of Doctor of Philosophy
Graduate Department of Astronomy and Astrophysics
University of Toronto

Abstract

Near-infrared Characterization of the Atmospheres of Alien Worlds

Bryce Croll

Doctor of Philosophy

Graduate Department of Astronomy and Astrophysics

University of Toronto

2011

In this thesis I present near-infrared detections of the thermal emission of a number of hot Jupiters and likely transit depth differences from different wavelength observations of a super-Earth. I have pioneered "Staring Mode" using the Wide-field Infrared Camera on the Canada-France-Hawaii Telescope to achieve the most accurate photometry to-date in the near-infrared from the ground. I also discuss avenues that should allow one to achieve even more accurate photometry in the future. Using WIRCam on CFHT my collaborators and I have detected the thermal emission of the following hot Jupiters: TrES-2b and TrES-3b in Ks-band, WASP-12b in the J, H & Ks-bands, and WASP-3b in the Ks-band on two occasions. Near-infrared detections of the thermal emission of hot Jupiters are important, because the majority of these planets' blackbodies peak in this wavelength range; near-infrared detections allow us to obtain the most model-independent constraints on these planets' atmospheric characteristics, their temperature-pressure profiles with depth and an estimate of their bolometric luminosities. With these detections we are able to answer such questions as: how efficiently these planets redistribute heat to their nightsides, if they're being inflated by tidal heating, whether there's any evidence that one of these planets is precessing, and whether another experiences extreme weather and violent storms?

My collaborators and I have also observed several transits of the super-Earth GJ 1214b. We find a deeper transit depth in one of our near-infrared bands than the other. This is likely indicative of a spectral absorption feature. For the differences in the transit depth to be as large as we observed, the atmosphere of GJ 1214b must have a large scale height, low mean molecular weight and thus have a hydrogen/helium dominated atmosphere. Given that other researchers have not found similar transit depth differences, we also discuss the most likely atmospheric

makeup for this planet that results from a combination of all the observations to date.

Lastly, by searching for long-term linear trends in radial velocity data, I constrain the theory that most hot Jupiters migrated to their present positions via the Kozai mechanism with tidal heating.

Acknowledgements

When it came time to write my thesis, the prospect of writing the dedication and acknowledgements was the most intimidating part. I read these sections from the theses of a number of my peers, and something about their unabashedly sanguine tone – without mentioning the adversity – did not ring true to me. These last five years have been a series of long, difficult, even occasionally unpleasant, and often solitary slogs. Ultimately though, it is these challenges, and the sacrifices that have been necessary to confront them head-on, that has made this process worthwhile; after all, we do these things "not because they are easy, but because they are hard." In between these slogs, I've had a great deal of fun, and in quiet moments of reflection it is the successes that have resulted from overcoming these hardships that I'll cherish and that have made my time in Toronto so rewarding.

My parents and family are not scientists, but they have nonetheless taught me an immeasurable number of life lessons that are reflected in these pages. A classic example is one of the lessons from what I refer to as the "The Four Rules of Dad." I'm not sure that these are the messages that my Father would be aware that I have taken away from our time together, but they are nonetheless the lessons that I've taken to heart. At least one of these "Rules of Dad" is unprintable, but one that isn't is: "If you are going to do a job, then do it right." It is perhaps a slightly less eloquent version of Dr. Martin Luther King, Jr.'s: "If a man is called to be a street sweeper, he should sweep streets even as Michelangelo painted, or Beethoven composed music, or Shakespeare wrote poetry. He should sweep streets so well that all the hosts of heaven and earth will pause to say, here lived a great street sweeper who did his job well." This thesis, and my efforts over the past five years, have been my earnest attempt to honour that fine tradition bequeathed to me by my Father and my Family.

Both of my thesis advisors deserve my considerable gratitude for assisting me on this journey over these past five years. I would like to thank Norman Murray for always having five minutes (that often turned into half-an-hour), even on Saturday and Sunday evenings of long weekends, to talk though the intriguing mysteries that my observations uncovered throughout my thesis. Ray Jayawardhana deserves my thanks for allowing and insisting that I do the work myself, and reinforcing the notion that it is not shameful to chase "sexy" science. I'm grateful to both my advisors for having enough faith in me to allow me to choose my own projects and effectively blaze my own trail. As a result, this thesis has been an exercise in appreciating the plaque that adorned Harry Truman's desk: "The buck stops here." This brings me to another printable

Contents

List of Tables

List of Figures

Chapter 1

Introduction

1.1 The first Alien Worlds

It is worth stressing the remarkable sea change in the attitude of astronomers on the legitimacy of research to search for, find and characterize planets in solar systems other than our own. While in recent years astrobiology and the theoretical characterization of biomarkers that one might be able to find in the atmospheres of habitable exo-Earths and super-Earths have attracted more and more attention from researchers (e.g. Seager et al. 2005a; Cowan et al. 2009; Palle et al. 2011), it wasn't more than a few decades ago that the mere idea of searching for extrasolar planets was treated with indifference and skepticism, or even derision (Walker, 2008). All of this changed with the announcement of the first extrasolar planet around a sun-like star (Mayor & Queloz, 1995). Within months, the trickle of exoplanet discoveries had begun (Marcy & Butler, 1996; Butler & Marcy, 1996), giving way to the flood that we've enjoyed over the last 15 years.

These detections did not arise out of the ether, but were the result of a long series of instrumental work, technological improvements, near-misses and retracted or disproven claims. The first definitive exoplanet discoveries had already been made, in an unlikely locale orbiting a pulsar (Wolszczan & Frail, 1992); in this oft-neglected work, Wolszczan & Frail (1992) discovered what would turn out to be three planets (Wolszczan, 1994) in this extreme environment, by detecting the subtle variations in the timing of the pulsar. Also, Latham et al. (1989) had already announced an object around a main-sequence star detected via the radial velocity method with a minimum mass of only $\sim$11 Jupiter masses, well below the deuterium burning limit. As these authors explain, a brown dwarf is a more likely explanation for this object, if one assumes an isotropic distribution of inclination angles, making this object one of the first inhabitants of the "brown dwarf" desert (Marcy & Butler, 2000).

Perhaps the most interesting claim[1], was that of a planet orbiting the star γ Cephei with a 2.5 year period from RV measurements using the Canada-France-Hawaii Telescope, as well as a several Jupiter mass companions in a few other systems that showed excess RV trends (Campbell, Walker & Yang, 1988). Interestingly, upon collecting further data that clearly showed an obvious periodic RV signal, Walker et al. (1992) deduced that, although the planetary companion explanation was still viable, rotational modulation was a more likely explanation. Similarly, Walker et al. (1995) downplayed the likelihood that the signals of Campbell, Walker & Yang (1988) were planetary in nature. As it turns out, three of the Campbell, Walker & Yang (1988) signals have since been confirmed, or arguably confirmed in the case of ϵ Eridani, to result from planetary orbital motion: γ Cephei (Hatzes et al., 2003), β Gemini (Hatzes et al., 2006) and ϵ Eridani (Hatzes et al., 2000; Benedict et al., 2006). It is intriguing to read, with the benefit of hindsight, Walker (2008) explain how for the γ Cephei system, the misclassification of the primary, and the underestimate of the period of the outer companion in the system, led the authors to downplay their announcement of what has since become the first confirmed, published exoplanet. The irony is especially rich considering that these authors developed the absorption cell technique with the dangerous and toxic chemical hydrogen fluoride (Campbell & Walker, 1979), that would lead to so much success once the transition was made to the more amenable iodine (Marcy & Butler, 1992).

1.1.1 Fulfilling the promise of Otto Struve

The promise that one might be able to detect the loss of light from the transit of an extrasolar planet across a star (Struve, 1952), was finally realized with the detection of the transit of HD 209458b (Charbonneau et al., 2000; Henry et al., 2000). This seminal discovery would lead to a drastic increase in our knowledge of the properties of exoplanets, by revealing more than the minimum mass, period and eccentricity revealed by radial velocity (RV) surveys. Transit observations, when combined with RV measurements, revealed the true mass of these bodies, their sizes and thus their densities; also, as we explain below, spectroscopic measurements during transit have allowed us to detect chemicals in these planets' atmospheres imprinted on the spectral signal (§1.2). Also, observations when the planet passes behind, or eclipses, its host star have allowed us to measure these planets' thermal emission and its temporal variability as revealed from phase curve observations (§1.3). With approximately 100 transiting planets with confirmed radial velocity measurements, and sensitivities that allow us to detect transiting super-Earths (Leger et al., 2009; Queloz et al., 2009), and the rich bounty of even smaller worlds that Kepler will announce over the coming few years (Borucki et al., 2011), the future

---

[1]The controversy surrounding the disproven claim of an exoplanet around Barnard's star (van de Kamp, 1969; Hershey, 1973; van de Kamp, 1982) is arguably as interesting.

is certainly bright for the study of exoplanets via their transits and eclipses.

1.2 Transmission Spectroscopy

During transit, absorption from the atmospheric limb of the transiting planet imprints itself on the combined stellar and planetary spectrum. Within these absorption lines, the planet will actually appear larger along the line of sight, leading to a deeper transit. A useful approximation for this change in the transit depth is provided by Brown et al. (2001). The change in the planetary radius between the line, R_{PL}, and the continuum, R_{PC}, can be related to the scale height, H, and the opacities in the absorption line, κ_l, and the continuum, κ_c; we can approximate this change as the ratio of these aforementioned opacities multiplied by the area of an annulus one scale height thick relative to that of the stellar disk:

$$(R_{PL}/R_*)^2 - (R_{PC}/R_*)^2 = \frac{2\pi R_P H}{\pi R_*^2} \ln(\kappa_l/\kappa_c). \tag{1.1}$$

Thus, absorption from a small sliver of the limb of the atmosphere of the planet causes this increased absorption in the spectral line.

Transmission spectroscopy is one of those rare subject areas in the field of extrasolar planets where the theory clearly led the observations. Seager & Sasselov et al. (2000) predicted that the alkali metal lines, specifically Na I and K I, would be prominent opacity sources in the atmospheres of hot Jupiters. This did indeed turn out to be the case, to an extent; Charbonneau et al. (2002) used the Hubble Space Telescope's (HST's) STIS spectrograph and detected a deeper transit at 589.3 nm of the hot Jupiter HD 209458b, arising from absorption from the sodium resonance doublet. Surprisingly though, the amplitude of sodium absorption was actually less than expected from a cloud-free atmosphere (Charbonneau et al., 2002). Other detections of sodium absorption followed from the ground using high resolution spectroscopy for the brightest exoplanet host stars (Redfield et al., 2008; Snellen et al., 2008). One explanation for the reduced sodium spectral signal, is the possibility that high altitude hazes from the atmosphere of the planet may mute the spectral features one expects to see; the opacity of these hazes need not be large, as the slant optical depth during transit will be a factor of 35-90 higher than the normal optical depth (Fortney et al., 2005). The importance of hazes has been confirmed for at least one hot Jupiter to date; the optical and UV transmission spectrum of HD 189733b has been confirmed to rise monotonically with a slope consistent with Rayleigh scattering, and to be otherwise featureless in broadband spectrophotometry, from 0.29 - 1.05 μm (Pont et al., 2008; Sing et al., 2011). In the meantime there have been a series of claims of low-resolution detections of spectral features in the near- and mid-infrared that warrant observational confirmation (e.g. Tinetti et al. 2007; Beaulieu et al. 2008; Desert et al. 2008; Swain, Vasisht & Tinetti. 2008; Tinetti et al. 2010).

The next step for transmission spectroscopy, is to extend these searches to the super-Earth and then the exo-Earth regime. In Chapter 5, we discuss such an attempt to detect broadband absorption features from the transmission spectrum of the super-Earths GJ 1214b.

1.3 Thermal Emission from hot Jupiters

The field of thermal emission from hot Jupiters was pioneered with two nearly simultaneous secondary eclipse detections from the exoplanets TrES-1b (Charbonneau et al., 2005) and HD 209458 (Deming et al., 2005). Both measurements used the Spitzer Space Telescope; the former used the IRAC instrument (Fazio et al., 2004) and detected TrES-1b's secondary eclipse in its 4.5 and 8.0 μm channels, while the latter used the MIPS instrument (Rieke et al., 2004) and detected HD 209458b's thermal emission in its 24 μm channel. Shortly after these seminal observations, a series of multiwavelength detections of the thermal emission of hot Jupiters, courtesy of Spitzer and the 3.6, 4.5, 5.8 and 8.0 μm channels of its IRAC camera, came fast and furious (e.g. Knutson et al. 2008; Charbonneau et al. 2008; Machalek et al. 2008; Knutson et al. 2009b). These multiwavelength thermal emission detections have forced our understanding of the atmospheric dynamics and reradiation of these exotic planets to dramatically evolve, as we outline below.

1.3.1 Two classes of hot Jupiters?

The prediction that there could be two classes of hot Jupiters actually predated any of these measurements of the thermal emission of hot Jupiters. In 2003 Hubeny et al. (2003) published the unfortunately titled: "A Possible Bifurcation in Atmospheres of Strongly Irradiated Stars and Planets"; in this work, the authors explained, in language that was unfortunately too opaque to receive the wider interest it deserved, that if there was an absorber at high altitudes a bifurcation could occur that would lead to temperature inversions in the atmospheres of these objects. Hubeny et al. (2003) (and Fortney et al. 2006; Burrows et al. 2007) thus laid the ground-work for Fortney et al. (2008), a more observationally friendly paper, predicting two classes of hot Jupiters that would arise depending on whether their incident stellar flux fell above or below a set value. The sharp incident flux dividing line between these two classes was predicted to arise from whether TiO and VO would remain in gaseous form in their upper layers. TiO and VO are a major optical absorbers in M-dwarfs; this spectral type, consisting of low-mass stars and brown dwarfs, displays prominent TiO and VO absorption bands, while in the cooler L spectral type the influence of TiO and VO wanes (Kirkpatrick et al., 1999; Lodders, 2002). Fortney et al. (2008) predicted that hot Jupiters would display similar characteristics and a similar dichotomy. The dichotomy between these two atmospheric classes was predicted

to arise from the fact that in hotter atmospheres TiO/VO would be able to remain in gaseous form in the upper atmospheric layers, and these chemicals would absorb strongly in the optical at high altitudes, thus forming a hot stratosphere. In cooler atmospheres, TiO and VO were predicted to condense and would rain out from the stratospheres of these worlds. Thus, those hot Jupiters exposed to a large incident stellar flux, were predicted to be analogous to M-type dwarfs, would absorb this incoming starlight high in their atmospheres due to gaseous TiO/VO, would have temperature inversions, strong day/night temperature asymmetries, and feature molecular bands in emission rather than absorption. Those exposed to less stellar flux, analogous to L-type dwarfs, were predicted to absorb the incoming starlight deeper in their atmospheres due to the fact that TiO/VO had rained out, would redistribute the heat more efficiently to their nightsides, and would feature molecular absorption lines.

At the time Fortney et al. (2008) proposed these two classes of hot Jupiters, the theory was extremely successful. Not only were the theoretical predictions easy to understand and easily testable for observers, but the two proposed classes also explained the two hot Jupiters that had been observed (or would shortly be observed) in the four Spitzer/IRAC channels at the time; one planet, HD 209458b, exposed to relatively high incident stellar flux seemed to have a temperature inversion, while the other, HD 189733b, exposed to lower incident flux, conveniently did not have a temperature inversion. Knutson et al. (2008) had already observed HD 209458b in the four Spitzer/IRAC channels and found that the 4.5 and 5.8 μm channels featured much higher emission than one would expect from a blackbody model compared to the 3.6 and 8.0 μm channels. In an accompanying paper, Burrows et al. (2007) had already explained that observing that the 4.5 and 5.8 micron channels were brighter than the other IRAC channels was likely a sign of molecular features in emission rather than absorption; specifically, if this planet had a high altitude optical absorber, such as TiO/VO, the expected water absorption features that would arise from an atmosphere in which the temperature decreased monotonically with altitude, would be switched to water emission features arising from the hot stratosphere. Interestingly, HD 209458b was exposed to just enough incident flux that TiO/VO were predicted to be able to remain in gaseous form in their stratospheres. HD 189733b, on the other hand, was expected to fall below this sharp dividing line. Indeed, HD 189733b was found by Charbonneau et al. (2008) to have 4.5 and 5.8 μm emission relatively lower than the adjacent IRAC bands, a supposed signal of water absorption from a canonical atmosphere without a temperature inversion.

With one post-diction (HD 209458) of a temperature inversion and one prediction (HD 189733) of the lack thereof, this "Two classes of hot Jupiters" Fortney et al. (2008) theory seemed poised to presciently predict that a strict dichotomy would exist and virtually all hot Jupiters would fall into these two classes. Unfortunately, the flush of success of this theory

was short-lived; XO-1b, which is exposed to similar levels of incident flux as HD 189733b, unexpectedly appeared to display signs of a temperature inversion (Machalek et al., 2008), while TrES-3b, which is hot enough that TiO/VO could be present in its upper atmosphere, lacked such an inversion (Fressin et al., 2010). As is so often the case with exoplanets, a simple explanation for their observed characteristics proved elusive.

In addition to the fact that observations of the thermal emission of hot Jupiters were not fully supportive of this "Two classes of hot Jupiters" theory, the prediction that TiO/VO would prove a likely stratospheric absorber begun to be subject to criticism on theoretical grounds. Spiegel et al. (2009) pointed out that for the TiO/VO hypothesis to be viable, the upper atmospheres of these planets would require considerable macroscopic mixing. As TiO and VO are considerably heavier than the primary constituent, molecular hydrogen, of the atmospheres of hot Jupiters, they would therefore be expected to gravitationally settle to lower altitudes. Macroscopic mixing would be required to keep these heavy species aloft. An additional problem to overcome in this hypothesis is that the region directly below the hot stratosphere is by definition cooler than the one above; this cooler region could be a so-called "cold trap" that could cause these species to rain-out before they were even lofted above this cooler layer and could reach the stratosphere. Additionally, Youdin & Mitchell (2010) pointed that even if the level of macroscopic mixing suggested by Spiegel et al. (2009) as necessary to keep these chemicals aloft was even possible, it would likely over-inflate hot Jupiters beyond what we observe by burying heat deep in their convective interior. Lastly, Madhusudhan & Seager (2010) showed that for a number of hot Jupiters the conclusion that these planets do or do not have temperatures inversion may not be so clear; by comparing all the observations up to that date to 10^6 atmospheric models with varying chemical compositions, the authors find that for a few hot Jupiters with claimed temperature inversions, the data can be equally well fit by models with and without such inversions.

An alternative explanation for the observed diversity in the characteristics of hot Jupiters, and specifically their thermal emission, was presented by Knutson et al. (2010). They suggested a correlation between the presence, or lack thereof, of a temperature inversion and the activity of the host stars as measured by Ca II H & K lines. Planets without temperature inversions[2] were found to be orbiting chromospherically active stars, while planets with inversions[3] were found to be orbiting quieter hosts. One possible explanation for this correlation, if it is real, is that as Ca II H & K activity should correlate with enhanced incident UV and X-ray flux, it is speculated that this increased UV flux destroys the high altitude optical absorber that

---

[2]Or perhaps more aptly, considering the Madhusudhan & Seager (2010) analysis, planets that have lower Spitzer/IRAC 4.5 μm flux than 3.6 μm flux, and thus supposedly water features in absorption.

[3]Again more aptly, planets that appear to have greater Spitzer/IRAC 4.5 μm flux than 3.6 μm flux, and thus supposedly water features in emission.

is responsible for the temperature inversion in the first place. The chemical nature of the likely putative stratospheric absorber is unclear; sulfur containing chemicals are one possibility (Zahnle et al., 2009a), but the true nature of this absorber, if it exists, will require further study.

1.3.2 Thermal emission of hot Jupiters in the near-infrared

It is clear from the preceding section that multiwavelength constraints on the thermal emission of hot Jupiters in the mid-infrared obtained with the Spitzer Space Telescope, have been an extremely powerful probe of the atmospheric dynamics and reradiation of these planets. One would expect that multiwavelength constraints across the near-infrared would be equally informative, or even more so. The near-infrared is crucial if we would like to understand the atmospheres of hot Jupiters, because for the hottest hot Jupiters - those generally with the largest signal to noise of their thermal emission measurements - their blackbodies peak at shorter wavelengths than the Spitzer wavelengths. Thus the near-infrared is where the majority of the flux emerges from these planets, and detections in this wavelength range will therefore give us the best estimates of their bolometric luminosities, energy budgets and the fraction of the incident stellar flux that is advected via winds to their nightsides (Barman, 2008). The other reason that the near-infrared is important is that the YJHK bands are water opacity windows; as water is expected to be a dominant source of opacity in the atmospheres of hot Jupiters, near-infrared observations should be able to probe much deeper in the atmospheres of hot Jupiters to higher pressure and lower altitude regions (Seager et al., 2005b; Fortney et al., 2008; Burrows et al., 2008b) - atmospheres that may be highly vertically stratified (Menou & Rauscher 2009 and references therein). For this reason, near-infrared detections should prove particularly potent when combined with observations at longer wavelengths, such as those provided by Spitzer, as they should allow us to constrain the temperature-pressure profile of the atmosphere of these planets across a wide wavelength range, from deep in their atmospheres to their high altitude stratospheres.

Although, obviously scientifically interesting, near-infrared detections of the thermal emission of hot Jupiters were not achieved as early as those in the mid-infrared with Spitzer, because the secondary eclipse signal is much more challenging in the near-infrared. The depth of the secondary eclipse, analogous to the planetary to stellar flux ratio, is much smaller in the near-infrared than at mid-infrared wavelengths; this is because, even though hot Jupiters' blackbodies often peak in the near-infrared, the stellar blackbodies peak at shorter wavelengths, and thus the ratio of these two quantities only becomes favourable at longer wavelengths. The challenge of achieving detections in the near-infrared from the ground did not deter numerous researchers from attempting this feat; unfortunately, these attempts, at first, only returned

ever more sensitive upper-limits using photometry (Snellen, 2005; Snellen & Covino, 2007) and spectroscopy (Richardson et al., 2003; Deming et al., 2005b; Knutson et al., 2007a).

The first detection in the near-infrared of the thermal emission of a hot Jupiter occurred from space using the HST; Swain et al. (2009a) used the NICMOS instrument to detect thermal emission and a putative spectrum from 1.5 - 2.5 μm from the planet orbiting HD 189733b. With this data, these authors also claimed to see spectral absorption features that indicated the presence of water, carbon monoxide and dioxide in HD 189733b's atmosphere. However, Gibson et al. (2010) recently published a study that calls many of the claimed NICMOS spectroscopy detections (Swain, Vasisht & Tinetti., 2008; Swain et al., 2009a,b; Tinetti et al., 2010) into question. Gibson et al. (2010) found that by using a slightly different NICMOS instrument model one could return wildly different results than the original model used in the above analyses; as they found no reason to prefer one instrument model over the other they suggested that the claimed detections of molecular species in these atmospheres were not robust. A counter-claim by the original detection team (Deroo, Swain & Vasisht, 2010), as well as a counter to the counter-claim (Gibson et al., 2011) have already been submitted to the arXiv. The truth likely lies somewhere in the middle; although there may well be subtle signs of the molecular features previously claimed in the emission spectrum of HD 189733 (Swain et al., 2009a), and later HD 209458 (Swain et al., 2009b), they were likely not detected with nearly the statistical accuracy claimed in these publications[4]. Nonetheless, it is debatably still safe to grant the honour of the first detection of thermal emission from a hot Jupiter in the near-infrared to Swain et al. (2009a).

Following this now controversial claim of the first near-infrared detection from space, two claimed detections quickly appeared simultaneously from the ground. de Mooij & Snellen (2009) presented a 6σ detection of the Ks-band thermal emission of TrES-3b using the LIRIS instrument on the William Herschel Telescope, while Sing & Lopez-Morales (2009) presented a 4σ detection of the secondary eclipse of OGLE-TR-56b in z'-band using combined photometry from the Magellan and the Very Large Telescope. The latter detection, being in the very near-infrared, probably consists of predominantly thermal emission with a small amount of reflected light from a planet that appears to have a low albedo (Sing & Lopez-Morales, 2009). Despite the troubling systematics induced by our own Earth's atmosphere, after these aforementioned detections demonstrated the feasibility of detecting thermal emission in the near-infrared from the ground, an avalanche of thermal emission detections of hot Jupiters have resulted (e.g. Gillon et al. 2009; Rogers et al. 2009; Lopez-Morales et al. 2010; Anderson et al. 2010; Gibson

---

[4]One should note that recently Shabram et al. (2011) have also called the theoretical transmission spectroscopic atmospheric models used in these claimed detections (Swain, Vasisht & Tinetti. 2008; Swain et al. 2009a,b; Tinetti et al. 2010) into question.

et al. 2010; de Mooij et al. 2011). Joining this cavalcade of results are our own detections of the thermal emission of TrES-2b, TrES-3b, and WASP-3b in Ks-band, and that of WASP-12b in J, H and Ks-band, which we discuss in detail in chapters 2, 3, 6, and 4 respectively.

It is unclear at the present date whether near-infrared thermal emission detections will live up to their potential of being as informative as detections in the Spitzer mid-infrared wavelengths in informing our understanding of the atmospheric properties of hot Jupiters[5]. A potent example of the relative strengths and weaknesses of these infrared detections is demonstrated by Madhusudhan et al. (2010); this work presented a combined analysis of the thermal emission detections of the highly irradiated hot Jupiter WASP-12b from ∼1.2 to nearly 10 μm, using photometry from the Spitzer Space Telescope (Campo et al., 2011), and our own CFHT/WIRCam photometry (discussed in Chapter 4). In this work Madhusudhan et al. (2010) argue that WASP-12b has a carbon/oxygen ratio greater than one; while our own near-infrared CFHT/WIRCam observations were able to probe the deep layers of the atmosphere of this planet and were therefore able to constrain WASP-12b's bolometric luminosity, it was the Spitzer/IRAC wavelengths that were useful probes of the planet's molecular composition. Madhusudhan et al. (2010) argue that the low thermal emission values in the 3.6 and 4.5 μm bands are indicative of methane and carbon-dioxide absorption features, thus leading to a high carbon-oxygen ratio. We caution that spectral energy distributions probed via broadband spectroscopy can be difficult to interpret due to the conflicting behaviour of vertically stratified atmospheres and absorption and emission features. We note that according to the Madhusudhan et al. (2010) analysis a solar C/O ratio is only excluded at just greater than the 4σ level; as the lesson from exoplanets is seemingly that they are always more complicated than our simple models suggest, further observations and analysis to confirm this speculative claim that WASP-12b has such a high C/O ratio are encouraged.

1.3.3   Future prospects of near-infrared thermal emission detections from the ground

Broadband photometric detections of thermal emission have greatly contributed to our understanding of the atmospheric properties of hot Jupiters and can be expected to continue to do so. One area of future promise is near-infrared thermal phase curve observations from the ground. This field was pioneered from space in the mid-infrared by Knutson et al. (2007b), who used the Sptizer/IRAC instrument at 8.0 μm and observed the bright exoplanet host star HD 189733 for half of its orbit, from before transit until after its secondary eclipse. These authors observed the near-sinusoidal increase in thermal flux as the cooler nightside rotated out of view, and

---

[5]We summarize the lessons from the current near-infrared detections in chapter 6.

then the hotter dayside rotated into view. In this way, these authors were able to constrain the day/night temperature asymmetry, and therefore determine the efficiency of advection to transport the incident stellar flux from the dayside to the nightside of the planet. Since this seminal measurement, a series of thermal phase curves have been measured with Spitzer for tidally locked hot Jupiters (e.g. Knutson et al. 2009a,c; Crossfield et al. 2010), as well as for eccentric exoplanets (Laughlin et al., 2009). Although these phase curve detections have been undeniably informative, they are all at wavelengths longer than or equal to 8.0 μm[6]. Thus these observations probe the day/night redistribution of heat at a set pressure range, high in the stratosphere of these planets. What would be interesting is to obtain a series of thermal phase curve measurements at a variety of wavelengths and thus pressures; as the near-infrared should peer to high pressure regions through windows in the water opacity, phase curve measurements in the JHK bands will determine the efficiency of day/night heat redistribution deep in these planets' atmospheres. Near-infrared phase curves, when combined with phase curve observations in the Spitzer wavelengths, will allow us to precisely determine the energy budgets of these planets, and how efficiently advection redistributes heat to the nightsides as one descends from their stratospheres into their deep atmospheric layers. Unfortunately, as we document in various chapters in this thesis (Chapters 2-6), near-infrared broadband photometry is affected by variability on several hour timescales, that have thus far frustrated any attempts to perform such phase curves from the ground. We discuss ideas on how to overcome these systematic errors in Chapter 7.

As informative as broadband spectroscopy is, low and high-resolution spectroscopy will ultimately prove more informative and a better use of telescope resources if one is able to calibrate the systematic errors that often frustrate work in the near-infrared. Recently, Swain et al. (2010) used the SpeX instrument on the NASA Infrared Telescope Facility and performed low spectral resolution ($\lambda/\Delta\lambda\sim30$) observations of the planet orbiting the bright host HD 189733. Those authors claimed a detection of thermal emission from the planet across 9 spectrophotometric bins from 2 - 4 μm; the most speculative claim from this work was that of a ~3.25 μm emission feature that required non-local thermodynamic equilibrium (LTE) conditions to explain its prominence. Unfortunately, the Swain et al. (2010) spectrophotometry suffered from significant systematics that were the most acute near ~3.3 μm. More recently, Mandell et al. (2011) used NIRSPEC on Keck II to perform high resolution ($\lambda/\Delta\lambda\sim27,000$) spectroscopic observations of this target around ~3.3 μm, at a wavelength that overlaps with the claimed Swain et al. (2010) non-LTE feature. These new observations do not reproduce the claimed non-LTE feature; moreover, if this non-LTE features falls within the NIRSPEC bandpass, then these

---

[6]Several Spitzer/IRAC 3.6 and 4.5 μm channel hot Jupiter thermal phase curves should be published in the near-term future from warm Spitzer observations.

observations are able to rule out the feature with very strong confidence (40σ). Also, Mandell et al. (2011) show that the proposed astrophysical mechanisms to explain this non-LTE feature, such as fluorescence, are unable to reproduce its observed prominence. The authors conclude that telluric water contamination is the most likely explanation for the observed feature. For the sake of the present discussion, it appears it is still an unanswered question, how, or if, one can overcome the systematics of the near-infrared sky to perform low spectral resolution spectroscopy across a wide wavelength range of the thermal emission of hot Jupiters from the ground.

Pioneering high resolution spectroscopy in the near-infrared from the ground has recently been performed by Snellen et al. (2010) using the CRIRES instrument on UT1 of the Very Large Telescope. They obtained a spectrum of HD 209458 from 2.29-2.35 μm with very high spectral resolution of $\lambda/\Delta\lambda\sim$100,000. The authors detected carbon monoxide absorption arising from the atmosphere of the planet with greater than 5σ confidence. Interestingly, the carbon monoxide signal is blueshifted by 2 kms^{-1} (2σ result); this has been interpreted as possibly arising from a high altitude wind flowing from the dayside to the nightside of the planet. Although, it is unclear if the claimed 2σ blueshift is physical, or if its interpretation as a sign of the planetary wind is valid, the carbon monoxide detection itself appears robust. Snellen et al. (2010) only calibrate their data by cross-correlating it with a predicted model atmosphere of the planet with numerous CO absorption lines. Clearly, this technique is worthy of further study and application to more exoplanet hosts. However, as their self-calibration method requires very high resolution spectroscopy, the application of their techniques to other telescopes may be limited, as the Deming et al. (2005b) NIRSPEC observations of HD 209458b show even NIRSPEC may not provide sufficient spectral resolution.

One possible route forward to achieve medium resolution coverage in the near-infrared is the MOSFIRE multi-object spectrograph (McLean et al., 2008). MOSFIRE should be commissioned on Keck in 2011. MOSFIRE has a resolving power of $\sim$3,270 with a spectral coverage from the Y-band to K-band. The 6×6 arcminute field of view should allow us to correct the flux of the target star with numerous reference stars, similar to our CFHT/WIRCam work. Thus it may be possible to achieve similar accuracy to our work with CFHT/WIRCam, except with medium resolution spectroscopy across broad swaths of the near-infrared.

Precise near-infrared spectrophotometry will undoubtedly be revolutionized by the launching of the James Webb Space Telescope (JWST; Mather et al. 2010). The NIRSpec instrument (Birkmann et al., 2010) on JWST will be a multi-object spectrograph with a 9.1 square arcmin field of view from 0.6 - 5.0 μm, and spectral resolutions from 100 to 3000. However, the launching of JWST will not negate the importance of being able to achieve near photon limited precision in the near-infrared from the ground; presuming that one or two Extremely

Large Telescope projects goes forward, there will likely be an instrument optimized for the near-infrared on one of these telescopes. It will therefore be crucial to be aware of methods to overcome the limiting systematics that have left current near-infrared photometry well below the photon noise limit. We discuss possible methods for improving our near-infrared photometric precision, that may be applicable to some of these future ground-based projects, in Chapter 7.

Chapter 2

Near-infrared Thermal Emission from the Hot Jupiter TrES-2b

2.1 Abstract

We present near-infrared Ks-band photometry bracketing the secondary eclipse of the hot Jupiter TrES-2b using the Wide-field Infrared Camera on the Canada-France-Hawaii Telescope. We detect its thermal emission with an eclipse depth of $0.062^{+0.013}_{-0.011}\%$ (5σ). Our best-fit secondary eclipse is consistent with a circular orbit (a 3σ upper limit on the eccentricity, e, and argument or periastron, ω, of $|e\cos\omega| < 0.0090$), in agreement with mid-infrared detections of the secondary eclipse of this planet. A secondary eclipse of this depth corresponds to a day-side Ks-band brightness temperature of $T_B = 1636^{+79}_{-88}$ K. Our thermal emission measurement when combined with the thermal emission measurements using Spitzer/IRAC from O'Donovan and collaborators suggest that this planet exhibits relatively efficient day to night-side redistribution of heat and a near isothermal dayside atmospheric temperature structure, with a spectrum that is well approximated by a blackbody. It is unclear if the atmosphere of TrES-2b requires a temperature inversion; if it does it is likely due to chemical species other than TiO/VO as the atmosphere of TrES-2b is too cool to allow TiO/VO to remain in gaseous form. Our secondary eclipse has the smallest depth of any detected from the ground at around 2 μm to date.

2.2   Introduction

The first detection of the transit of an exoplanet in front of its parent star (Charbonneau et al. 2000; Henry et al. 2000) opened a new avenue to determine the characteristics of these exotic worlds. For all but the most eccentric cases, approximately half-an-orbit after their transits these planets pass behind their star along our line of sight allowing their thermal flux to be measured in the infrared. The first detections of an exoplanet's thermal emission (Charbonneau et al. 2005; Deming et al. 2005) came from observations in space with Spitzer using the Infrared Array Camera (IRAC; Fazio et al. 2004). Since then the vast majority of such measurements have been made using Spitzer at wavelengths longer than 3 μm, and thus longwards of the blackbody peak of these "hot" exoplanets. Recent observations have extended secondary eclipse detections into the near-infrared; the first detection was from space with NICMOS on the Hubble Space Telescope (Swain et al. 2009a at ~ 2 μm). More recently, near-infrared detections have been achieved from the ground; the first of these detections include a $\sim 6\sigma$ detection in K-band of TrES-3b using the William Herschel Telescope (de Mooij & Snellen, 2009), a $\sim 4\sigma$ detection in z'-band of OGLE-TR-56b using Magellan and the Very Large Telescope (VLT; Sing & Lopez-Morales 2009), and a $\sim 5\sigma$ detection at ~ 2.1 μm of CoRoT-1b also with the VLT (Gillon et al., 2009).

Thermal emission measurements in the near-infrared are crucial to our understanding of these planets' atmospheres, as they allow us to constrain hot Jupiters' thermal emission near their blackbody peaks. The combination of Spitzer/IRAC and near-infrared thermal emission measurements allows us to constrain the temperature-pressure profiles of these planets' atmospheres over a range of pressures (Fortney et al., 2008), to better estimate the bolometric luminosity of these planets' dayside emission, and thus contributes to a more complete understanding of how these planets transport heat from the day to nightside at a variety of depths and pressures in their atmospheres (Barman, 2008).

The transiting hot Jupiter TrES-2b orbits a G0 V star with a period of ~ 2.47 d (O'Donovan et al., 2006). According to the Fortney et al. (2008) theory this places TrES-2b marginally in the hottest, mostly highly irradiated class (the pM-class) of hot Jupiters and close to the dividing line between this hottest class and the merely warm class of hot Jupiters (the pL-class). Thus, TrES-2b could be a key object to refine the dividing line between these two classes, and could indicate the physical cause of this demarcation, or reveal whether this divide even exists. Recently O'Donovan et al. (2010) used Spitzer/IRAC to measure the depth of the secondary eclipse of TrES-2b in the four IRAC bands. Their best-fit eclipses are consistent with a circular orbit, and collectively they are able to place a 3σ limit on the eccentricity, e, and argument of periastron, ω, of $|e\cos\omega| < 0.0036$. Their best-fit eclipses at 3.6, 5.8 and 8.0 μm are well-fit by

a blackbody. At 4.5 μm they detect excess emission, in agreement with the theory of several researchers (Fortney et al. 2008; Burrows et al. 2008a) that predicts such excess due to water emission, rather than absorption, at this wavelength due to a temperature inversion in the atmosphere. One-dimensional radiative-equilibrium models for hot Jupiter planets generally show that the atmospheric opacity is dominated by water vapor, which is especially high in the mid-infrared, but has prominent windows (the JHK bands) in the near infrared (Fortney et al., 2008; Burrows et al., 2008a). One can probe more deeply, to gas at higher pressure, in these opacity windows. Models without temperature inversions feature strong emission in the JHK bands, since one sees down to the hotter gas. Models with temperature inversions, since they feature a relatively hotter upper atmosphere and relatively cooler lower atmosphere, yield weaker emission in the near-IR (JHK), but stronger emission in the mid-infrared (Hubeny et al., 2003; Fortney et al., 2006). Near-infrared thermal emission measurements should thus be useful to determine whether TrES-2b does or does not harbour a temperature inversion.

Owing to its high irradiation, with an incident flux of $\sim 1.1 \times 10^9 \ erg s^{-1} cm^{-2}$, and favourable planet-to-star radius ratio ($R_P/R_* \sim 0.13$), we included TrES-2b in our program observing the secondary eclipses of some of the hottest of the hot Jupiters from the ground. Here we present Ks-band observations bracketing TrES-2b's secondary eclipse using the Wide-field InfraRed Camera (WIRCam) on the Canada-France-Hawaii Telescope (CFHT). We report a 5σ detection of its thermal emission.

2.3   Observations and data reduction

We observed TrES-2 (K=9.846) with WIRCam (Puget et al., 2004) on CFHT on 2009 June 10 under photometric conditions. The observations lasted for $\sim$3.5 hours evenly bracketing the predicted secondary eclipse of this hot Jupiter assuming it has a circular orbit. Numerous reference stars were also observed in the 21x21 arcmin field of view of WIRCam. To minimize the impact of flat field errors, intrapixel variations and to keep the flux of the target star well below detector saturation, we defocused the telescope to 1.5mm, such that the flux of our target was spread over a ring $\sim$20 pixels in diameter (6") on our array.

We observed TrES-2 in "stare" mode on CFHT where the target star is observed continuously without dithering. 5-second exposures were used to avoid saturation. To increase the observing efficiency we acquired a series of data-cubes each containing twelve 5-second exposures. The twelve exposure data-cube is the maximum number of exposures allowed in a guide-cube in queue mode at CFHT. To counteract drifts in the position of the stars positions on the WIRCam chips, which we had noticed in earlier WIRCam observations of secondary eclipses (Croll et al., 2010b), we initiated a corrective guiding "bump" before every image cube
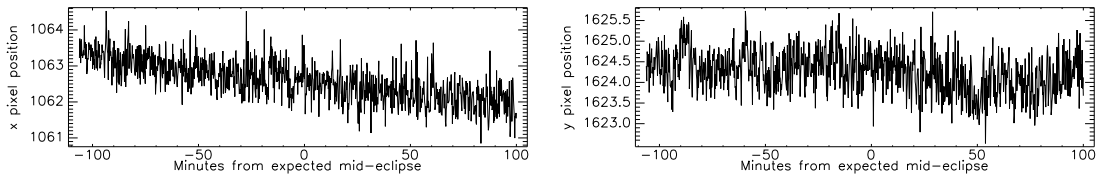
Figure 2.1 The x and y position of the centroid of the PSF of the target star, TrES-2, with time (top panels).

to recenter the stellar point-spread-function as near as possible to the original pixels at the start of the observation. The effective duty cycle after accounting for readout and for saving exposures was 43%. The images were preprocessed with the 'I'iwi pipeline[1]. This pipeline includes the following steps: applying a non-linearity flux correction, removing bad and saturated pixels, dark subtraction, flat-fielding, sky subtraction, zero-point calibration and a rough astrometry determination. We sky subtract our data by constructing a normalized sky frame built by taking the median of a stack of source-masked and background-normalized on-sky images. Our on-sky images consist of 15 dithered in-focus images observed before and after the on-target sequence. For each on-target image the normalized sky frame is scaled to the target median background level and then subtracted.

We performed aperture photometry on our target star and all unsaturated, reasonably bright reference stars on the WIRCam array. We used a circular aperture with a radius of 12.5 pixels. We tested larger and smaller apertures in increments of 0.5 pixels, and confirmed that this size of aperture returned optimal photometry. The residual background was estimated using an annulus with an inner radius of 21 pixels, and an outer radius of 30 pixels; a few different sizes of sky annuli were tested, and it was found that the accuracy of the resulting photometry was not particularly sensitive to the size of the sky aperture. As TrES-2 has a nearby reference star (0.17 arcmin separation) that falls in our sky aperture, we exclude a slice of the annulus that falls near this reference star to avoid any bias in background determination[2]. During our observations, despite the aforementioned corrective "bump" to keep the centroid of our stellar point-spread-function (PSF) as steady as possible, our target star and the rest of the stars on our array displayed high frequency shifts in position (Figure 2.1). To ensure that the apertures for our photometry were centered in the middle of the stellar PSFs, we used a center-of-mass calculation, with pixel flux substituted for mass, to determine the x and y centers of our defocused stellar rings for each one of our target and reference star apertures.

The light curves for our target and reference stars following our aperture photometry dis-

---

[1] http://www.cfht.hawaii.edu/Instruments/Imaging/WIRCam/IiwiVersion1Doc.html
[2] Pixels that fall from 5° to -45° degrees as measured from due North towards the East are excluded from our annulus.
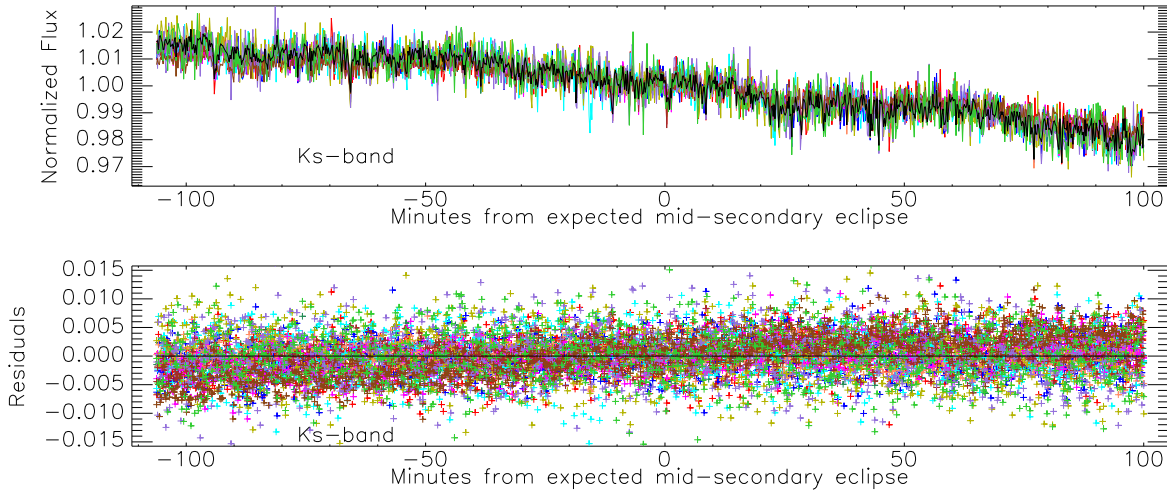
Figure 2.2 Top panel: The normalized flux from the target star (black) and the reference stars that are used to calibrate the flux of TrES-2b (various colours). Bottom panel: The residuals from the normalized flux of the target star of the normalized flux of the reference stars (various colours). The residuals have not been corrected for the x/y pixel positions of the target.

played significant, systematic variations in intensity (see the top panel of Figure 2.2), possibly due to changes in atmospheric transmission, seeing and airmass, guiding errors and/or other effects. The target light curve was then corrected for these systematic variations by normalizing its flux to the 11 reference stars that show the smallest deviation from the target star outside of the expected occultation. Reference stars that showed significant deviations in-eclipse from that of the target star and other reference stars, as indicated by a much larger root-mean-square in-eclipse than out-of-eclipse due to intermittent systematic effects for instance, were also excluded. For the reference stars that were chosen for the comparison to our target star, the flux of each one of these star was divided by its median-value, and then an average reference star light curve was produced by taking the mean of the light curves of these median-corrected reference stars. The target flux was then normalized by this mean reference star light curve.

Figure 2.3 marks the 11 reference stars used to correct the flux of our target; the 2MASS identifiers of the reference stars are given in Table 2.1. Note that the majority of the reference stars with the smallest out of occultation residuals to our target star are on the same chip as our target, despite the fact that there are other reference stars on other chips closer in magnitude to our target. We believe that this is due to the differential electronic response of the different WIRCam chips, and have noticed this same effect with other WIRCam observations of other hot Jupiter secondary eclipses (Croll et al., 2010b).

Following this correction we noticed that the flux of our target and reference stars displayed

Table 2.1.   TrES-2 Reference Stars

Reference Star #	2MASS Identifier	K-band Magnitude
1	J19072977+4918354	10.294
2	J19065501+4916195	10.737
3	J19071365+4912041	11.270
4	J19065809+4916315	9.875
5	J19070093+4917323	11.337
6	J19074435+4915418	10.766
7	J19071824+4916526	11.239
8	J19073380+4916035	10.712
9	J19071955+4911176	11.514
10	J19075629+4923281	9.671
11	J19065548+4925404	11.454
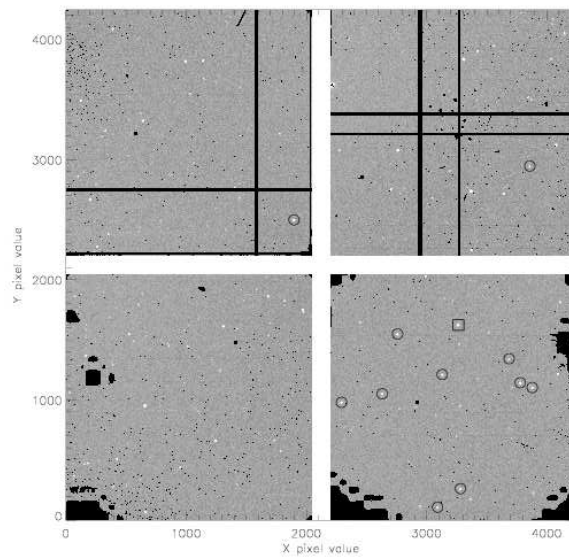
Figure 2.3 The CFHT/WIRCam full frame array during our observations of TrES-2b. The image has been preprocessed with the 'I'iwi pipeline; the obvious artifacts (in the lower-left corners of the bottom two chips for instance or the crosses on the upper two chips) are due to the masking of bad pixels. The target star, TrES-2 (large square on the lower-right chip), and the reference stars used to correct the flux of TrES-2 (circles) are marked.
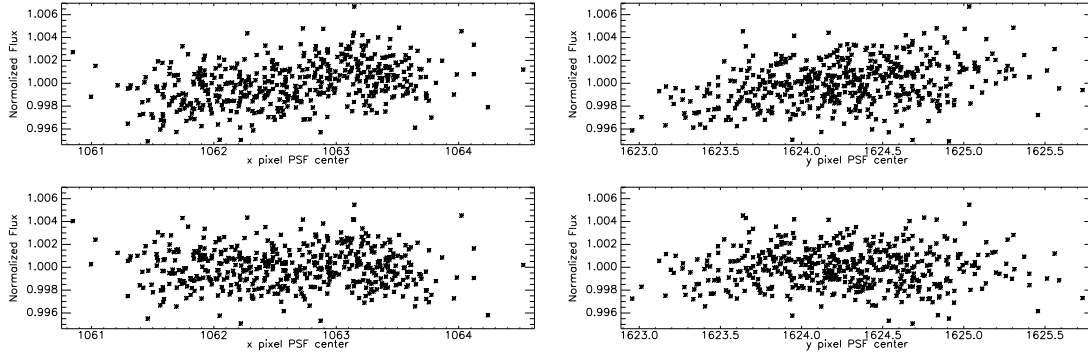
Figure 2.4 The out-of-eclipse photometry prior to the correction for the x and y position of the PSF (top panels). The out-of-eclipse photometry following this correction (bottom panels; see §6.3 for details).
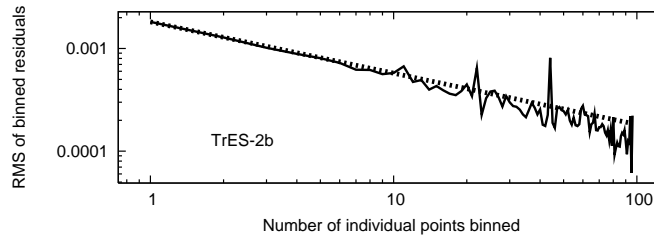
Figure 2.5 The root-mean-square of our out-of-eclipse photometry (solid line) following the various corrections documented in §6.3. The dashed line displays the one over the square-root of the bin-size expectation for Gaussian noise.

near-linear correlations with the x or y positions of the centroid of the stellar PSF on the chip. Given the aforementioned high frequency of these shifts (Fig. 2.1) this suggests that any leftover trend with position and the flux of the star was instrumental in origin. Thus these near-linear trends (Figure 2.4 top panels) were removed from the data for both the target and reference stars by performing a fit to the x and y position of the centroid of the PSF and the normalized flux for the out-of-eclipse photometry. We fit the out-of-eclipse photometric flux to the x and y position of the centroid of the PSF with a function of the following form:

$$f = 1 + d_1 x + d_2 y + d_3 xy \tag{2.1}$$

where d_1, d_2, and d_3 are constants. We then apply this correction to both the in-eclipse and out-of-eclipse photometry. The out-of-eclipse photometric data prior to and following this correction are displayed in Figure 2.4 (bottom panels). No other trends that were correlated with instrumental parameters were found.

By correcting the flux of our target with these 11 reference stars and by removing the above correlation with the x/y position on the chip the point-to-point scatter of our data outside

occultation improves from a root-mean-square (RMS) of 13.7×10^{-3} to 0.71×10^{-3} per every 58 s (or 5 images). The photometry following the aforementioned analysis is largely free of systematics, as evidenced by the fact that the out-of-eclipse photometric precision lies near the Gaussian noise expectation for binning the data of one over the square-root of the bin-size (Figure 2.5). Our observations in Ks-band, though, are still well above the predicted photon noise RMS limit of 2.3×10^{-4} per 58 seconds. For the following analysis we set the uncertainty on our individual measurements as 0.95 times the RMS of the out of eclipse photometry after the removal of a linear-trend with time; we found simply using 1.0 times the RMS of the out-of-eclipse photometry resulted in a reduced χ^2 below one, and thus resulted in a slight over-estimation of our errors.

2.4 Analysis

Similarly to nearly all our near-infrared photometric data-sets taken with CFHT/WIRCam (e.g. Croll et al. 2010b, 2011), our Ks-band photometry following the reduction exhibited an obvious background trend, B_f. This background term displayed a near-linear slope, and thus we fit the background with a linear-function of the form:

$$B_f = 1 + c_1 + c_2 dt \tag{2.2}$$

where dt is the time interval from the beginning of the observations, and c_1 and c_2 are the fit parameters. Given that most of our other data-sets display these background trends, it is unlikely, but not impossible, that this slope is intrinsic to TrES-2. We fit for the best-fit secondary eclipse and linear fit simultaneously using Markov Chain Monte Carlo (MCMC) methods (Christensen et al. 2001; Ford 2005; described for our purposes in Croll 2006). We use a 5×10^6 step MCMC chain. We fit for c_1, c_2, the depth of the secondary eclipse, ΔF, and the offset that the eclipse occurs later than the expected eclipse center, t_{offset}[3]. We also quote the best-fit phase, ϕ, as well as the best-fit mid-eclipse heliocentric julian-date, $t_{eclipse}$. We use the Mandel & Agol (2002) algorithm without limb darkening to generate our best-fit secondary eclipse model. We obtain our stellar and planetary parameters for TrES-2 from Torres et al. (2008), including the planetary period and ephemeris. The results from these fits are presented in Table 6.1. The phase dependence of the best-fit secondary eclipse is presented in Figure 2.6. The best-fit secondary eclipse is presented in Figure 2.7.

To determine the effect of any excess systematic noise on our photometry and the resulting fits we employ the "residual-permutation" method as discussed in Winn et al. (2009). In this method the best-fit model is subtracted from the data, the residuals are shifted between 1 and

---

[3]we take into account the 0.6 minute offset due to light travel-time in the system [Loeb 2005]
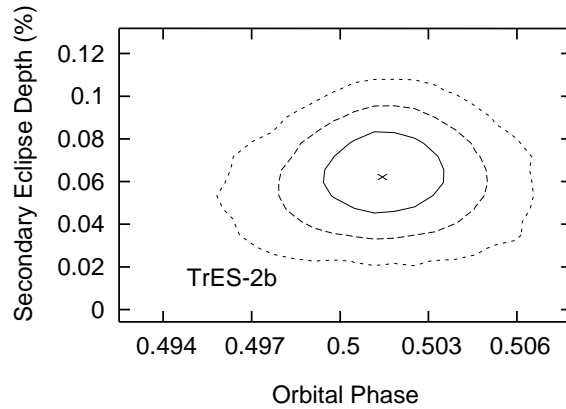
Figure 2.6 The 68.3% (1σ; solid-line), 95.5% (2σ; dashed-line) and 99.7% (3σ; short dashed-line) credible regions from our MCMC analysis on the secondary eclipse depth, ΔF, and phase, ϕ. The "x" in the middle of the plot denotes the best-fit point from our MCMC analysis.
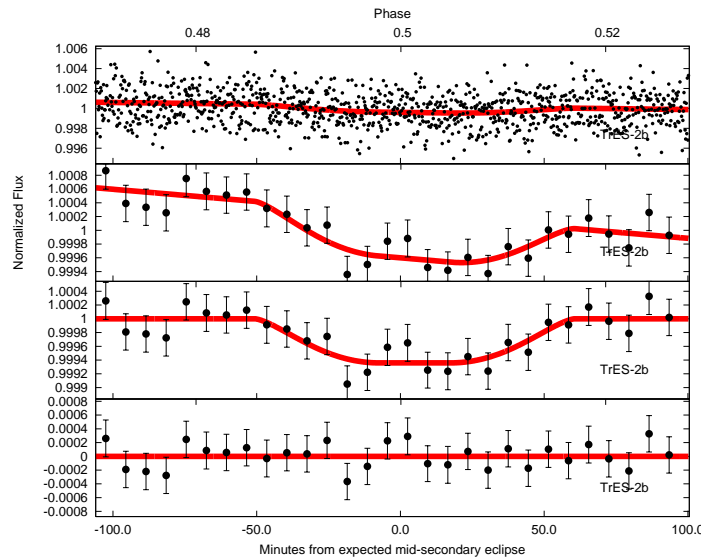
Figure 2.7 CFHT/WIRCam Ks-band photometry of the secondary eclipse of TrES-2b. The top panel shows the unbinned light curve, while the panel that is the second from the top shows the light curve with the data binned every 7.0 minutes. The panel that is the second from the bottom shows the binned data after the subtraction of the best-fit background, B_f, while the bottom panel shows the binned residuals from the best-fit model. In each one of the panels the best-fit best-fit secondary eclipse and background, B_f, is shown with the red line. The expected mid-secondary eclipse is if TrES-2b has zero eccentricity.

Table 2.2.   TrES-2b's best-fit secondary eclipse parameters

Parameter	MCMC Solution	"Residual permutation" Solution
reduced χ^2	$1.089^{+0.003}_{-0.002}$	$1.086^{+0.018}_{-0.001}$
ΔF	$0.062^{+0.013}_{-0.011}\%$	$0.064^{+0.005}_{-0.005}\%$
$t_{offset}\ (min)$[a]	$4.5^{+4.8}_{-4.6}$	$3.8^{+4.6}_{-3.0}$
$t_{eclipse}$ (HJD-2440000)	$14994.0605^{+0.0033}_{-0.0032}$	$14994.0600^{+0.0032}_{-0.0021}$
c_1	$0.00061^{+0.00010}_{-0.00012}$	$0.00061^{+0.00008}_{-0.00007}$
$c_2\ (d^{-1})$	$-0.005^{+0.001}_{-0.001}$	$-0.005^{+0.001}_{-0.002}$
ϕ [a]	$0.5014^{+0.0013}_{-0.0013}$	$0.5012^{+0.0013}_{-0.0008}$
$T_B\ (K)$	1636^{+79}_{-88}	1646^{+29}_{-30}
$e\cos(\omega)$ [a]	$0.0020^{+0.0021}_{-0.0021}$	$0.0017^{+0.0020}_{-0.0020}$
f_{Ks}	$0.358^{+0.074}_{-0.072}$	$0.367^{+0.027}_{-0.026}$

[a]We account for the increased light travel-time in the system (Loeb, 2005).

the total number of data points (N=1056 in our case), and then the best-fit model is added back to the residuals. We then refit the adjusted light curve with a 5000-step MCMC chain and record the parameters of the lowest χ^2 point reached. By inverting the residuals we are able to perform $2N - 1$ total iterations. The best-fit parameters and uncertainties obtained with this method are similar to those found for our MCMC method and are listed in Table 6.1. As the two methods produce similar results we employ the MCMC errors for the rest of this paper. We also test for autocorrelation among the residuals to our best-fit model using the Durbin-Watson test (Durbin & Watson, 1951); for the Durbin-Watson test a test-statistic greater than 1.0 and less than 3.0 (ideally near 2.0) indicates a lack of autocorrelation. Our residuals pass this test with a test-statistic of 1.97.

2.5   Discussion

The depth of our best-fit secondary eclipse is $0.062^{+0.013}_{-0.011}$%. The reduced χ^2 is 1.089. Our best-fit secondary eclipse is consistent with a circular orbit; the offset from the expected eclipse center is: $t_{offset} = 4.5^{+4.8}_{-4.6}$ minutes (or at a phase of ϕ=$0.5014^{+0.0013}_{-0.0013}$). This corresponds to a limit on the eccentricity and argument of periastron of $e \cos \omega = 0.0020^{+0.0021}_{-0.0021}$, or a 3σ limit of $|e\cos\omega| < 0.0090$). Our result is fully consistent with the more sensitive $e\cos\omega$ limits reported from the secondary eclipse detections at the four Spitzer/IRAC wavelengths (O'Donovan et al., 2010). Thus our result bolsters the conclusion of O'Donovan et al. (2010) that tidal damping of the orbital eccentricity is unlikely to be responsible for "puffing up" the radius of this exoplanet.

A secondary eclipse depth of $0.062^{+0.013}_{-0.011}$% corresponds to a brightness temperature of T_B = 1636^{+79}_{-88} K in the Ks-band assuming the planet radiates as a blackbody, and adopting a stellar effective temperature of $T_{eff} = 5850 \pm 50$ (Sozzetti et al., 2007). This compares to the equilibrium temperature of TrES-2b of T_{eq}~1472 K assuming isotropic reradiation, and a zero Bond albedo. Hot Jupiter thermal emission measurements allow joint constraints on the Bond albedo, A_B, and the efficiency of day to nightside redistribution of heat on these presumably tidally locked planets. The Bond albedo, A_B is the fraction of the bolometric, incident stellar irradiation that is reflected by the planet's atmosphere. We parameterize the redistribution of dayside stellar radiation absorbed by the planet's atmosphere to the nightside by the reradiation factor, f, following the Lopez-Morales & Seager (2007) definition. If we assume a Bond albedo near zero, consistent with observations of other hot Jupiters (Charbonneau et al., 1999; Rowe et al., 2008) and with model predictions (Burrows et al., 2008b), we find a reradiation factor of $f_{Ks} = 0.358^{+0.074}_{-0.072}$ from our Ks-band eclipse photometry only, indicative of relatively efficient advection of heat from the day-to-nightside at this wavelength. In comparison, the reradiation factor for an atmosphere that reradiates isotropically is f=$\frac{1}{4}$, while f=$\frac{1}{2}$ denotes redistribution
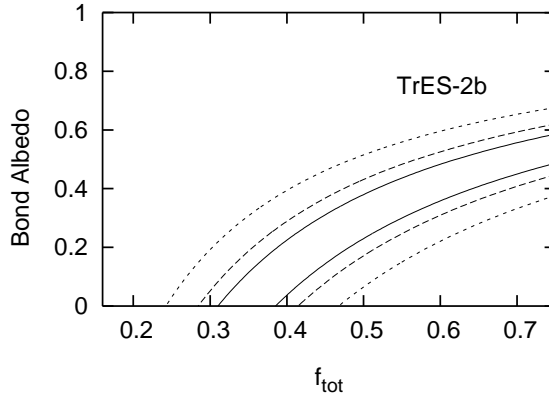
Figure 2.8 The 68.3% (1σ; solid-line), 95.5% (2σ; dashed-line) and 99.7% (3σ; short dashed-line) χ^2 confidence regions on the reradiation factor, f_{tot}, and Bond albedo from the combination of our Ks-band point and the Spitzer/IRAC measurements (O'Donovan et al., 2010).

and reradiation over the dayside face only.

Our secondary eclipse depth, when combined with the secondary eclipse depths at the Spitzer/IRAC wavelengths from O'Donovan et al. (2010), is consistent with a range of Bond albedos, A_B, and efficiencies of the day to nightside redistribution on this presumably tidally locked planet (Figure 6.6). The best-fit total reradiation factor, f_{tot}, that results from a χ^2 analysis of all the eclipse depths for TrES-2b assuming a zero Bond albedo is $f_{tot} = 0.346^{+0.038}_{-0.037}$. Thus our Ks-band brightness temperature ($T_B = 1636^{+79}_{-88} \ K$) and reradiation factor $f_{Ks}=0.358^{+0.074}_{-0.072}$, reveal an atmospheric layer that is similar to, and perhaps slightly hotter, than the atmospheric layers probed by longer wavelength Spitzer observations ($T_B{\sim}1500 \ K$ from Spitzer/IRAC observations of TrES-2b [O'Donovan et al. 2010]). The Ks-band is expected to be at a minimum in the water opacity (Fortney et al., 2008; Burrows et al., 2008a), and thus our Ks-band observations are expected to be able to see deep into the atmosphere of TrES-2b. Our observations suggest that the deep, high pressure atmosphere of TrES-2b displays a similar temperature – perhaps a slightly warmer temperature – to lower pressure regions.

Another way of parameterizing the level of day-to-nightside heat redistribution is calculating the percentage of the bolometric luminosity emitted by the planet's dayside, L_{day}, compared to the nightside emission, L_{night}. Measurements of the thermal emission of a hot Jupiter at its blackbody peak provide a valuable constraint on the bolometric luminosity of the planet's dayside emission, and by inference its nightside emission (Barman, 2008). From simple thermal equilibrium arguments if TrES-2b has a zero Bond albedo and it is in thermal equilibrium with its surroundings it should have a total bolometric luminosity of $L_{tot} = 7.7{\times}10^{-5}L_{\odot}$. By integrating the luminosity per unit frequency of our best-fit blackbody model across a wide wavelength range we are able to calculate the percentage of the total luminosity reradiated by

the dayside as $\sim$69% ($L_{day} = 5.3 \times 10^{-5} L_\odot$). The remainder, presumably, is advected via winds to the nightside.

We compare the depth of our Ks-band eclipse and the Spitzer/IRAC eclipses (O'Donovan et al., 2010) to a series of planetary atmosphere models in Figure 6.7. This comparison is made quantitatively as well as qualitatively by integrating the models over the WIRCam Ks band-pass as well as the Spitzer/IRAC channels, and calculating the χ^2 of the thermal emission data compared to the models. We first plot blackbody models with an isotropic reradiation factor ($f=\frac{1}{4}$; blue dotted-line) and that of our best-fit value (f=0.346; grey dotted-line) these models have dayside temperatures of $T_{day}\sim$1496K and $T_{day}\sim$1622K, respectively. Both blackbody models provide reasonable fits to the data, although the latter model (f=0.346; χ^2=4.7) provides a definitively better fit than the former isothermal model ($f=\frac{1}{4}$; χ^2=9.1) as it better predicts our Ks-band emission and the Spitzer/IRAC 8.0 μm emission. This suggests that overall TrES-2b has a near-isothermal dayside temperature-pressure profile and is well-fit by a blackbody.

We thus also compare the data to a number of one-dimensional, radiative transfer, spectral models (Fortney et al., 2006, 2008) with different reradiation factors that specifically include or exclude gaseous TiO and VO into the chemical equilibrium and opacity calculations. In these models when TiO and VO are present they act as absorbers at high altitude and lead to a hot stratosphere and a temperature inversion (Hubeny et al., 2003). However, if the temperature becomes too cool (TiO and VO start to condense at 1670 K at 1 mbar [Fortney et al. 2008]), TiO and VO condense out and the models with and without TiO/VO are very similar. In the case of TrES-2b, for all the models we calculate, except our model that features dayside emission only ($f=\frac{1}{2}$), they do not harbour temperature inversions because the atmospheres are slightly too cool and TiO/VO has condensed out of their stratospheres. We plot models with TiO/VO and reradiation factors of $f=\frac{1}{4}$ (purple dotted line), f=0.31 (green dashed line), and $f=\frac{1}{2}$ (orange dotted line), and without TiO/VO with a reradiation factor of $f=\frac{1}{2}$ (cyan dot-dashed line). O'Donovan et al. (2010) argued that TrES-2b experienced a temperature inversion due to the high 4.5 μm emission compared to the low 3.6 μm emission, which was predicted to be a sign of water and CO in emission, rather than absorption, in TrES-2b's presumably inverted atmosphere. We also find that our models without a temperature inversion have difficultly matching the Spitzer/IRAC 5.6 and 8.0 μm thermal emission (χ^2=25.4 for $f=\frac{1}{4}$ with TiO/VO, χ^2=15.3 for f=0.31 with TiO/VO, and χ^2=5.5 for $f=\frac{1}{2}$ without TiO/VO). If the temperature inversion is due to TiO/VO, by the time the atmosphere becomes hot enough that TiO/VO remains in gaseous form, the thermal emission is too bright to fit the 3.6, and 5.8 μm thermal emission (χ^2=10.6 for $f=\frac{1}{2}$ with TiO/VO).

The combination of our blackbody and radiative transfer models with our own eclipse depth and those from the Spitzer/IRAC instrument (O'Donovan et al., 2010) thus suggest that the at-
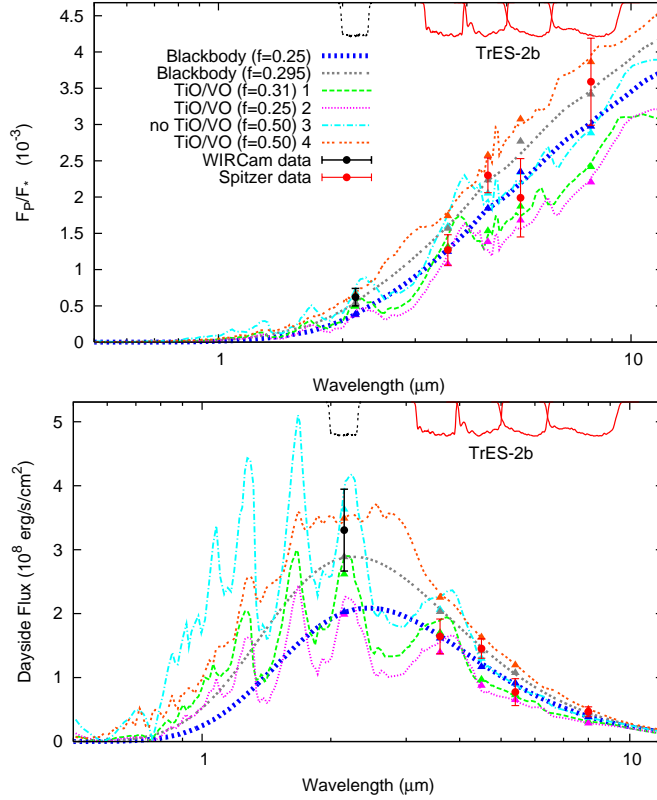
Figure 2.9 Dayside planet-to-star flux ratios (top) and dayside flux at the planet's surface (bottom). The Ks-band point (black point; $\sim 2.15\ \mu m$) is our own, while the Spitzer/IRAC red points are from O'Donovan et al. (2010). Blackbody curves for isotropic reradiation ($f=\frac{1}{4}$; $T_{eq}\sim 1496\ K$; blue dashed-line) and for our best-fit reradiation factor ($f=0.346$; $T_{eq}\sim 1622\ K$; grey dotted-line) are also plotted. We also plot one-dimensional, radiative transfer spectral models (Fortney et al., 2006, 2008) for various reradiation factors and with and without TiO/VO. The models with TiO/VO include $f=\frac{1}{4}$ (purple dotted line), $f=0.31$ (green dashed line), and $f=\frac{1}{2}$ (orange dotted line); only the last of the models has a temperature inversion. The model without TiO/VO features emission from the dayside only ($f=\frac{1}{2}$; cyan dot-dashed line). The models on the top panel are divided by a stellar atmosphere model (Hauschildt et al., 1999) of TrES-2 using the parameters from Torres et al. (2008) (M_*=0.98 $M_\odot$, R_*=1.00 $R_\odot$, T_{eff}=5850 K, and log g= 4.43). We plot the Ks-band WIRCam transmission curve (dotted black lines) and Spitzer/IRAC curves (solid red lines) inverted at arbitrary scale at the top of both panels.

mosphere of TrES-2b likely features modest redistribution of heat from the day to the nightside. It is unclear whether the atmosphere of TrES-2b requires a temperature inversion. A simple blackbody model (f=0.346 and T_{eq}~1622 K) provides an exemplary fit to the data; this may indicate that TrES-2b has a fairly isothermal dayside temperature structure, perhaps similar to HAT-P-1b (Todorov et al., 2010). An important caveat, on the above result is that our f=$\frac{1}{2}$ model without TiO/VO (χ^2=5.5) and thus without a temperature inversion returns nearly as good of fit as our best-fit blackbody model (f=0.346; χ^2=4.7); thermal emission measurements at other wavelengths, and repeated measurements at the above wavelengths, are thus necessary to differentiate a blackbody-like spectrum, from significant departures from blackbody-like behaviour, and to confirm that TrES-2b efficiently redistributes heat to the nightside of the planet. Specifically, the variations between the models displayed in Figure 6.7 are largest in the near-infrared J & H-bands and thus further near-infrared constraints – if they are able to achieve sufficient accuracy to measure the small thermal emission signal of TrES-2b in the near-infrared – should prove eminently useful to constrain the atmospheric characteristics of this planet.

If the excess emission at 4.5 μm is due to water emission, rather than absorption, due to a temperature inversion in the atmosphere of TrES-2b then the inversion is unlikely to be due to TiO/VO. This is because the atmosphere of TrES-2b appears too cool to allow TiO/VO to remain in gaseous form in its upper atmosphere. If there is a temperature inversion then the high altitude optical absorber is likely to be due to another chemical species than TiO/VO. For instance, Zahnle et al. (2009a) have investigated the photochemistry of sulphur-bearing species as another alternative.

TrES-2b is a promising target for the characterization of its thermal emission across a wide wavelength range. In addition to orbiting a relatively bright star, and having a favourable planet-to-star radius ratio, TrES-2 lies within the Kepler field. The combination of secondary eclipse measurements already published using Spitzer/IRAC, upcoming measurements with Kepler (~430 - 900 nm; Borucki et al. 2008), and J, H and K-band near-infrared measurements that could be obtained from the ground, will allow us to fully constrain TrES-2b's energy budget. At the shorter end of this wavelength range it should also be possible to constrain the combination of reflected light and thermal emission. Our results predict that even if the geometric albedo of TrES-2b is as low as 5% in the Kepler bandpass, if Kepler is able to detect the secondary eclipse of this planet then it will be detecting a significant fraction of reflected light in addition to thermal emission. This will largely break the degeneracy on the Bond albedo and the reradiation factor for this planet, facilitating a more complete understanding of its energy budget.

Chapter 3

Near-infrared Thermal Emission of TrES-3b

3.1 Abstract

We present H and Ks-band photometry bracketing the secondary eclipse of the hot Jupiter TrES-3b using the Wide-field Infrared Camera on the Canada-France-Hawaii Telescope. We detect the secondary eclipse of TrES-3b with a depth of $0.133^{+0.018}_{-0.016}\%$ in the Ks-band (8σ) - a result in sharp contrast to the eclipse depth reported by de Mooij & Snellen. We do not detect its thermal emission in H-band, but place a 3σ limit on the depth of the secondary eclipse in this band of 0.051%. A secondary eclipse of this depth in Ks requires very efficient day-to-nightside redistribution of heat and nearly isotropic reradiation, a conclusion that is in agreement with longer wavelength, mid-infrared Spitzer observations. Our 3σ upper-limit on the depth of our H-band secondary eclipse also argues for very efficient redistribution of heat and suggests that the atmospheric layer probed by these observations may be well homogenized. However, our H-band upper limit is so constraining that it suggests the possibility of a temperature inversion at depth, or an absorbing molecule, such as methane, that further depresses the emitted flux at this wavelength. The combination of our near-infrared measurements and those obtained with Spitzer suggest that TrES-3b displays a near isothermal dayside atmospheric temperature structure, whose spectrum is well approximated by a blackbody. We emphasize that our strict H-band limit is in stark disagreement with the best-fit atmospheric model that

results from longer wavelength observations only, thus highlighting the importance of near-infrared observations at multiple wavelengths in addition to those returned by Spitzer in the mid-infrared to facilitate a comprehensive understanding of the energy budgets of transiting exoplanets.

3.2 Introduction

Near-infrared secondary eclipse observations of hot Jupiters from the ground is a relatively new field. After a series of non-detections and increasingly more sensitive upper limits using photometry (Snellen 2005; Snellen & Covino 2007; Deming et al. 2007) and spectroscopy (Richardson et al. 2003; Knutson et al. 2007a), the field has been reinvigorated by a series of successful ground-based, photometric detections. Examples include: a $\sim6\sigma$ detection in Ks-band of TrES-3b using the William Herschel Telescope (WHT; de Mooij & Snellen 2009), a $\sim4\sigma$ detection in z'-band emission of OGLE-TR-56b using Magellan and the Very Large Telescope (VLT; Sing & Lopez-Morales 2009), a $\sim5\sigma$ detection at ~2.1 μm with the VLT (Gillon et al., 2009), a $\sim8\sigma$ detection in the Ks-band of CoRoT-1b using the Apache Point observatory (APO; Rogers et al. 2009), and a $\sim5\sigma$ detection of WASP-12b's z'-band emission also using the APO (Lopez-Morales et al., 2010). From our own program, we were able to report a $\sim5\sigma$ detection of thermal emission from the hot Jupiter TrES-2b in Ks-band (Croll et al., 2010a) using the Wide-field InfraRed Camera (WIRCam) on the Canada-France-Hawaii Telescope (CFHT).

Near-infrared measurements of the thermal emission of hot Jupiters are crucial to our understanding of the dynamics and radiative transfer in the atmospheres of these exotic worlds as these measurements sample their blackbody peaks. Such near-infrared measurements, when combined with secondary eclipse detections longward of $3\mu m$ with Spitzer, enable us to characterize these planets' pressure-temperature profiles and better understand their energy budgets. Specifically they facilitate an estimate of the bolometric luminosity of these planets' dayside emission (Barman, 2008), leading to a more complete understanding of how the planets reradiate the incoming stellar flux and advect this heat from the day to nightside at various depths and pressures.

One of the most favourable targets for ground-based measurements is the transiting hot Jupiter TrES-3b. It circles a G-type star in a ~31 hour orbit (O'Donovan et al., 2007). It is exposed to relatively high stellar insolation, with an incident flux of 1.7×10^9 $erg s^{-1} cm^{-2}$, and is thus a member of the hottest and mostly highly irradiated class (pM-class) of hot Jupiters according to the Fortney et al. (2008) theory. Its high equilibrium temperature ($T_{EQ}\sim1650$ K; assuming isotropic reradiation, and a zero Bond albedo) in combination with its relatively favourable planet-to-star radius ratio ($R_P/R_*\sim0.166$; Sozzetti et al. 2009), makes it a com-

pelling target for thermal emission measurements.

Thermal emission from this target has already been measured with Spitzer in the four IRAC (Fazio et al., 2004) channels (Fressin et al., 2010). Their best-fit eclipes are consistent with a circular orbit, and Fressin et al. (2010) place a 3σ limit on the eccentricity, e, and argument of periastron, ω, of $|ecos\omega| < 0.0056$. Despite the high incident stellar irradiation for this target, their secondary eclipse measurements are best-fit with an atmospheric model that efficiently redistributes heat. Also, as the 4.5 μm eclipse depth is less than the 3.6 μm depth, this suggests that this planet does not harbour a temperature inversion, as we are seeing water in absorption rather than emission at 4.5 μm. This is surprising, because highly irradiated hot Jupiters, such as TrES-3b, were expected to experience temperature inversions due to absorption of the incoming stellar flux from gaseous TiO/VO in a hot stratosphere (Hubeny et al., 2003; Fortney et al., 2006; Burrows et al., 2007; Fortney et al., 2008).

In the near-infrared, de Mooij & Snellen (2009) have reported a detection of TrES-3b's thermal emission in Ks-band using the LIRIS instrument on the WHT. The depth of their best-fit secondary eclipse was $0.241 \pm 0.043\%$, and this result argued in favour of very bright dayside emission and very inefficient redistribution of heat to the nightside of this planet, in sharp disagreement to the Spitzer results from longer wavelengths. However, the authors noted residual systematic noise during the ingress of the secondary eclipse that resulted in a deep, slightly eccentric best-fit eclipse. For these reasons we felt follow-up observations were warranted to confirm their measured eclipse depth.

A bright secondary eclipse in the near-infrared is reasonable, as simplified one-dimensional, radiative transfer models (Hubeny et al., 2003) suggest that one can expect hot Jupiters without temperature inversions to display increased thermal emission in the near-infrared. This makes intuitive sense as the decreased output in the mid-infrared allows the planet to shine more brightly at shorter wavelengths. On the other hand, near-infrared observations are expected to probe atmospheric layers that are more homogenized than the layers probed by longer wavelength observations. This is because the JHK near-infrared spectral bands occur at minima in the opacity of water where one should be able to see deeper into a planet's atmosphere than one can see in the mid-infrared with *Spitzer* (Seager et al., 2005b; Fortney et al., 2008; Burrows et al., 2008a). JHK-band observations should then probe higher pressure (P) atmospheric layers. At higher pressures it is expected that the radiative time-scale (how quickly the planet reradiates the incident stellar flux; τ_{rad}) will become of similar order to the advective timescale (how quickly the planet advects the heat to the nightside of the planet; τ_{adv}) leading to a more homogenized atmospheric layer (Seager et al., 2005b; Fortney et al., 2008). The reradiative timescale is thought to be proportional to pressure: $\tau_{rad} \sim \frac{Pc_P}{g4\sigma T^3}$ (Showman & Guillot, 2002), where T is the temperature, c_P is the specific heat capacity, σ is the Stefan-Boltzmann constant,

and g is the gravitational acceleration of the planet. The advective timescale, on the other hand, is thought to be approximated by the radius of the planet, R_P, divided by the horizontal wind speed, U: $\tau_{adv} \sim R_P/U$ (Showman & Guillot, 2002). For these reasons, as one probes higher pressure atmospheric layers, τ_{rad} should increase, and become of similar order to τ_{adv}; this has been confirmed by 3D models (Showman et al., 2009). For the near-infrared JHK bands we therefore may expect more efficient heat redistribution and that the near-infrared emission may be depressed, as the depths we probe may be more homogenized than the upper atmospheres of these planets. This behavior is difficult to capture for a 1D radiative-equilibrium model that assumes an average day-side temperature or planet-wide conditions. For these reasons near-infrared observations are crucial to inform our understanding of the underlying physics that govern hot Jupiter radiative transfer and atmospheric dynamics.

Here we present observations bracketing TrES-3b's secondary eclipse using WIRCam on CFHT. We report a 8σ detection of its Ks-band thermal emission of $0.133^{+0.018}_{-0.016}\%$ and place a 3σ upper limit on its thermal emission in H-band of 0.051%. We do not find that this planet radiates brightly in the near-infrared, as our Ks-band measurement and our H-band upper limit argue in favour of very efficient day-to-nightside redistribution and nearly isotropic reradiation of heat. These results are in clear contrast to the de Mooij & Snellen (2009) result, although we explain that under different assumptions their result is consistent with our own. Our H-band limit is so constraining that it suggests that the layer of the atmosphere probed by this wavelength is very well homogenized and that there may be a temperature inversion deep in this planet's atmosphere, or that the emitted flux is depressed at this wavelength due to a wide absorption band near 1.6 μm.

3.3   Observations and data reduction

We observed the secondary eclipse of TrES-3 ($K=10.608$, $H=10.655$) on two occasions with WIRCam on CFHT (Puget et al., 2004). On 2009 June 3 we observed TrES-3 using a Ks-band filter and on 2009 June 6 we observed it again using an H-band filter. Both observations were taken under photometric conditions and lasted for $\sim$3.1 hours for our Ks observations and $\sim$2.8 hours for our H-band observations, evenly bracketing the predicted secondary eclipse. On both occasions numerous reference stars were also observed in the 21x21 arcmin field of view of WIRCam. The telescope was defocused to 1.0mm, resulting in the flux of our target star being spread over a ring 13 pixels in diameter (4") on our array. We used "stare" mode on CFHT where the target star is observed continuously without dithering for the duration of the observations.

We used 5-second exposures for our Ks-band observations. The effective duty cycle after
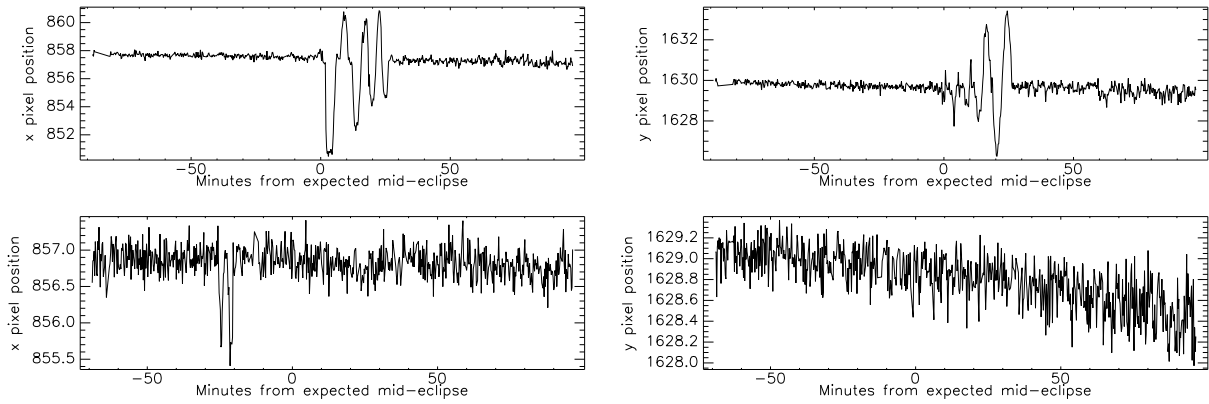
Figure 3.1 The x and y position of the centroid of the PSF of the target star, TrES-3, with time for our Ks-band photometry (top panels) and our H-band photometry (bottom panels).
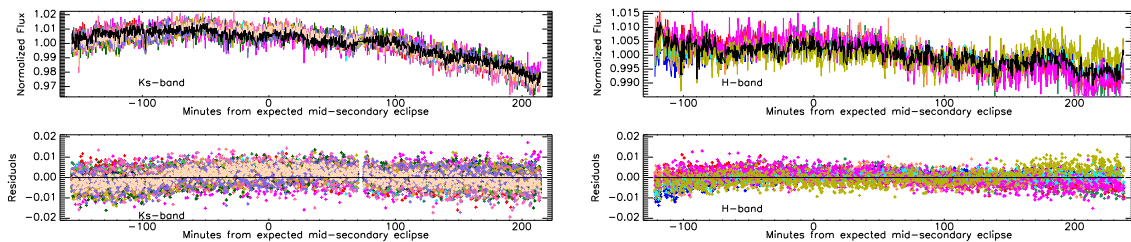
Figure 3.2 Top panels: The flux from the target star (black) and the reference stars (various colours) that are used to calibrate the flux of TrES-3b for our Ks-band photometry (left) and our H-band photometry (right). Bottom panels: The residuals from the normalized flux of the target star of the normalized flux of the reference stars for the Ks-band (left) and H-band photometry (right).

accounting for readout and for saving exposures was 33%. Following the observations we noted significant drifts in the centroid of the stellar point-spread-function (PSF) of TrES-3 as well as other stars on the chip (Figure 3.1 top panels).

For our H-band observations, and subsequent observations in our program, to counteract these drifts we initiated a corrective guiding "bump" before every image cube to ensure that our target star fell as often as possible on or near the original pixel. Following this corrective "bump" the drifts on the chip were significantly reduced (Figure 3.1 bottom panels). To counteract the extra overheads that this "bump" induced, we observed in "cubes" of multiple images in each FITS files. Thus, for our H-band observations we obtained data-cubes each containing twelve 5-second exposures. The effective duty cycle after accounting for readout and for saving exposures was 43%.

For both sets of data the images were reduced and aperture photometry was performed on our target star and all unsaturated, reasonably bright reference stars on the WIRCam array as discussed in Croll et al. (2010a). Exceptions include that we do not modify the shape of the annulus used to calculate the sky aperture, and that we do not correct the flux of our targets for the x or y positions of the centroid of the stellar PSF. We used an aperture with a radius of 11 pixels for our Ks-band photometry, and an aperture with a radius of 10.5 pixels for our H-band photometry. To estimate the residual background flux for both sets of photometry, we used an annulus with an inner radius of 18 pixels and an outer radius of 28 pixels. We tested larger and smaller apertures in increments of 0.5 pixels, and confirmed that these sizes of apertures returned optimal photometry.

For our H-band photometry pixels in the annulus produced by our defocused target star occasionally saturated, and were removed in the preprocessing step; similar saturation issues were noted with some of our reference stars as well. It was difficult to account for the discrepancy in flux that resulted from these saturated pixels at the precision required for these observations; thus, observations in which a pixel near our target star was saturated were excluded from the resulting analysis. 62 of our 718 H-band observations ($\sim$8.6% of the total) were cut as a result of this step. Saturation was not an issue in the 740 exposures for our Ks-band photometry.

As with our previous near-infrared CFHT/WIRCam photometry (Croll et al., 2010a), the resulting light curves displayed significant, systematic variations in intensity (see the top panels of Figure 3.2), possibly due to changes in atmospheric transmission, seeing and airmass, guiding errors and/or other effects. These variations in the flux of our target star were then corrected by normalizing the flux of the target star by 9 reference stars in Ks-band and 10 in H-band using the method discussed in Croll et al. (2010a). This method entails using the reference stars that showed the smallest deviation from the target star outside of the expected secondary eclipse to correct the flux of our target star. As a result of these corrections (and the removal of
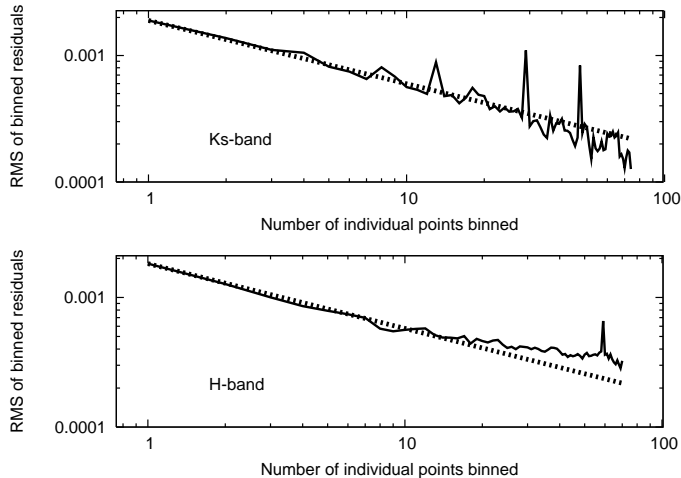
Figure 3.3 The root-mean-square of our out-of-eclipse photometry (solid line) for various number of binned points following the various corrections documented in §6.3 for our Ks-band photometry (top) and our H-band photometry (bottom). In both cases the dashed line displays the one over the square-root of the bin-size expectation for Gaussian noise.

a linear-trend with time for the sake of this comparison only), the point-to-point scatter of our data outside of occultation improved from a root-mean-square of 13.8×10^{-3} to 1.60×10^{-3} in Ks and 5.9×10^{-3} to 0.84×10^{-3} in H per 60 seconds (Figure 3.2). We should note that we are still well above the predicted photon noise RMS limit of 3.7×10^{-4} for Ks-band, and 2.7×10^{-4} for H-band per 60 seconds. We set the uncertainty on our measurements as the RMS of the out of eclipse photometry after the removal of a linear-trend with time. We also bin our out-of-eclipse photometry following the above reduction and compare it to the one-over-the square-root of the number of binned points expectation for Gaussian noise. Although our Ks-band data scales down near this limit, our H-band data display systematics that result in the data scaling down marginally above this limit (Figure 6.2). This suggests that there is an extra systematic in our H-band photometry that merits further investigation.

3.4 Analysis

Similarly to a number of our near-infrared photometric data-sets taken with CFHT/WIRCam (Croll et al., 2010a, 2011), our Ks-band photometry following the reduction exhibited an obvious background trend, B_f, with a near-linear slope. The H-band photometry also displayed a less obvious background trend. Although these trends could be intrinsic to TrES-3, the frequency with which we find such background trends with our other near-infrared photometric data-sets suggests that they are systematic in origin. We thus fit both data-sets independently with a
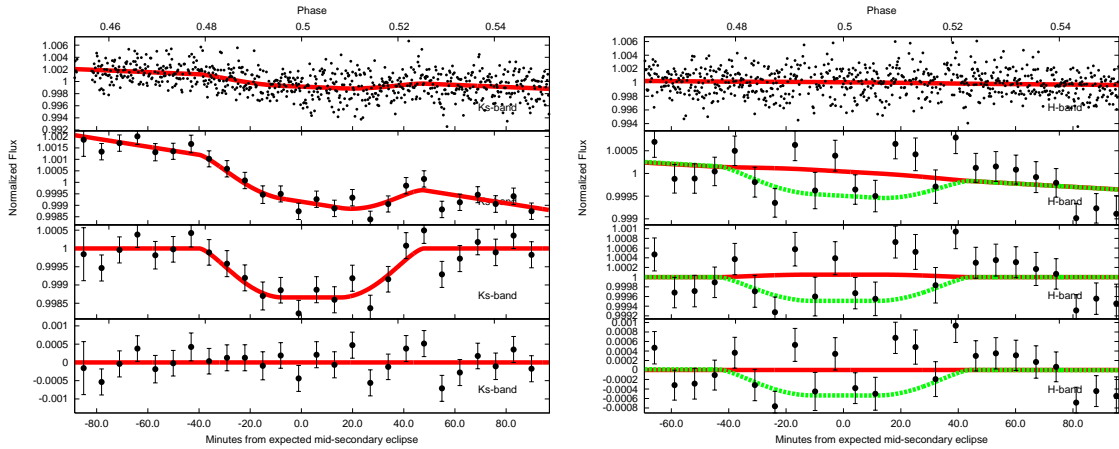
Figure 3.4 WIRCam/CFHT photometry bracketing the secondary eclipse of TrES-3b in Ks-band (left) and H-band (right). The top panels show the unbinned light curves, the panel that is second from the top shows the light curves with the data binned every 7.0 minutes. The panel that is the second from the bottom shows the binned data after the subtraction of the best-fit background trends, B_f (the slope), while the bottom panels show the binned residuals from the best-fit model of each eclipse. In each one of the panels the best-fit secondary eclipse and background trend, B_f, is shown with the red line. For our H-band photometry at right we also display the depth of the secondary eclipse that we are able to rule out at 3σ (green dotted-line). As displayed in Table 6.1 the best-fit secondary eclipse in H-band (right panel) has a small negative depth (thus representing an unphysical brightening).
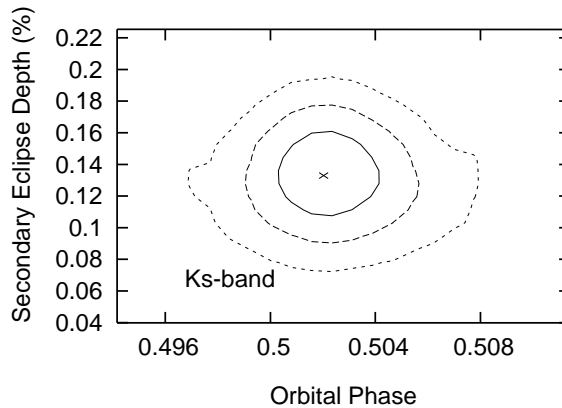
Figure 3.5 The 68.3% (1σ; solid-line), 95.5% (2σ; dashed-line) and 99.7% (3σ; short dashed-line) credible regions from our MCMC analysis for our Ks-band photometry comparing the secondary eclipse depth, ΔF, and the best-fit phase, ϕ. The "x" in the middle of the plot denotes the best-fit point from our MCMC analysis.

Table 3.1.   TrES-3b's best-fit secondary eclipse parameters

Parameter	MCMC Ks-band Solution	"Residual permutation" Ks-band solution	MCMC H-band Solution	"Residual permutation" H-band solution	Bootstrap H-band solution
reduced χ^2	$1.044^{+0.006}_{-0.001}$	$1.037^{+0.004}_{-0.138}$	$1.131^{+0.006}_{-0.000}$	$1.123^{+0.024}_{-0.008}$	$1.128^{+0.002}_{-0.004}$
ΔF (%)	$0.133^{+0.018}_{-0.016}$	$0.132^{+0.012}_{-0.010}$	$-0.002^{+0.015}_{-0.019}$	$0.011^{+0.019}_{-0.040}$	$-0.003^{+0.018}_{-0.018}$
3σ upper limit on ΔF (%)	< 0.185	< 0.154	< 0.047	< 0.045	< 0.051
t_{offset} (min)[a]	$3.4^{+2.7}_{-1.9}$	$3.6^{+1.8}_{-2.2}$	0.0[b]	-0.0[b]	-0.4[b]
$t_{eclipse}$ (HJD-2440000)	$14985.9542^{+0.0019}_{-0.0013}$	$14985.9543^{+0.0013}_{-0.0015}$	14989.8703[b]	14989.8703[b]	14989.8701[b]
c_1	$0.00212^{+0.00017}_{-0.00016}$	$0.00211^{+0.00010}_{-0.00009}$	$0.00032^{+0.00013}_{-0.00018}$	$0.00010^{+0.00055}_{-0.00003}$	$0.00029^{+0.00016}_{-0.00015}$
c_2 (d^{-1})	$-0.025^{+0.002}_{-0.002}$	$-0.025^{+0.001}_{-0.001}$	$-0.005^{+0.002}_{-0.002}$	$-0.004^{+0.002}_{-0.006}$	$-0.005^{+0.002}_{-0.002}$
ϕ [a]	$0.5020^{+0.0014}_{-0.0010}$	$0.5021^{+0.0010}_{-0.0012}$	0.5002[b]	0.5002[b]	0.0000[b]
$e\cos(\omega)$	$0.0029^{+0.0022}_{-0.0022}$	$0.0030^{+0.0015}_{-0.0015}$	0.0000[b]	-0.0000[b]	-0.0003[b]
T_B (K)	1731^{+56}_{-60}	1727^{+39}_{-41}	n/a	n/a	n/a
3σ upper limit on T_B (K)	< 1887	< 1799	< 1635	< 1622	< 1658
f	$0.303^{+0.042}_{-0.040}$	$0.300^{+0.029}_{-0.028}$	n/a	n/a	n/a
3σ upper limit on f	< 0.429	< 0.354	< 0.242	< 0.234	< 0.255

[a]We account for the increased light travel-time in the system (Loeb, 2005).

[b]By assumption.

secondary eclipse model and a linear background of the form:

$$B_f = 1 + c_1 + c_2 dt \qquad (3.1)$$

where dt is the time interval from the beginning of the observations. As in Croll et al. (2010a) we fit for the best-fit secondary eclipse and background using Markov-Chain Monte Carlo methods (Christensen et al. 2001; Ford 2005; described for our purposes in Croll 2006). We use a 5×10^6 step MCMC chain. We fit for c_1, c_2, the depth of the secondary eclipse, ΔF, and the mid-eclipse phase, ϕ. We also quote the offset that the eclipse occurs later than the expected eclipse center, t_{offset}[1], as well as the best-fit mid-eclipse heliocentric (UTC) Julian Date, $t_{eclipse}$. We use the Mandel & Agol (2002) algorithm without limb darkening to generate our best-fit secondary eclipse model. We obtain our stellar and planetary parameters for TrES-3 from Sozzetti et al. (2009).

The results from these fits for the Ks and H-band photometry are presented in Table 6.1. The best-fit secondary eclipse models are presented in Figure 3.4. The phase dependence of the best-fit secondary eclipse for our Ks-band photometry is presented in Figure 6.4. For our H-band photometry we are unable to detect the secondary eclipse. Thus for our H-band analysis that follows we artificially restrict the eccentricity of TrES-3b to 0, and thus we do not fit for the eclipse phase, ϕ.

To determine the effect of systematic noise in the derived eclipse parameters we also fit our data using the "residual-permutation" method (Winn et al., 2009), described for our purposes in Croll et al. (2010a). For our H-band data we also perform 8000 iterations of a bootstrap method that randomly scrambles the residuals and refits the data. The results from all these methods are presented in in Table 6.1. For our Ks-band data, as the "residual permutation" and the MCMC analyses result in similar uncertainties we quote the MCMC errors for the rest of the paper. For our H-band data, the bootstrap method returns the most conservative upper limit, and we thus quote this limit for the rest of the paper. We also present this 3σ upper-limit on the eclipse depth in Figure 3.4.

We note that for our Ks-band data specifically we also explored a quadratic expression for the background term, B_f: $B_f = 1 + c_1 + c_2 dt + c_3 dt^2$, where c_3 is also a fit parameter. A background of this term returned similar eclipse parameters to that of our linear background fit, and thus we quote our linear background MCMC fit henceforth.
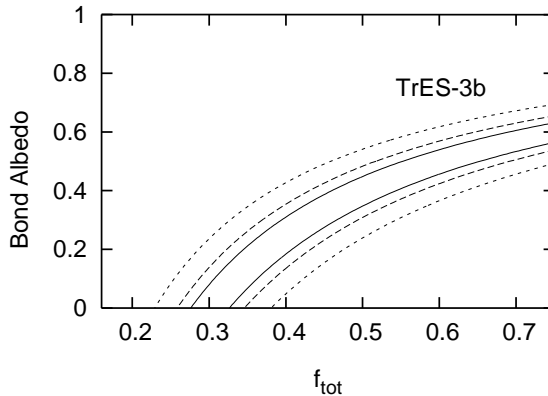
Figure 3.6 The 68.3% (1σ; solid-line), 95.5% (2σ; dashed-line) and 99.7% (3σ; short dashed-line) χ^2 confidence regions on the total reradiation factor, f_{tot}, and Bond albedo from the combination of our Ks-band point, the reanalyzed Ks-band de Mooij & Snellen (2009) point discussed here, and the Spitzer/IRAC measurements (Fressin et al., 2010).

3.5   Discussion

The depth of our best-fit secondary eclipse in Ks-band is $0.133^{+0.018}_{-0.016}\%$, with a reduced χ^2 of 1.044. We discuss the implications of this detection combined with the other thermal emission constraints for this system in §3.5.1. In H-band we are unable to detect the secondary eclipse and discuss the implications of this in §3.5.2. We then compare these observations to atmospheric models in §5.5.4, and discuss the future prospects for this system in §3.5.4.

3.5.1   TrES-3b's Ks-band thermal emission

Our Ks-band best-fit secondary eclipse is consistent with a circular orbit; the offset from the expected eclipse center is: $t_{offset} = 3.4^{+2.7}_{-1.9}$ minutes (or at a phase of $\phi = 0.5020^{+0.0014}_{-0.0010}$). This corresponds to a limit on the eccentricity and argument of periastron of $e\cos\omega = 0.0029^{+0.0022}_{-0.0022}$, or a 3σ limit of $|e\cos\omega| < 0.0101$. Our result is consistent with the more sensitive $e\cos\omega$ limits reported by Fressin et al. (2010) from the secondary eclipse detections at the four Spitzer/IRAC wavelengths. Our result therefore supports the conclusion of Fressin et al. (2010) that the "puffed-up" radius of TrES-3b is unlikely to be due to tidal damping of the orbital eccentricity.

A secondary eclipse of $0.133^{+0.018}_{-0.016}\%$ corresponds to a Ks-band brightness temperature of $T_{BKs} = 1731^{+56}_{-60}$ K assuming a stellar effective temperature of $T_{eff} = 5650 \pm 75$ (Sozzetti et al., 2009). This compares to an equilibrium temperature $T_{EQ}\sim1650$ K assuming isotropic reradiation, and a zero Bond albedo.

We should note that our Ks-band detection is discrepant from the de Mooij & Snellen (2009)

---

[1] we take into account the 22 s delay due to light travel-time in the system [Loeb 2005]

Ks-band detection of $0.241 \pm 0.043\%$. Our measurement is approximately half of their value, and is discrepant by more than 2σ. The best explanation for this discrepancy is the impact of systematic uncertainties for observations in the near-infrared; de Mooij & Snellen (2009) specifically mention several discrepant points at the beginning of their best-fit eclipse that both increase the depth of their eclipse and lead to an eccentric eclipse center ($\phi = 0.4958 \pm 0.0027$). If the planet is assumed to have zero eccentricity, in accordance with the Spitzer results and our own, and these discrepant points are excluded, then the resulting best-fit eclipse is: $\Delta F_{WHT} = 0.174 \pm 0.046\%$ (Ernst de Mooij & Ignas Snellen, personal communication). Thus our two measurements are consistent within 1σ under these assumptions. Any remaining variation between our two eclipse depths is likely statistical in nature, or could be due to eclipse variability between our observations and theirs. The difference in our two eclipse depths would necessitate a change in the brightness temperature of only $\sim 100K$.

Our Ks-band secondary eclipse depth, when combined with the secondary eclipse depths at the Spitzer/IRAC wavelengths from Fressin et al. (2010) and the de Mooij & Snellen (2009) reanalyzed eclipse depth quoted above, is consistent with a range of Bond albedos, A_B, and efficiencies of the day to nightside redistribution of heat on this presumably tidally locked planet (Figure 6.6). We parameterize the level of redistribution from the day to nightside by the reradiation factor, f, following the Lopez-Morales & Seager (2007) definition, which relates the dayside temperature of the planet, T_p to the stellar effective temperature (T_*), stellar radius (R_*), and semimajor axis of the planet (a): $T_p = T_* \ (R_*/a)^{1/2}[f(1 - A_B)]^{1/4}$, in the absence of any intrinsic flux (which for hot Jupiters is much smaller than the absorbed and reradiated stellar flux). From a theoretical perspective, one expects that the total reradiation factor, f_{tot}, of a hot Jupiter's atmosphere should fall between isotropic reradiation ($f_{tot}=\frac{1}{4}$), and no redistribution ($f_{tot}=\frac{2}{3}$; Burrows et al. 2008b). For reference $f_{tot}=\frac{1}{2}$ denotes redistribution and reradiation from the dayside-face only. However, the reradiation factors of individual atmospheric layers may fall well below or above these levels, as f in this case simply relates the properties of the system (T_*, R_*, and a) to the brightness temperature of the atmospheric layer probed by that wavelength of observations.

For our Ks-band observations, if we assume a Bond albedo near zero, consistent with observations of other hot Jupiters (Charbonneau et al., 1999; Rowe et al., 2008) and with model predictions (Burrows et al., 2008a), we find a reradiation factor of $f_{Ks} = 0.303^{+0.042}_{-0.040}$ from our Ks-band eclipse photometry only, indicative of relatively efficient advection of heat from the day-to-nightside at this wavelength. Our Ks-band reradiation factor, f_{Ks}, is consistent with the reradiation factor that results from combining our eclipse depth with that of the Spitzer/IRAC depths and the de Mooij & Snellen (2009) measurement quoted above. The best-fit total reradiation factor, f_{tot}, that results from a χ^2 analysis of all the eclipse detections for TrES-3b (and

thus excluding our H-band limit) assuming a zero Bond albedo is $f_{tot} = 0.301^{+0.026}_{-0.025}$.

Another way of parameterizing this redistribution is by comparing the bolometric dayside luminosity, L_{day}, of the hot Jupiter to its nightside bolometric luminosity, L_{night}. Simply by following elementary thermal equilibrium calculations one can deduce that TrES-3b should display a total bolometric luminosity of $L_{tot} = 12.5 \times 10^{-5} L_{\odot}$, assuming it is in thermal equilibrium with its surroundings and has zero Bond albedo. For our $f_{tot} = 0.301$ blackbody model the dayside luminosity is $L_{day} = 7.5 \times 10^{-5} L_{\odot}$, suggesting that $\sim 60\%$ of the incident heat on this planet is reradiated by the dayside, leaving $\sim 40\%$ to be advected to the nightside.

3.5.2   An upper-limit on TrES-3b's H-band thermal emission

In H-band we are able to place a 3σ upper-limit on the depth of the secondary eclipse of ΔF_H $< 0.051\%$. The 3σ upper limit on the H-band brightness temperature is $T_{BH} < 1658$ K, a limit nearly as low as the equilibrium temperature of TrES-3b ($T_{EQ} \sim 1650K$) assuming a zero Bond albedo and isotropic reradiation. The associated reradiation factor for the atmospheric layer probed by our H-band observations is $f_H < 0.255$. Presuming that our limit does not suffer from systematic effects that we have not accounted for, the H-band brightness temperature of TrES-3 is remarkably low.

One possibility to explain the less-luminous dayside emission (weak H-band flux) of TrES-3b is that the albedo of TrES-3b is significantly non-zero, as has been conjectured for a number of hot Jupiters by Cowan & Agol (2011). If this conjecture is true for this planet then the observed thermal emission is not due to the planet reradiating nearly isotropically, but due to inefficient redistribution of heat after a significant fraction of the light is reflected (the allowed parameter space in the right-half of Figure 6.6). As mentioned above, a significantly non-zero albedo has been ruled out for all other hot Jupiters for which in-depth investigations have been performed. Nonetheless TrES-3b remains an attractive target for optical, reflected light observations.

More likely possibilities to explain the reduced H-band emission are that we are probing an atmospheric depth of TrES-3b that is well-homogenized, or that we are seeing a wide absorption band near this wavelength that is depressing the observed flux. Simplified one-dimensional atmospheric models (Fortney et al., 2008) suggest that we should be seeing deeper in the atmosphere in H-band than in Ks. Our measurements, taken at face value, imply that the atmosphere is modestly colder deeper down – that is, we are seeing a small temperature inversion deep in the atmosphere (and thus at a depth much greater than the temperature inversions seen by others in the Spitzer/IRAC bands). Perhaps this inversion is due to efficient homogenization at high pressures where the advective timescale may be of similar order to the radiative timescale (Fortney et al., 2008). Alternatively, for the absorption band possibility, there could be a strong opacity source that is blocking our anticipated H-band opacity window, and we are actually

seeing high in the atmosphere (low P) where the gas is colder. We find the former explanation compelling, but also explore the latter possibility of an additional opacity source and a wide absorption band.

One possibility for a chemical that could be causing such absorption is methane, which has an absorption band at around 1.7 μm, which could, in principle, shave off flux from the red edge of the planet's H-band flux. Such an absorption feature was recently detected in the emission spectrum of HD 209458 from the dayside of this planet (Swain et al., 2009b), and was attributed to methane. For comparison, the L-type brown dwarfs, which reach down to $T_{\rm eff} \sim 1350$ K (Cushing et al., 2008; Stephens et al., 2009), show no evidence for methane in the near-infrared, but the T-type spectral class below 1350 K shows methane absorption in the near-infrared - indeed, that is the definition of the new spectral class. Due to the planet's relatively high temperatures, detectable methane in the atmosphere of TrES-3b is not expected from considerations of equilibrium chemistry (Lodders & Fegley, 2002) or non-equilibrium chemistry including vertical mixing (Saumon et al., 2007). Photochemical models of hot Jupiter atmospheres show that methane is also readily destroyed by the incident stellar flux (Zahnle et al., 2009b). However, these various chemical models are not yet verified for hot Jupiters, so methane absorption cannot be excluded at this time. If methane is present in a large enough quantity to suppress the H-band flux, it would significantly affect the opacities and thus the emitted flux at other wavelengths as well, particularly at 3.3 and 8 μm, thus affecting conclusions on the efficiency of day-to-nightside redistribution and the presence, or lack thereof, of a temperature inversion for this planet. We encourage further modelling to explore this possibility.

3.5.3   Comparisons to atmospheric models

We compare the depth of our Ks-band eclipse, and our H-band 3σ upper-limit on the eclipse depth, to a series of planetary atmosphere models in Figure 6.7. We include the Spitzer/IRAC eclipse depths reported by Fressin et al. (2010), the revised de Mooij & Snellen (2009) eclipse depth reported above, and the limits on thermal emission and reflected light at shorter wavelengths of Winn et al. (2008b). This comparison is made qualitatively as well as quantitatively by integrating the models over the WIRCam H & Ks bandpasses as well as the Spitzer/IRAC channels and the WHT/LIRIS Ks-bandpass, and calculating the χ^2 of the thermal emission data compared to the models. We specifically exclude and then include our H-band upper limit, χ^2_{NoH} and χ^2_H, respectively, as this upper limit is difficult to reconcile with the below models.

For the data longward of 2 μm the eclipse depths are relatively well-fit by blackbody models featuring an isotropic reradiation factor ($f=\frac{1}{4}$; blue dotted line; χ^2_{NoH}=19.0), or our best-fit
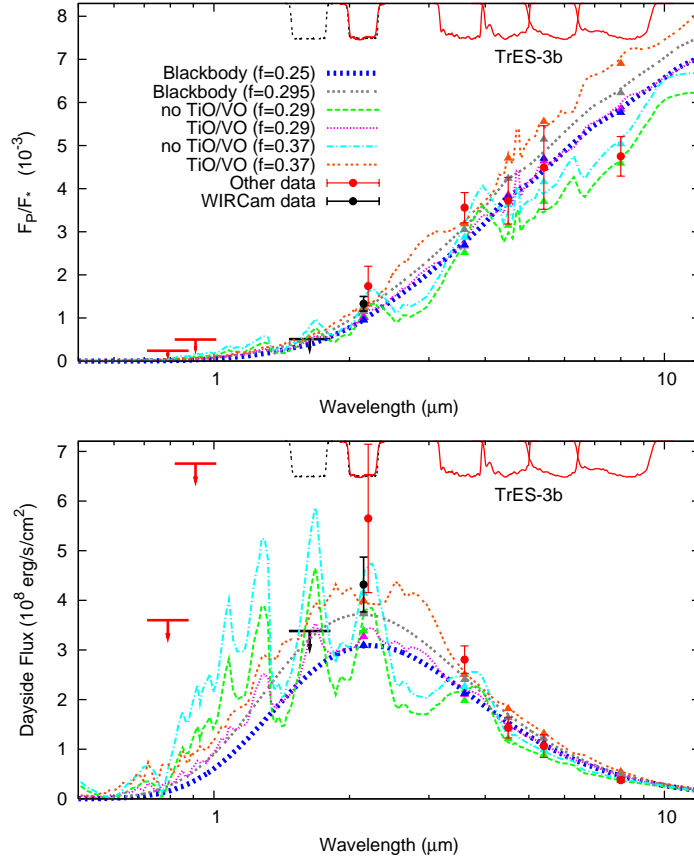
Figure 3.7 Dayside planet-to-star flux ratios (top) and dayside flux at the planet's surface (bottom). The Ks-band point ($\sim2.15\ \mu m$) and H-band 3σ upper limit (black point and black downward arrow) are our own, while the red points are the Spitzer/IRAC eclipses from Fressin et al. (2010), and the WHT eclipse depth from the de Mooij & Snellen (2009) reanalyzed photometry as quoted above. We also present the 90% upper-limits obtained by Winn et al. (2008b) short of 1 μm (red downward arrows). Blackbody curves for isotropic reradiation ($f=\frac{1}{4}$; $T_{eq}\sim1650$ K; blue dashed-line) and our best-fit total reradiation factor ($f=0.301$; $T_{eq}\sim1728$ K; grey dotted-line) are also plotted. We also plot one-dimensional, radiative transfer spectral models (Fortney et al., 2006, 2008) for various reradiation factors and with and without TiO/VO. We plot models with reradiation factors of $f=0.37$ with and without TiO/VO (orange dotted and cyan dot-dashed lines, respectively), and with close to isotropic reradiation ($f=0.29$) with and without TiO/VO (magenta dotted and green dashed lines, respectively). Both models with TiO/VO display temperature inversions. The models on the top panel are divided by a stellar atmosphere model (Hauschildt et al., 1999) of TrES-3 using the parameters from Sozzetti et al. (2009) ($M_*=0.928\ M_\odot$, $R_*=0.829\ R_\odot$, $T_{eff}=5650\ K$, and log $g=$ 4.4). We plot the Ks and H-band WIRCam transmission curves (black dotted curves), as well as the Spitzer/IRAC and WHT/LIRIS Ks-band transmission curves (red solid curves) inverted at arbitrary scale at the top of both panels. As the WHT/LIRIS Ks-band transmission curve is nearly identical to the CFHT/WIRcam Ks-band transmission curve, we offset the WHT/LIRIS point slightly in wavelength for clarity.

reradiation value ($f = 0.301$; grey dotted-line; χ^2_{NoH}=16.6). These models have dayside temperatures of $T_{day} \sim 1650K$ and $T_{day} \sim 1728K$, respectively. Blackbody models that fit the wavelength range between ~ 2 and $\sim 7~\mu m$, overpredict the 8 μm flux compared to the Spitzer/IRAC eclipse depth at this wavelength. We thus also compare these thermal emission measurements to a series of one-dimensional, radiative transfer, spectral models (Fortney et al., 2005, 2006, 2008) with different reradiation factors that specifically include or exclude gaseous TiO/VO into the chemical equilibrium and opacity calculations. In these models when TiO/VO are present in gaseous form in the upper atmosphere they act as absorbers at high altitudes and lead to hot stratospheres and temperature inversions (Hubeny et al., 2003). We present models with reradiation factors of f=0.29, and f=0.37, both with and without TiO/VO. Both the models with TiO/VO display temperature inversions. The brighter of these two inverted atmosphere models (f=0.37; orange dotted line) is a close match to our own Ks-band point, but is generally too hot for the Spitzer wavelengths and is thus demonstrably inconsistent with the data (χ^2_{NoH}=29.1). The fainter of these two models with TiO/VO (f=0.29; magenta dotted line) is a reasonable fit to some wavelengths, but is marginally discrepant from the Spitzer 8.0 μm point (χ^2_{NoH}=18.4). The models without temperature inversions are superior to those with inversions at 2.0 μm and longer. The best-fit model is the f=0.37 model without TiO/VO (cyan dot-dashed line; χ^2_{NoH}=5.6), which provides a quantitatively and qualitatively better fit than the f=0.29 model (green dashed line; χ^2_{NoH}=16.1). The differences are most obvious in the 3.6 μm channel, but the model better predicts the other bands as well. This thus suggests that a model without a temperature inversion with modest day-to-nightside redistribution provides an excellent fit to the measured eclipse depths at 2.0 μm and longward.

However, the preceding discussion completely ignored our strict H-band upper limit. This is appropriate if the low level of emitted flux at this wavelength is due to an absorption band from a species that we do not include, or do not include at the correct concentrations, in our model atmosphere. Nonetheless, we calculate the χ^2 of our models including the H-band limit, χ^2_H. For reference, the predicted H-band flux from our best-fit blackbody model is 0.051%, a value we are able to exclude nearly at 3σ. The χ^2 of our former best-fit model (f=0.37 without TiO/VO) becomes much worse (χ^2_H=21.1), because our non-inverted atmospheric model predicts elevated flux in H-band (actually the higest flux in H-band of any of the models we present). The hottest model with the temperature inversion (f=0.37 with TiO/VO) remains a poor fit (χ^2_H=39.7), but the cooler models (f=0.29) with and without TiO/VO are nearly statistically indistinguishable from our best-fit model (χ^2_H=25.6 with TiO/VO, and χ^2_H=25.7 without TiO/VO). Our blackbody models actually provide very similar fits to these models, as these simple models predict much lower emission in H-band, consistent with our strict upper-limit (χ^2_H=26.8 for our blackbody model with f=$\frac{1}{4}$, and χ^2_H=28.7 for our blackbody model with

f=0.301). If the pressure-temperature profile of the atmosphere is more nearly isothermal than predicted by models, then the differences between emission peaks and troughs will be muted, leading to more blackbody-like emission spectrum – we find this explanation compelling for TrES-3b.

3.5.4 Future prospects

Our near-infrared observations of this planet's secondary eclipse clearly show the need for multi-wavelength observations to develop a complete understanding of the energy budgets of hot Jupiters. In addition, detections of secondary eclipses in multiple near-infrared bands for multiple planets opens the door of a comparative study of hot Jupiters and brown dwarfs at similar T_{eff}, to better understand how heating from above, versus heating from below, affects the temperatures and chemistry of these objects. We will shortly reconfirm or improve upon our H-band upper limit by observing TrES-3b in this band again, to continue to facilitate a greater understanding of this planet's reradiation, and advection of heat at various depths and pressures in its exotic atmosphere.

Chapter 4

Detections of the Thermal Emission of WASP-12b in Ks, H & J

4.1   Abstract

We present Ks, H & J-band photometry of the very highly irradiated hot Jupiter WASP-12b using the Wide-field Infrared Camera on the Canada-France-Hawaii telescope. Our photometry brackets the secondary eclipse of WASP-12b in the Ks and H-bands, and in J-band starts in mid-eclipse and continues until well after the end of the eclipse. We detect its thermal emission in all three near-infrared bands. Our secondary eclipse depths are $0.309^{+0.013}_{-0.012}\%$ in Ks-band (24σ), $0.176^{+0.016}_{-0.021}\%$ in H-band (9σ) and $0.131^{+0.027}_{-0.029}\%$ in J-band (4σ). All three secondary eclipses are best-fit with a consistent phase, ϕ, that is compatible with a circular orbit: $\phi=0.4998^{+0.0008}_{-0.0007}$. The limits on the eccentricity, e, and argument of periastron, ω, of this planet from our photometry alone are thus $|ecos\omega| < 0.0040$. By combining our secondary eclipse times with others published in the literature, as well as the radial velocity and transit timing data for this system, we show that there is no evidence that WASP-12b is precessing at a detectable rate, and show that its orbital eccentricity is likely zero. Our thermal emission measurements also allow us to constrain the characteristics of the planet's atmosphere; our Ks-band eclipse depth argues strongly in favour of inefficient day to nightside redistribution of heat and a low Bond albedo for this very highly irradiated hot Jupiter. The J and H-band brightness temperatures are slightly cooler than the Ks-band brightness temperature, and thus hint at the possibility of a modest temperature inversion deep in the atmosphere of WASP-12b; the high

pressure, deep atmospheric layers probed by our J and H-band observations are likely more homogenized than the higher altitude layer probed by our Ks-band observations. Lastly, our best-fit Ks-band eclipse has a marginally longer duration than would otherwise be expected; this may be tentative evidence for material being tidally stripped from the planet – as was predicted for this system by Li & collaborators, and for which observational confirmation was recently arguably provided by Fossati & collaborators.

4.2   Introduction

Multiwavelength constraints on the thermal emission of hot Jupiters are crucial to precisely defining the spectral energy distributions of these planets and understanding their energy budgets. Interestingly most hot Jupiter thermal emission detections to date have not been at the blackbody peaks of these planets, but at longer wavelengths with the Spitzer Space Telescope ($\lambda > 3$ μm; e.g. Charbonneau et al. 2005; Deming et al. 2005). Probing shorter near-infrared wavelengths at the blackbody peaks of these planets has only recently been proven feasible first through space-based observations with the Hubble Space Telescope (HST; Swain et al. 2009a), and then from the ground (e.g. de Mooij & Snellen 2009; Sing & Lopez-Morales 2009; Gillon et al. 2009). Our program to detect near-infrared thermal emission from the hottest of the hot Jupiters has also been successful using the Wide-field Infrared Camera (WIRCam) on the Canada-France-Hawaii Telescope (CFHT) to detect the Ks-band thermal emission of: TrES-2b (Croll et al., 2010a), TrES-3b including an H-band upper-limit (Croll et al., 2010b), and two eclipses of WASP-3b, including a limit on its temporal variability (Croll et al., in prep.).

In the near-infrared multiple band detections have only been performed on a handful of occasions; such multiple-band detections were performed in narrow wavelength regimes from space via spectroscopy with HST for HD 209458 and HD 189733 (Swain et al., 2009a,b), and arguably recently from the ground for HD 189733 using the Infrared Telescope Facility (Swain et al., 2010), as well as from the ground using the Very Large Telescope in the H & K-bands for the highly irradiated hot Jupiter WASP-19b (Anderson et al., 2010; Gibson et al., 2010). Multiple band detections in the near-infrared are therefore rare compared to the frequent multiple-band detections at longer wavelengths using the IRAC (Fazio et al., 2004), IRS (Houck et al., 2004), or MIPS (Rieke et al., 2004) instruments on the Spitzer Space Telescope. Multiwavelength thermal emission measurements with Spitzer have revealed a wealth of information, including that the most highly irradiated exoplanets seem to harbour hot stratospheres and temperature inversions (Knutson et al., 2008; Charbonneau et al., 2008; Machalek et al., 2008; Knutson et al., 2009b). One could imagine that obtaining multiwavelength constraints on a planet's thermal emission in the near-infrared could be equally informative. Furthermore, the near-

infrared is also an ideal place to directly constrain these planets' pressure-temperature profiles at depth, dayside bolometric luminosities, and the fraction of the incident stellar radiation that is transported from the tidally locked day to nightsides deep in these planets' atmospheres (Barman, 2008).

Here we continue our program using WIRCam on CFHT to detect thermal emission from some of the hottest of the hot Jupiters. Our target was the highly irradiated hot Jupiter WASP-12b. The discovery of the inflated, transiting exoplanet WASP-12b was of immediate interest to those attempting to measure the loss in flux during the secondary eclipses of hot Jupiters in the near-infrared - this was because WASP-12b circles a late F-type star with a period of only $\sim$26 hours (Hebb et al., 2009). It is thus exposed to extremely high stellar insolation, with an incident flux of $\sim 9 \times 10^9 \ ergs^{-1}cm^{-2}$. The planet is also one of the most inflated hot Jupiters, with a radius of $R_P \sim 1.8 R_J$ and a favourable planet-to-star radius ratio ($R_P/R_* \sim 0.12$; Hebb et al. 2009). It should be heated to an equilibrium temperature of over $\sim$2500 K assuming isotropic reradiation and a zero Bond albedo[1]. For these reasons it was predicted to display near-infrared thermal emission on the order of 0.1-0.3% of the stellar flux in the J, H & Ks near-infrared bands, assuming isotropic reradiation and a zero Bond albedo. Lopez-Morales et al. (2010) have already reported a detection of the secondary eclipse of WASP-12b in z'-band (0.9 μm), and more recently Campo et al. (2011) have presented detections of two eclipses in the four IRAC channels for WASP-12b. Campo et al. (2011), however, did not report the eclipse depths for WASP-12b, and for reasons discussed below the Lopez-Morales et al. (2010) detection has recently been called into question. Thus the atmospheric characteristics of WASP-12b remain largely unconstrained.

In addition to receiving extremely high stellar insolation, WASP-12b is intriguing because the combination of its close proximity to its star and its putative original eccentricity (e=0.049$\pm$0.015; Hebb et al. 2009) suggests that it could be precessing at a rate that is detectable with current instruments. Such a putative precession signal was recently claimed by Campo et al. (2011). Although the IRAC eclipses reported by Campo et al. (2011) suggest an $e\cos\omega$ constraint similar to that expected for a circular orbit ($e\cos\omega$=-0.0054$\pm$0.0030), Lopez-Morales et al. (2010) had earlier reported an eclipse detection that was considerably offset from a circular orbit ($|e\cos\omega|$=0.016$^{+0.011}_{-0.009}$). While at first glance the two measurements are inconsistent, if the planet precesses this is not the case. By combining their secondary eclipses with those of Lopez-Morales et al. (2010), together with the original radial velocity data for the system (Hebb et al., 2009), as well as a series of transit-time measurements from the original detection paper and ground-based amateurs (from the Exoplanet Transit Database; Poddany

---

[1]The Bond albedo is the fraction of the bolometric flux reflected from the planet compared to the incident bolometric radiation.

et al. 2010), Campo et al. (2011) show that a precessing orbital model best-fits the data with 2σ confidence. The authors caution that this detection is heavily dependent on the secondary eclipse offset reported by Lopez-Morales et al. (2010). Even more recently, radial velocity observations of WASP-12b have suggested that the eccentricity of WASP-12b is small (e=$0.017^{+0.015}_{-0.010}$; Husnoo et al. 2010) and likely zero, constraining the Campo et al. (2011) precession signal and calling into question the Lopez-Morales et al. (2010) eclipse detection. Nevertheless, the best-fit eccentricity of WASP-12b remains non-zero, and thus this planet could be precessing at a much slower rate than Campo et al. (2011) claim. The definitive nail in the coffin on the claim that WASP-12b is precessing at a detectable rate, will thus only result from further detections of this planet's secondary eclipse well separated in time from the original eclipse detections.

Also recently, preliminary evidence was presented that material from WASP-12b may be being tidally stripped from the planet and may possibly form a circumstellar disk in this system. Li et al. (2010) predicted that this system may have such a disk from material overfilling the Roche lobe of WASP-12b, because WASP-12b's observed radius in the optical (R_p~1.79 R_J; Hebb et al. 2009) is already close to its 2.36 R_J Roche lobe radius (as quoted in Fossati et al. 2010a). That WASP-12b may exhibit material overfilling it Roche lobe and a circumstellar disk from this material has recently received possible confirmation from HST Cosmic Origins Spectrograph (COS) observations of this system. From these observations Fossati et al. (2010a) find increased transit depths in the ultraviolet when compared to the optical, indicative of material surrounding WASP-12b overfilling its Roche lobe and blocking out a larger fraction of the stellar flux at these wavelengths. In addition they observe an early ingress of the transit of WASP-12b in their near ultraviolet data; Fossati et al. (2010a) interpret this early ingress as a putative sign of previously stripped material from WASP-12b forming a circumstellar disk. These putative signs of a disk are interesting to observers in the near-infrared, specifically the K-band, as Li et al. (2010) predicted that such a disk in this system may exhibit CO emission as bright as 10 mJy at 2.292 μm. WASP-12 does not, however, display a significant near-infrared excess (Fossati et al., 2010b).

Here we present detections of WASP-12b's thermal emission in the Ks (24σ), H (9σ) and J-bands (4σ). Our J-band detection is the first thermal emission measurement in this band. Our photometry favours a circular orbit for WASP-12b ($e\cos\omega$=$-0.0007^{+0.0013}_{-0.0013}$). By combining our secondary eclipse times with those of Lopez-Morales et al. (2010) and Campo et al. (2011), as well as the radial velocity data of Hebb et al. (2009) and Husnoo et al. (2010), and all the transit-time data for the system, we are able to show that not only is there no evidence to date that WASP-12b is precessing at a detectable rate, but also that the orbit of WASP-12b is likely circular. Our analysis also allows us to constrain the characteristics of the atmosphere of WASP-12b; our Ks-band eclipse depth argues in favour of inefficient redistribution of heat
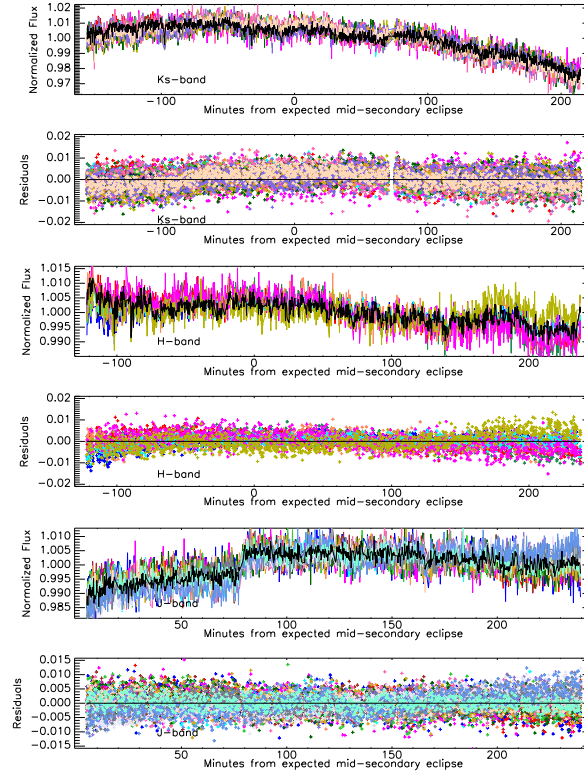
Figure 4.1 The normalized flux from our target star and reference stars for our Ks-band photometry (top two panels), our H-band photometry (middle two panels), and our J-band photometry (bottom panels). For each set of panels the top panel displays the flux from the target star (black) and the reference stars (various colours) that are used to calibrate the flux of WASP-12b in the various sets of photometry. The bottom panels in each set of panels displays the residuals from the normalized flux of the target star corrected by the normalized flux of the reference stars.

from the day to nightside, while our J and H-band observations seem to be probing deeper, higher pressure atmospheric layers that are slightly more homogenized. We also show that our Ks-band photometry may feature a longer than expected eclipse duration that could arguably be interpreted as evidence for material streaming from the planet or a circumstellar disk in this system.

4.3   Observations and Data Reduction

We obtained observations with WIRCam on CFHT of WASP-12 ($J\sim10.48$, $H\sim10.23$, $K\sim10.19$) on 2009 December 26, 27 and 28 in the J, H & Ks-bands respectively. Our J-band observations on Dec. 26 lasted for 3.9 hours and started in mid-eclipse and persisted for 2.2 hours after
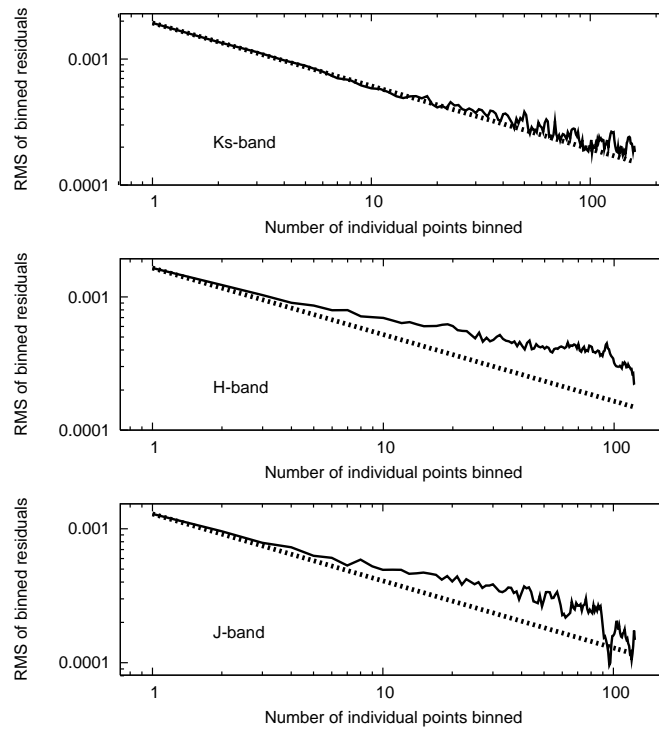
Figure 4.2 The root-mean-square of our out-of-eclipse photometry (solid line) following the corrections documented in §6.3 for our Ks-band photometry (top), our H-band photometry (middle), and our J-band photometry (bottom). The dashed line in each panel displays the one over the square-root of the bin-size expectation for Gaussian noise.

the end of eclipse. Our observations on Dec. 27 and 28 lasted for 6.0 hours in H-band and 6.2 hours in Ks-band, respectively, evenly bracketing the predicted secondary eclipse of WASP-12b. Numerous reference stars were also observed in the 21×21 arcmin field-of-view of WIRCam. The telescope was defocused for our various observations to approximately 1.5mm (J-band), 1.8mm (H-band), and 2.0mm (Ks-band), resulting in the flux of our target star being spread over a ring ∼19, ∼23, and ∼26 pixels in diameter (6, 7 and 8") on our array. For each observation, as the telescope temperature changed over the course of the night, we used the focus stage model and kept the defocus amount constant, thus achieved a stable PSF over the entire observation set. We used "Staring Mode" for our J and Ks-band observations where we do not dither for the duration of our observations; for the H-band eclipse the queue observations mistakenly used micro-dithering which featured small 0.5 pixel shifts between consecutive exposures. The exposure times for our J, H & Ks-band observations were 5-seconds. The effective duty cycle after accounting for readout and for saving exposures was 34%.

For both observations the data were reduced and aperture photometry was performed on our target star and our reference stars as discussed in Croll et al. (2010b) (with the details provided in Croll et al. 2010a). We used an aperture with a radius of 17 pixels for our Ks-band photometry, and 16.5 pixels for our H and J-band photometry. We used an annulus to define the sky with an inner radius of 22, and an outer radius of 34 pixels for all our photometry. We ensured that these choices of aperture were optimal by testing smaller and larger aperture sizes in increments of 0.5 pixels and ensuring these choices displayed the smallest root-mean-square (RMS) outside of occultation and the least time-correlated red-noise.

Following our aperture photometry we correct the flux of our target star with a number of nearby reference stars as discussed in Croll et al. (2010a). We used 22, 7, and 17 reference stars to correct our J, H and Ks-band eclipse photometry, respectively. The normalized flux of WASP-12 and the various reference stars that are used to correct the flux of our target star are displayed in Figure 4.1. For our Ks-band photometry we corrected our photometry for a small trend with the x, and y pixel position of the target star on the chip [2]. We did not notice such trends in our H and J-band photometry.

For our H-band photometry the airmass, X, was high at the start of the observations (X∼1.9), and fell to X∼1.2 by mid-eclipse. We noticed a downward trend in our H-band photometry following the correction with nearby reference stars that appeared to be correlated with airmass. We found that this effect was reduced, but not removed, for our H-band photometry by correcting the flux of WASP-12 with reference stars solely on the same WIRCam chip as WASP-12; this downward trend in flux of our target star compared to the reference stars is

---

[2]The correction is described in Croll et al. (2010a)

still apparent at the start of our H-band photometry. To reduce the impact of these systematic data we scale-up the errors of the first ∼25 minutes of data for our H-band photometry by a factor of 1.3.

The root-mean-square (RMS) of our photometry per minute following the above corrections improved from 10.0×10^{-3} to 0.86×10^{-3} in Ks-band, 3.8×10^{-3} to 0.90×10^{-3} in H-band and 1.93×10^{-3} to 0.69×10^{-3} in J-band. To evaluate the impact of systematics and the presence of red-noise in our photometry we bin our data and compare the out-of-eclipse photometric precision to the Gaussian noise expectation of one over the square-root of the bin-size (Figure 6.2). The Ks-band data bins down very close to the Gaussian noise limit, while the J-band data bins down marginally above this limit; the H-band data are worse, possibly due to the systematics introduced by the micro-dithering. To ensure that we do not underestimate the uncertainties in our model parameters we employ the Winn et al. (2008a) method to account for time-correlated red-noise in our photometry. We scale-up the uncertainties on our individual data-points by a factor β; β is equal to the factor that the binned out-of-eclipse RMS scales above the Gaussian noise expectation in the absence of red-noise. We use a binning time of ∼12 minutes. For our H-band photometry we exclude the first 15 minutes of data from this calculation, due to the obvious systematic that we believe to be correlated with airmass that does not appear to affect the rest of the photometry. For our photometry β is equal to 1.7, 1.3 and 1.1 for our J, H & Ks-band data, respectively. We note that our observations are still well above the predicted photon noise RMS limit of 2.7×10^{-4}, 2.2×10^{-4} and 3.1×10^{-4} per minute in the J, H & Ks-bands, respectively.

4.4   Analysis

For many of our other WIRCam data-sets we have observed residual background trends in the reduced data that seems to affect our target stars differently than our reference stars (Croll et al., 2010a,b, in prep.). For our Ks, H & J-band photometry these backgrounds, B_f, displayed a near-linear slope. We fit our Ks, H & J-band data-sets with linear backgrounds of the form:

$$B_f = 1 + c_1 + c_2 dt \qquad (4.1)$$

where dt is the interval from the beginning of the observations and c_1, c_2 and c_3 are fit parameters. We use Markov Chain Monte Carlo (MCMC) fitting to fit for our background as well as a secondary eclipse model calculated from the Mandel & Agol (2002) algorithm without limb darkening. We fit for the background, the depth of the secondary eclipse (ΔF) and the offset that the eclipse occurs later than the expected eclipse center (t_{offset}). Our Markov Chain Monte Carlo method is discussed in Croll (2006) and Croll et al. (2010a). We obtain our stellar

Table 4.1.   WASP-12b's best-fit secondary eclipse parameters

Parameter	Ks-band MCMC Solution	H-band MCMC Solution	J-band MCMC Solution	Joint MCMC Solution	Ks-band MCMC variable eclipse duration solution	Joint MCMC variable eclipse duration solution
reduced χ^2	$0.732^{+0.003}_{-0.001}$	$0.435^{+0.002}_{-0.001}$	$0.358^{+0.003}_{-0.002}$	$0.533^{+0.002}_{-0.001}$	$0.727^{+0.003}_{-0.001}$	$0.532^{+0.001}_{-0.001}$
ΔF_{Ks}	$0.310^{+0.012}_{-0.013}\%$	n/a	n/a	$0.309^{+0.013}_{-0.012}\%$	$0.311^{+0.013}_{-0.011}\%$	$0.313^{+0.011}_{-0.013}\%$
ΔF_H	n/a	$0.180^{+0.015}_{-0.018}\%$	n/a	$0.176^{+0.016}_{-0.021}\%$	n/a	$0.180^{+0.018}_{-0.020}\%$
ΔF_J	n/a	n/a	$0.126^{+0.030}_{-0.013}\%$	$0.131^{+0.027}_{-0.029}\%$	n/a	$0.129^{+0.027}_{-0.031}\%$
t_{offset} (min)[a]	$-1.3^{+1.5}_{-1.2}$	$2.0^{+2.1}_{-2.6}$	$-2.4^{+4.5}_{-4.5}$	$-0.7^{+1.3}_{-1.1}$	$-0.9^{+1.4}_{-1.4}$	$-0.6^{+0.9}_{-1.4}$
$t_{eclipseKs}$ (BJD-2450000)	$5194.9351^{+0.0010}_{-0.0008}$	n/a	n/a	$5194.9356^{+0.0009}_{-0.0007}$	$5194.9355^{+0.0010}_{-0.0010}$	$5194.9356^{+0.0007}_{-0.0010}$
$t_{eclipseH}$ (BJD-2450000)	n/a	$5193.8461^{+0.0014}_{-0.0018}$	n/a	$5193.8441^{+0.0009}_{-0.0007}$	n/a	$5193.8442^{+0.0007}_{-0.0010}$
$t_{eclipseJ}$ (BJD-2450000)	n/a	n/a	$5192.7515^{+0.0031}_{-0.0031}$	$5192.7527^{+0.0009}_{-0.0007}$	n/a	$5192.7528^{+0.0007}_{-0.0010}$
c_{1Ks}	$0.00116^{+0.00014}_{-0.00014}$	n/a	n/a	$0.00116^{+0.00012}_{-0.00015}$	$0.00126^{+0.00016}_{-0.00014}$	$0.00122^{+0.00017}_{-0.00013}$
c_{2Ks} (d^{-1})	$0.001^{+0.001}_{-0.001}$	n/a	n/a	$0.001^{+0.001}_{-0.001}$	$0.001^{+0.001}_{-0.001}$	$0.001^{+0.001}_{-0.001}$
c_{1H}	n/a	$0.00109^{+0.00022}_{-0.00021}$	n/a	$0.00104^{+0.00024}_{-0.00024}$	n/a	$0.00115^{+0.00026}_{-0.00024}$
c_{2H} (d^{-1})	n/a	$-0.003^{+0.001}_{-0.001}$	n/a	$-0.003^{+0.001}_{-0.001}$	n/a	$-0.003^{+0.001}_{-0.001}$
c_{1J}	n/a	n/a	$0.00157^{+0.00027}_{-0.00035}$	$0.00163^{+0.00030}_{-0.00031}$	n/a	$0.00163^{+0.00031}_{-0.00031}$
c_{2J} (d^{-1})	n/a	n/a	$-0.014^{+0.003}_{-0.003}$	$-0.015^{+0.003}_{-0.003}$	n/a	$-0.015^{+0.003}_{-0.003}$
ϕ [a]	$0.4994^{+0.0009}_{-0.0008}$	$0.5015^{+0.0013}_{-0.0017}$	$0.4987^{+0.0028}_{-0.0028}$	$0.4998^{+0.0008}_{-0.0007}$	$0.4997^{+0.0009}_{-0.0009}$	$0.4999^{+0.0006}_{-0.0009}$
$\Phi_{II/I}$	n/a	n/a	n/a	n/a	$1.109^{+0.046}_{-0.039}$	$1.080^{+0.034}_{-0.034}$
Φ_{II} (hours)	2.93	2.93	2.93	2.93	$3.25^{+0.14}_{-0.11}$	$3.16^{+0.10}_{-0.10}$
T_{BKs} (K)	2988^{+45}_{-46}	n/a	n/a	2985^{+49}_{-49}	2993^{+50}_{-51}	3000^{+40}_{-40}
T_{BH} (K)	n/a	2765^{+70}_{-72}	n/a	2748^{+71}_{-74}	n/a	2763^{+80}_{-84}
T_{BJ} (K)	n/a	n/a	2833^{+152}_{-173}	2860^{+138}_{-155}	n/a	2849^{+138}_{-155}
$e\cos(\omega)$ [a]	$-0.0013^{+0.0015}_{-0.0015}$	$0.0020^{+0.0021}_{-0.0021}$	$-0.0024^{+0.0044}_{-0.0044}$	$-0.0007^{+0.0013}_{-0.0013}$	$-0.0009^{+0.0014}_{-0.0014}$	$-0.0006^{+0.0009}_{-0.0009}$
$e\sin(\omega)$	n/a	n/a	n/a	n/a	$0.059^{+0.082}_{-0.034}$	$0.044^{+0.062}_{-0.026}$
f_{Ks}	$0.482^{+0.030}_{-0.029}$	n/a	n/a	$0.480^{+0.032}_{-0.031}$	$0.485^{+0.034}_{-0.033}$	$0.490^{+0.027}_{-0.026}$
f_H	n/a	$0.353^{+0.037}_{-0.036}$	n/a	$0.345^{+0.037}_{-0.036}$	n/a	$0.353^{+0.043}_{-0.041}$
f_J	n/a	n/a	$0.389^{+0.091}_{-0.087}$	$0.405^{+0.085}_{-0.081}$	n/a	$0.399^{+0.083}_{-0.080}$

[a]We account for the increased light travel-time in the system (Loeb, 2005), and use the best-fit period for the non-precessing case reported by Campo et al. (2011).
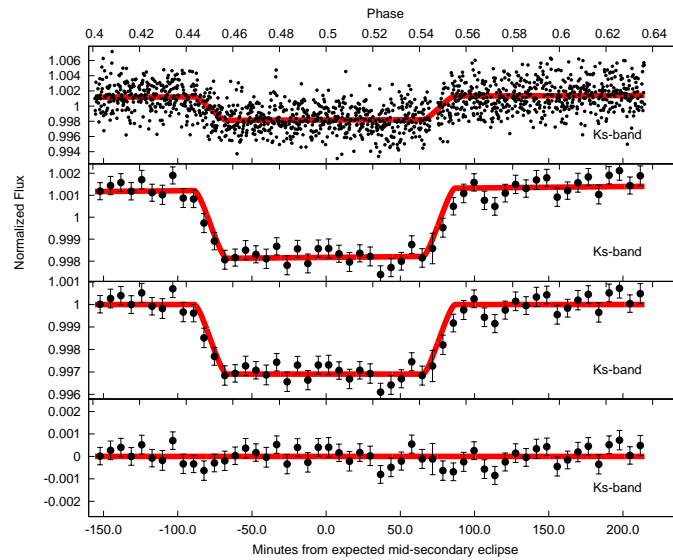
Figure 4.3 CFHT/WIRCam photometry of the secondary eclipse of WASP-12b observed in the Ks-band on 28 December 2009. The top panel shows the unbinned light curve with the best-fit secondary eclipse and background from our MCMC analysis of the Ks-band data with the fixed eclipse duration (red line). The second panel shows the light curve with the data binned every ∼7.0 minutes and again our best-fit eclipse and background. The third panel shows the binned data after the subtraction of the best-fit background, B_f, along with the best-fit eclipse model. The bottom panel shows the binned residuals from the best-fit model.
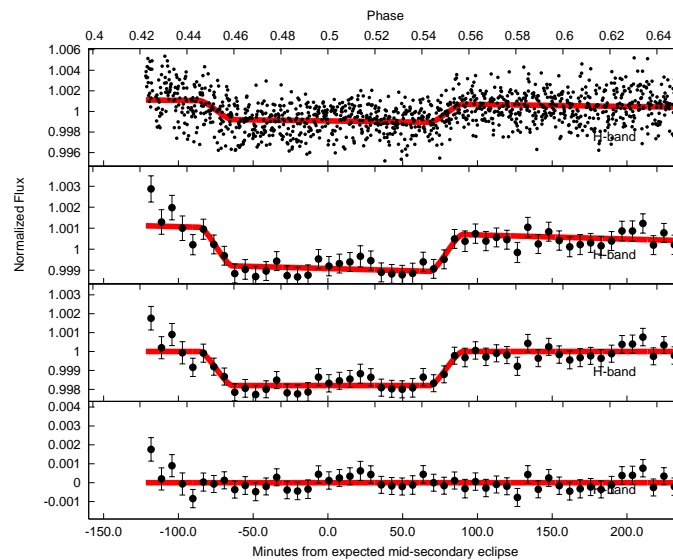
Figure 4.4 The same as figure 4.3 except that the data are our H-band photometry obtained on 27 December 2009.
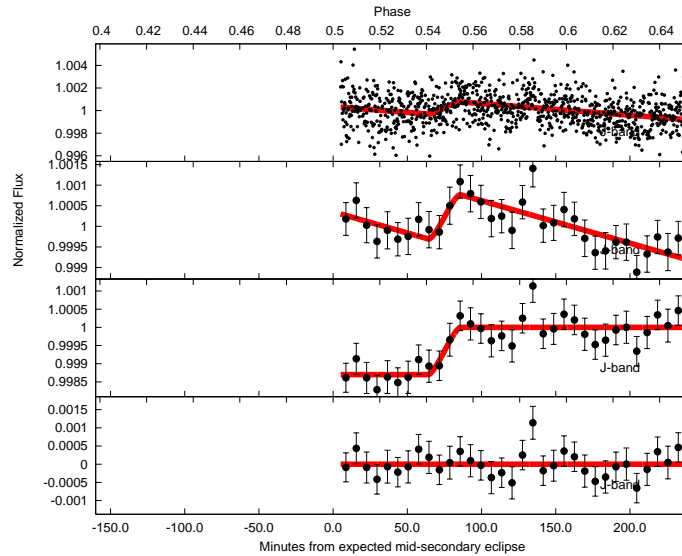
Figure 4.5 The same as figure 4.3 except that the data are our J-band photometry obtained on 26 December 2009. Note that the photometry is a partial eclipse only, and starts in eclipse and extends well out of eclipse.
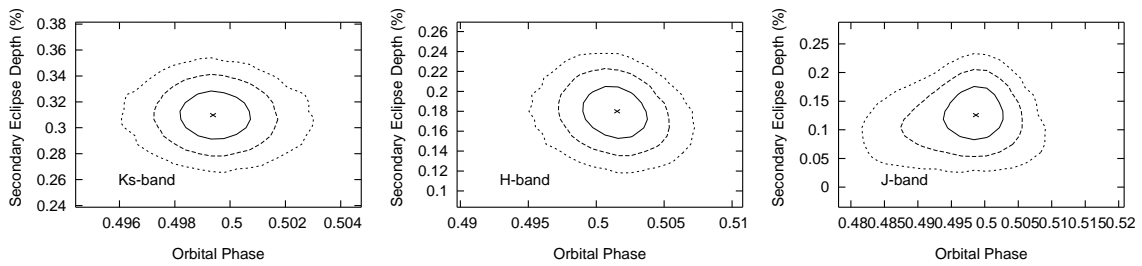
Figure 4.6 The 68.3% (1σ; solid-line), 95.5% (2σ; dashed-line), and 99.7% (3σ; dotted-line) credible regions from our individual MCMC analyses with a fixed eclipse duration of our Ks-band photometry (left), H-band photometry (middle), and J-band photometry (right). The "x" in the middle of the plots marks the best-fit point from our MCMC analyses.

and planetary parameters for WASP-12 from Hebb et al. (2009), while the planetary period and ephemeris are obtained from Campo et al. (2011) from their non-precessing best-fit.

The best-fit secondary eclipses from our individual MCMC analyses with a fixed eclipse duration are presented in Figures 4.3, 4.4 and 4.5 and the best-fit eclipse parameters are presented in Table 6.1 along with associated parameters, such as the best-fit phase, ϕ, and the barycentric Julian Date of the eclipse center in the terrestrial time format[3], $t_{eclipse}$. The phase dependence of these fits are presented in Figure 6.4. We also perform a joint analysis of the three secondary eclipses with a common offset from the eclipse center (t_{offset}); the fit parameters are thus $\Delta F_K s$, ΔF_H, ΔF_J, t_{offset}, and c_1, and c_2 in each band. The resulting best-fit parameters of this joint fit are listed in Table 6.1.

We also repeat our fit for our Ks-band photometry, our highest signal-to-noise photometry, and for the joint analysis while fitting for an additional parameter - the duration of the secondary eclipse, Φ_{II}. We parameterize this by the duration of the eclipse divided by the duration of the transit, $\Phi_{II/I}$, using the duration of the transit ($\Phi_I \sim 2.93\ h$) reported by Hebb et al. (2009). The results from this fit are presented in Table 6.1. We do not fit our J-band or H-band data individually with this additional parameter, Φ_{II}, as the J-band data are of a partial eclipse and thus the duration of the secondary eclipse is degenerate with an offset of the eclipse center, and the H-band data suffers from additional time-correlated systematics that could lead to erroneous conclusions.

4.5   Discussion

We strongly detect all three secondary eclipses in the three near-infrared bands that we observed in. The individual analyses of our three eclipses confirm that all three secondary eclipses are fit with a consistent phase (Table 6.1); thus the best-fit parameters from our joint analysis are similar to the parameters returned by the analyses of the individual eclipses. We therefore quote the results of the joint analysis below. The best-fit eclipse depths from our joint analysis is $0.309^{+0.013}_{-0.012}\%$ in Ks-band, $0.176^{+0.016}_{-0.021}\%$ in H-band and $0.131^{+0.027}_{-0.029}\%$ in J-band.

4.5.1   Eccentricity and Precession of WASP-12b

The best-fit phase of the joint analysis is $\phi = 0.4998^{+0.0008}_{-0.0007}$. The resulting limit on the eccentricity, e, and argument of periastron, ω, is $e\cos\omega = -0.0007^{+0.0013}_{-0.0013}$, a result that is consistent with a circular orbit and the Campo et al. (2011) results. This value is inconsistent, however, with the Lopez-Morales et al. (2010) $e\cos\omega$ result. The discrepancy between the Lopez-Morales

---

[3]As calculated using the routines of Eastman et al. (2010).

Table 4.2.   WASP-12b's orbital parameters

Parameter	Precessing Case	Non-Precessing Case	Non-Precessing Case without the Lopez-Morales et al. (2010) eclipse
P (days)	$1.0914239^{+0.0000004}_{-0.0000004}$	$1.0914239^{+0.0000003}_{-0.0000003}$	$1.0914239^{+0.0000002}_{-0.0000004}$
e	$0.00095^{+0.01428}_{-0.00063}$	$0.00095^{+0.02435}_{-0.00063}$	$0.00087^{+0.02494}_{-0.00058}$
T_o (BJD-2450000)	$4508.9769^{+0.0001}_{-0.0002}$	$4508.9769^{+0.0001}_{-0.0001}$	$4508.9769^{+0.0002}_{-0.0001}$
ω_o (^{o})	$-90.9^{+183.6}_{-4.5}$ [a]	$-89.9^{+1.8}_{-2.7}$ [a]	$-90.0^{+180.9}_{-2.7}$ [a]
$\dot{\omega}$ (^{o} d^{-1})	$0.003^{+0.001}_{-0.001}$	0.0 [b]	0.0 [b]
$e\cos\omega_o$	$-0.0001^{+0.0003}_{-0.0007}$	$-0.0000^{+0.0004}_{-0.0005}$	$-0.0001^{+0.0005}_{-0.0005}$
$e\sin\omega_o$	$-0.000^{+0.011}_{-0.018}$	$-0.016^{+0.017}_{-0.017}$	$-0.015^{+0.017}_{-0.019}$
χ^2	85.5	93.2	91.4
BIC	106.5	110.1	108.2

[a]These distributions are bimodal with strong peaks at $\omega \sim 90^o$ and -90° (where $\cos\omega \sim 0$.)

[b]By definition.)
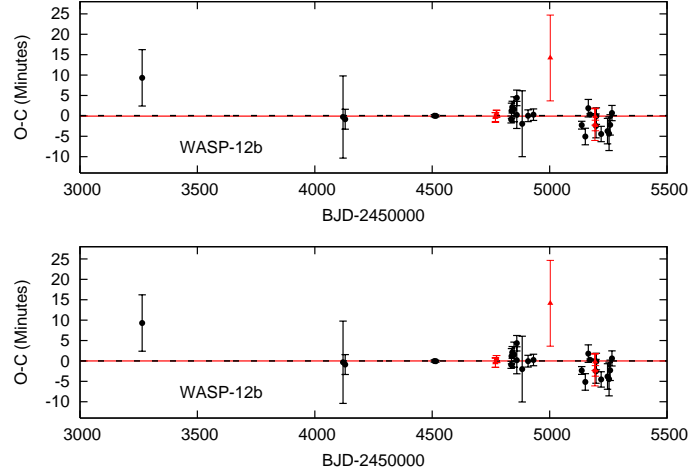
Figure 4.7 Transit (black points) and eclipse (red points) times for WASP-12b compared to the best-fit orbital models for the precessing case (top), and the non-precessing case (bottom). The best-fit models for the transit times (dotted black line) and the eclipse times (solid red line) are also shown. Both diagrams show the observed-minus-calculated (O-C) times from a linear ephemeris calculated using T_o and P; the secondary eclipse O-C times are compared to a calculated eclipse centre of $T_o + \frac{P}{2}$. The eclipse points in the two panels are from left-to-right, the Campo et al. (2011) Spitzer/IRAC eclipses (BJD-2450000~4750), the Lopez-Morales et al. (2010) eclipse (BJD-2450000~5000), while the last three red-points are the eclipse times reported here (BJD-2450000~5200).

et al. (2010) result and that of Campo et al. (2011) and our own could be due to WASP-12b precessing - we explore this possibility below.

Campo et al. (2011) performed an analysis of the reported transit times and secondary eclipse times and presented tentative evidence that WASP-12b may be precessing at an observable rate, $\dot{\omega} = 0.02 \pm 0.01^o$ d^{-1}, with a period as short as 40 years. The primary evidence for the precession was the ground-based secondary eclipse detection of Lopez-Morales et al. (2010), which occurred late by approximately ~15 minutes (at a phase of $\phi = 0.5100^{+0.0072}_{-0.0061}$ using the Hebb et al. 2009 ephemeris and period).

We repeat the Campo et al. (2011) precession analysis adding in our three secondary eclipse detections. We summarize the Campo et al. (2011) precession model that we employ here. The mid-transit time of the Nth transit, T_N, in our precessing model is predicted to occur at:

$$T_N = T_o + P_s N - \frac{eP_a}{\pi}(cos\omega_N - cos\omega_o). \tag{4.2}$$

T_o and ω_o are the transit time and argument of periastron at the reference epoch, ω_N is the argument of periastron of the Nth transit, P_s is the sidereal period, P_a is the period between successive periastron passages, and e has already been defined as the eccentricity. P_a is not an

independent variable, but is related to the sidereal period, P_s, and the constant precession rate, $\dot{\omega}$: $P_a = \frac{P_s}{1 - P_s \frac{\dot{\omega}}{2\pi}}$. The argument of periastron of the Nth transit is simply $\omega_N = \dot{\omega}(T_N - T_o) + \omega_o$. Equation 4.2 is solved iteratively for T_N after it is expanded to the fifth order in e (as shown in equation (22) of Ragozzine & Wolf 2009). We fit the radial velocity data from Hebb et al. (2009) and Husnoo et al. (2010)[4], and the transits listed in Table 2 of Campo et al. (2011) as well as four additional, recent transits[5] from the Exoplanet Transit database (Poddany et al., 2010) and our own secondary eclipse data along with those of Lopez-Morales et al. (2010), and Campo et al. (2011). We exclude the in-transit radial velocity data as we do not model for the Rossiter-McLaughlin effect (Gaudi & Winn, 2007). We follow Campo et al. (2011), and quote the Lopez-Morales et al. (2010) eclipse point that results from the combined photometry from 1.5 eclipses, at a single epoch halfway between their observations (HJD~2455002.8560 $\pm$ 0.0073). T_N of course gives the transit time to compare to the data, we use e, ω_N, T_N and P_a to calculate the eclipse times, and $\omega(t)$ to calculate the radial velocity values. We use the MCMC techniques explained above to calculate the best-fit precessing model, and non-precessing models, except that we fit for $ecos\omega$ and $esin\omega$, instead of e and ω, as ω is poorly constrained as the eccentricity approaches zero.

We plot our precessing and non-precessing best-fit models in Figure 4.7 and present the MCMC results in Table 4.2. The best-fit models with and without precession are similar. The best-fit precessing model features a very small rate of precession ($\dot{\omega} = 0.003^{+0.001o}_{-0.001}$ d^{-1}), that barely provides a superior fit once the extra degrees of freedom are taken into account (a Bayesian Information Criterion[6] of BIC=106.5 for the precessing case, compared to BIC=110.1 for the non-precessing case). Thus there is not convincing evidence at this date that WASP-12b is precessing.

Given that the timing offset of the Lopez-Morales et al. (2010) eclipse detection may be suspect, we also refit the non-precessing case with this eclipse excluded, and present the MCMC results in Table 4.2. The distribution of eccentricity values from our MCMC chain without the Lopez-Morales et al. (2010) eclipse is non-Gaussian (the bottom left panel of Figure 4.8) and favours a near-zero eccentricity with a tail to higher eccentricity values; this limit

---

[4]Husnoo et al. (2010) argue that there may be correlated red noise in the Hebb et al. (2009) radial-velocity data, possibly due to a systematic offset in the RV zero-point from night to night. As a result we scale-up the errors for the Hebb et al. (2009) data by a factor of 8 and those of Husnoo et al. (2010) by a factor of 2 to account for possible offsets between these two data-sets. We refer the reader to Husnoo et al. (2010) for further discussion.

[5]The additional transits have mid-transit times (HJD) of 2455246.77604$\pm$0.00217 (A. Gibson, TRESCA), 2455253.32414$\pm$0.00287 (F. Lomoz, TRESCA), 2455257.69131 (G. Haagen, TRESCA), and 2455265.33327$\pm$0.00129 (H. Kucakova, TRESCA).

[6]For the Bayesian Information Criterion (Liddle, 2007) lower-values indicate superior fits corrected for the number of free parameters: $BIC=\chi^2 + k\ln N$, where k is the number of free parameters and N is the number of data points.
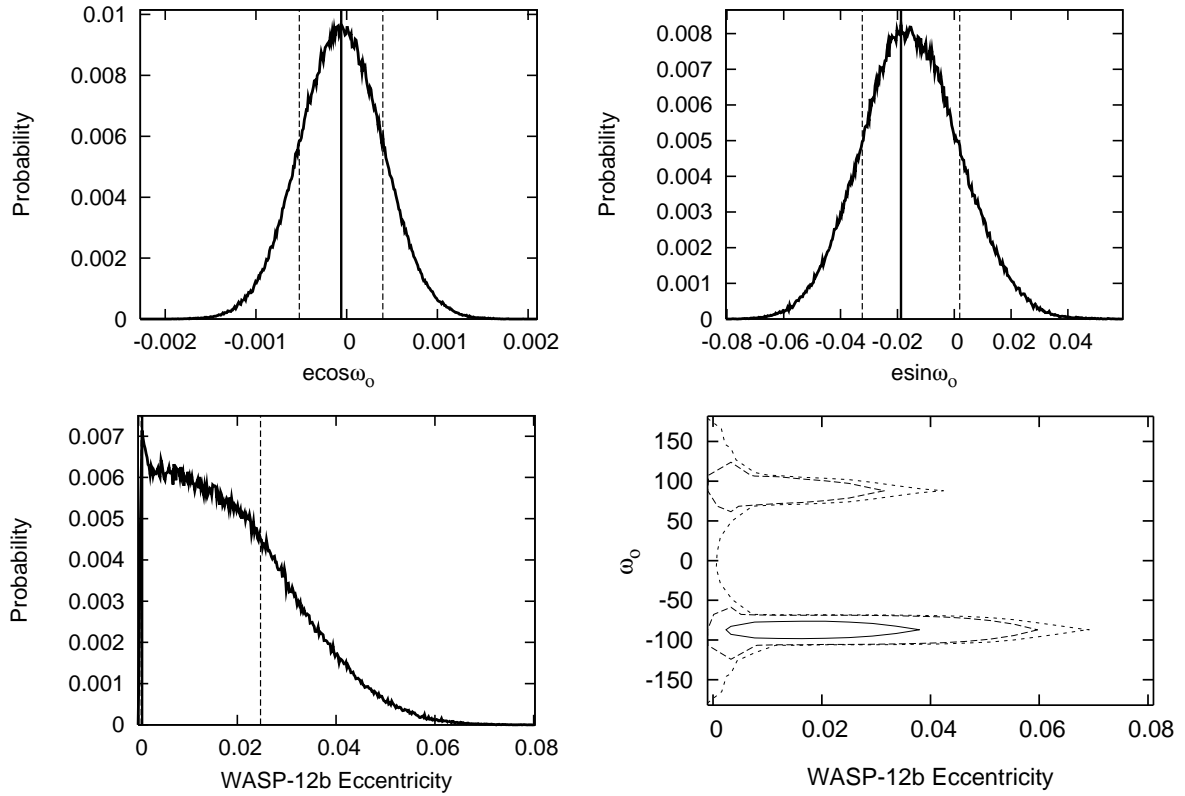
Figure 4.8 Top-left, top-right and bottom-left panels: Marginalized likelihood for WASP-12b's $e\cos\omega$, $e\sin\omega$ and its eccentricity from the non-precessing MCMC chain with the Lopez-Morales et al. (2010) point excluded. The best-fit value for each panel is given with the solid vertical line (for the bottom-left panel this value is nearly indistinguishable from zero), while the 68% credible region is indicated by the dotted vertical line. Bottom-right panel: Contour parameter showing the eccentricity, e, and the argument or periastron, ω, of WASP-12b again from the same MCMC chain. The 68.3% (1σ; solid-line), 95.5% (2σ; dashed-line), and 99.7% (3σ; dotted-line) credible regions are indicated.
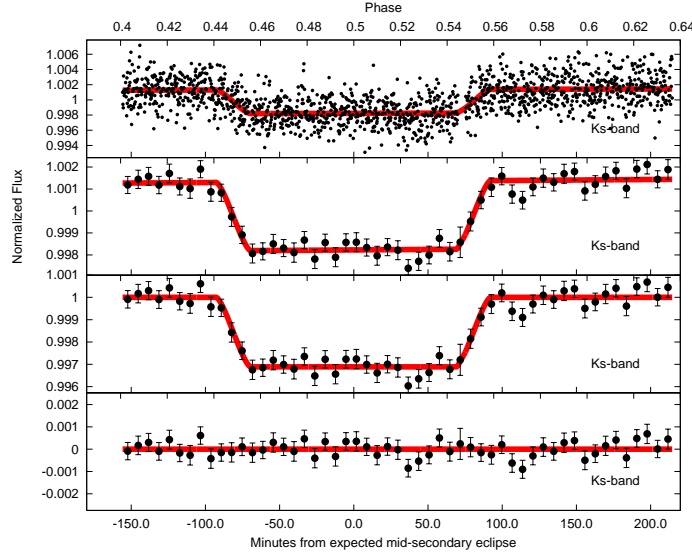
Figure 4.9 The same as figure 4.3 except that the best-fit model is our variable eclipse duration model for our Ks-band photometry.

is $e=0.00087^{+0.02494}_{-0.00058}$. This is due to the fact that although the $e\cos\omega_o$ values for WASP-12b are well-constrained from the radial-velocity data and the combination of the timing of the eclipses and transits (the top-left panel of Figure 4.8), the $e\sin\omega_o$ values are not well-constrained and thus higher eccentricity values are allowed (the top-right panel of Figure 4.8) for an argument of periastron where $\cos\omega_o\sim0$ at $\omega_o\sim90^o$ and -90° (as can be seen in the contour plot in the bottom-right panel of Figure 4.8). Although we are not able to rule out higher eccentricity values for WASP-12b with high confidence, the orbit of WASP-12b is likely circular; thus WASP-12b is no longer an outlier from the expectation of the timescale of tidal circularization for close-in giant exoplanets. The above analysis would be improved by including an a priori constraint on $e\sin\omega_o$ using the eclipse duration values from our own eclipses and the Campo et al. (2011) Spitzer/IRAC eclipses. Unfortunately, although Campo et al. (2011) indicate that their best-fit eclipse durations are similar to that of the transits and should thus place a tight constrain on $e\sin\omega_o$ near zero, Campo et al. (2011) do not formally fit for the duration of the eclipse and do not include the associated uncertainties. We discuss the implications of fitting our own eclipse durations below.

4.5.2   A longer duration secondary eclipse; possible signs of material stripped from the planet?

We also fit our Ks-band photometry and our joint J, H & Ks-band photometry with an eclipse model with the eclipse duration as a free parameter. Our best-fit Ks-band variable eclipse

duration fit is presented in Figure 4.9. Our variable eclipse duration fit does argue for a marginally wider secondary eclipse than transit: $\Phi_{II/I} = 1.109^{+0.046}_{-0.039}$, although this result is only significant at the 2.8σ-level. The associated eclipse duration is $\Phi_{II} = 3.25^{+0.14}_{-0.11}$ hours, longer than the $\sim$2.93 hour optical transit found by Hebb et al. (2009), and longer than the similar duration IRAC eclipses found by Campo et al. (2011). That the data suggests a wider secondary eclipse than our best-fit model can be seen in the ingress and egress of our Ks-band photometry (Figure 4.3).

Our joint analysis of our J, H & Ks-band data also argues for a marginally wider secondary eclipse than transit: $\Phi_{II/I} = 1.080^{+0.034}_{-0.034}$, or that the duration of the eclipse is $\Phi_{II} = 3.16^{+0.10}_{-0.10}$ hours. As our J-band data is a partial eclipse, it has no ability to constrain the eclipse duration on its own. Similarly, as our H-band data suffers from significant systematics prior to and during ingress, its ability to constrain the eclipse duration is compromised; in fact, the systematics at the beginning of the H-band photometry that manifest themselves as a sharp decrease in flux, can be well-fit by a significantly wider, and deeper secondary eclipse that is unlikely to be physical. These facts, combined with a visual inspection of Figures 4.3-4.5, suggests that the wider secondary eclipse for our joint analysis, is in-fact dominated by our Ks-band photometry and the longer duration eclipse may not be credible for the joint analysis.

Our Ks-band photometry is best-fit with a wider secondary eclipse than expected: $\Phi_{II/I}=1.109^{+0.046}_{-0.039}$. The first possibility to explain this wider than expected eclipse is systematic time-correlated, red-noise in our photometry, which would not be unexpected as the eclipse is only wider than expected at less than the 3σ level. Another possibility for this wider eclipse is that the planet has a small eccentricity ($e\sin\omega=0.059^{+0.082}_{-0.034}$). We have already presented strong evidence that the eccentricity of WASP-12b is quite likely near zero in §4.5.1 and the Campo et al. (2011) Spitzer/IRAC eclipse photometry does not feature a longer duration secondary eclipse. Also, although the $e\sin\omega$ of the planet is less well constrained in §4.5.1, an $e\sin\omega$ value necessary to explain our longer duration eclipse can be ruled out at several sigma and thus we find this possibility uncompelling.

Another possibility – perhaps the most intriguing possibility – is that if this apparently wider secondary eclipse is not due to systematic effects or due to a small $e\sin\omega$ for WASP-12b, then it could be due to radiation from gas that is escaping from the planet and possibly forming a circumstellar disk. The latter was predicted by Li et al. (2010), while the former was arguably recently confirmed by Fossati et al. (2010a) through observations that WASP-12b displayed increased transit depths in the UV with COS/HST. An eclipse of this duration could argue for material surrounding the planet with a projected radius that is approximately 1.9 times the optical radius of the planet, or at a radius of 3.3 $R_{Jupiter}$, and would thus argue for material emitting radiation that is exceeding the Roche lobe, and streaming from the planet.

This emission could be due to CO ~2.292 bandhead emission, as predicted by Li et al. (2010), although the material around the planet should be cooler than the ~4000-5000 K temperatures they predicted for the cirumstellar disk and will thus result in reduced emission. In the "accretion stream" hypothesis, advocated by (Lai et al., 2010), the material streaming from the planet towards the star may be highly localized in a line passing through the inner Lagrangian point. The extra emission from this stream would be obscured by the star earlier than the planet during eclipse ingress and later than the planet during eclipse egress. Such a scenario is arguably favoured over simply a sphere of evaporating material 3.3 $R_{Jupiter}$ in radius, as in the accretion stream scenario the emission will arise from a smaller surface area; otherwise the Ks-band brightness temperature of the planet would have to be anomalously low, given that the $\Delta F_{Ks}{=}0.309^{+0.013}_{-0.012}\%$ that we observe would have to be a combination of the planet and the enveloping material that would have a much larger surface area of emitting material than the planet itself.

Alternatively, this wider eclipse could be interpreted as the planet passing behind a circumstellar disk that is optically thick at these wavelengths and extends marginally from the star (at least ~1.11 times the stellar radius), and therefore obscures the planet earlier and later than expected. If the disk is optically thick it will have to be due to gas opacity, as the temperature of the disk will be well above the dust sublimation temperature, and the temperature and density of the disk will have to be high enough for the material to be largely photoionized to avoid the "opacity gap" (Thompson et al., 2005). The disk would also have to be optically thick at around 2 μm, but not at the longer wavelengths probed by Spitzer/IRAC (3.6 to 8.0 μm) as the durations of the eclipses are not discrepant from the expected duration in the Campo et al. (2011) photometry. The "accretion stream" hypothesis is arguably less contrived, but the observed eclipse duration could also result from a combination of both scenarios.

An obvious way to differentiate between these two scenarios would be observations of WASP-12 during transit in the Ks-band band. If WASP-12 is surrounded by a circumstellar disk that is emitting in Ks-band then the transit duration will increase. If there is material surrounding WASP-12b, then its transit will be of the expected duration if the material is optically thin, and the transit will display an increased depth if the material is optically thick. We plan to perform such follow-up observations of the transit and eclipse of WASP-12b in the Ks and H-bands to differentiate between these various scenarios, and to confirm the near-zero eccentricity of WASP-12b. Until such follow-up observations take place we emphasize that our Ks-band photometry is best-fit with a wider eclipse at less than the 3σ level.
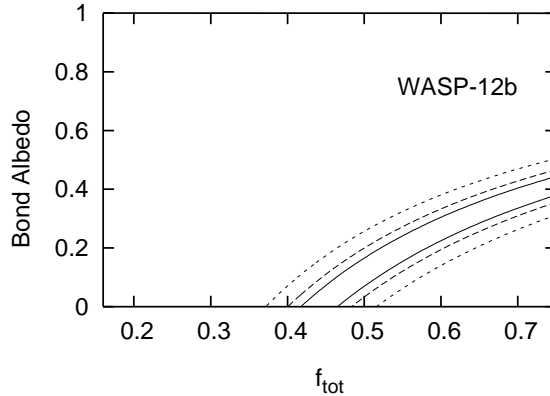
Figure 4.10 1σ (solid-lines), 2σ (dashed-lines), and 3σ (dotted-lines) constraints on the Bond albedo and reradiation factor, f_{tot} from our Ks, H & J-band secondary eclipse observations of WASP-12b.

4.5.3   The properties of WASP-12b's atmosphere

Our measurements of the thermal emission of WASP-12b allow us to constrain the characteristics of its atmosphere, including: its Bond albedo, the level of redistribution of heat from the day to the nightside at various depths, and the planet's dayside bolometric luminosity. We parameterize the level of redistribution by the reradiation factor, f, following the Lopez-Morales & Seager (2007) definition (i.e. $f=\frac{1}{4}$ denotes isotropic reradiation, while $f=\frac{1}{2}$ denotes redistribution and reradiation from the dayside only). Our eclipse depths are consistent with a range of Bond albedos, A_B, and overall day to nightside redistribution of heat, f_{tot} (Figure 6.6). If we assume a Bond albedo near zero, consistent with observations of other hot Jupiters (Charbonneau et al., 1999; Rowe et al., 2008) and with model predictions (Burrows et al., 2008b), the best-fit reradiation factor, f_{tot}, that results from our three near-infrared eclipse measurements is $f_{tot} = 0.441^{+0.024}_{-0.023}$. This suggests that the dayside of WASP-12b reradiates most of the incident stellar flux without redistributing it to the nightside.

As the atmospheres of hot Jupiters may be highly vertically stratified, different atmospheric layers may redistribute heat much more or much less efficiently than other layers. The best-fit brightness temperatures and reradiation factors of the individual atmospheric layers probed by our various wavelengths of observations are: $T_{BKs}=2988^{+45}_{-46}K$ and $f_{Ks}=0.482^{+0.030}_{-0.029}$ for our Ks-band observations, $T_{BH} =2765^{+70}_{-72}K$ and $f_H=0.353^{+0.037}_{-0.036}$ for our H-band observations, $T_{BJ} =2833^{+152}_{-173}K$ and $f_J=0.389^{+0.091}_{-0.087}$ for our J-band observations. Our three different bands should be probing high pressure regions, deep into the atmosphere of WASP-12b. Specifically if the near-infrared opacity is dominated by water vapour opacity the J, H & K-bands should be windows in water opacity (Fortney et al., 2008), and the Ks, H & J-bands should be seeing progressively deeper into WASP-12b's atmosphere. Within the errors the brightness temperatures
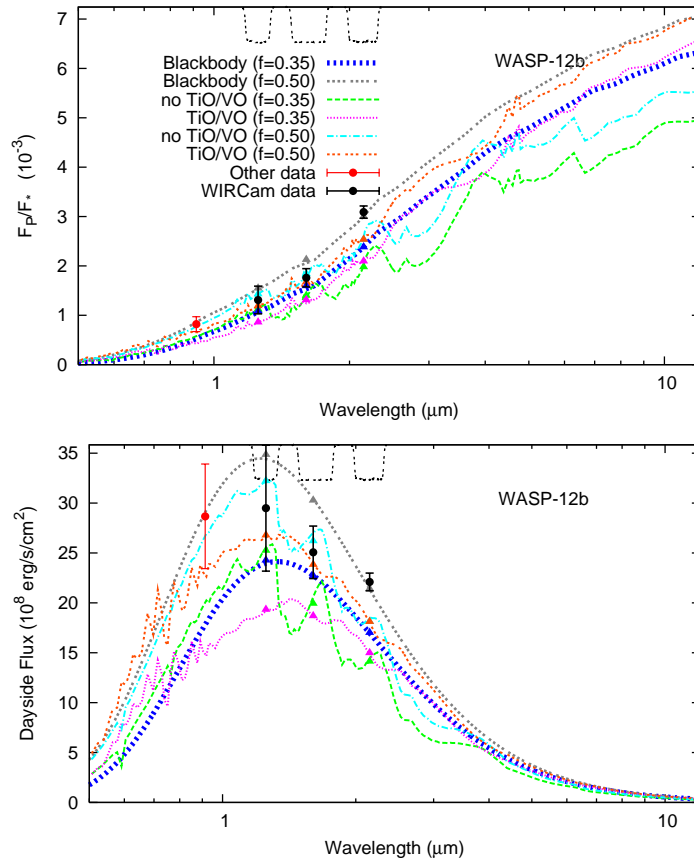
Figure 4.11 Dayside planet-to-star flux ratios (top) and dayside flux at the planet's surface (bottom). The Ks-band ($\sim$2.15 μm), H-band ($\sim$1.60 μm) and J-band ($\sim$1.25 μm) points are our own, while the z'-band point ($\sim$0.9 μm) is from Lopez-Morales et al. (2010). Blackbody curves for modest redistribution (f=0.35; $T_{eq}\sim$2735 K; blue dashed line), and dayside only emission (f=$\frac{1}{2}$; $T_{eq}\sim$2990 K; grey dotted line) are also plotted. We also plot one-dimensional, radiative transfer spectral models (Fortney et al., 2006, 2008) for various reradiation factors and with and without TiO/VO. We plot models with modest redistribution (f=0.35) with and without TiO/VO (magenta-dotted and green-dashed lines, respectively), and for dayside only emission (f=$\frac{1}{2}$) with and without TiO/VO (orange dotted and cyan dot-dashed lines, respectively). The models with TiO/VO display temperature inversions. The models on the top panel are divided by a stellar atmosphere model (Hauschildt et al., 1999) of WASP-12 using the parameters from (Hebb et al., 2009). (M_*=1.35 $M_\odot$, R_*=1.57 $R_\odot$, T_{eff}=6300 K, and log g=4.38). We plot the WIRCam Ks, H and J-band transmission curves inverted at arbitrary scale at the top of both panels (dotted black lines). We integrate our models over the WIRCam bandpasses and display the result in the appropriately coloured triangles.

displayed in our three near-infrared bands are similar. However, the J and H-band brightness temperatures are marginally lower, and taken at face value compared to the Ks-band brightness temperature they suggest a modest temperature inversion at very high pressures of ~100 to 500 mbar, deep in the atmosphere of WASP-12b. One explanation for why WASP-12b might display decreased flux at these shorter wavelengths as compared to the Ks-band, is that the atmospheric depths and pressures probed by these shorter wavelength observations may be more homogenized than higher altitude layers. The efficiency of redistribution of the incident stellar flux from the dayside to the nightside should be proportional to the ratio of the reradiative (τ_{rad}) to advective timescales (τ_{adv}). It is thought that the reradiative timescale should increase with pressure and depth[7]. The advective timescale [8] is also thought to increase in pressure, although it is generally thought that advection should win out over reradiation as one descends through the atmosphere of a typical hot Jupiter (Seager et al., 2005b; Fortney et al., 2008). Thus, one might expect more efficient redistribution of heat at the layers probed by our shorter wavelength observations compared to the layers probed by our Ks-band observations. Other explanations for the relatively higher Ks-band emission than the H and J-band emission are certainly possible, including: extra flux from a circumstellar disk or material streaming from the planet in the Ks-band, an atmospheric emission feature at Ks-band, or absorption features over the H and J-bands. The eclipse depths from the Campo et al. (2011) Spitzer/IRAC measurements will not shed much additional light on this matter, as, if water opacity dominates, the Spitzer/IRAC bands to do not probe as deeply as the JHK near-infrared bands.

We compare the depths of our near-infrared eclipses to a series of planetary atmosphere models in Figure 6.7. This comparison is made quantitatively as well as qualitatively by integrating the models over the WIRCam J, H & Ks band-passes and calculating the χ^2 of the thermal emission data compared to the models. We include the Lopez-Morales et al. (2010) eclipse depth in Figure 6.7, but do not include it in our χ^2 calculation due to the aforementioned uncertainty with the timing and depth of this eclipse. The Spitzer/IRAC eclipse depths (Campo et al., 2011) are also not included, as of the time of writing only the central eclipse times have been reported. We first plot two blackbody models, the first one displaying modestly efficient heat redistribution (f=0.35; blue dotted line; T_{eq}~2735 K), while the latter features emission from the dayside only ($f=\frac{1}{2}$; grey dotted line; T_{eq}~2990 K). The $f=\frac{1}{2}$ blackbody model provides an excellent fit to the longer wavelength Ks-band emission, and does a reasonable job of

---

[7]The radiative time-scale (how quickly the planet reradiates the incident stellar flux) is thought to be proportional to $\tau_{rad} \sim \frac{c_P P}{4g\sigma T^3}$ (Showman & Guillot, 2002), where c_P is the specific heat capacity, σ is the Stefan-Boltzmann constant, T is the temperature of the atmospheric layer, and g is the gravitational acceleration of the planet.

[8]It is thought that the advective timescale (how quickly the planet advects the heat to the nightside of the planet; τ_{adv}) can be approximated by the radius of the planet, R_P, divided by the horizontal windspeed, U: $\tau_{adv} \sim R_P/U$ (Showman & Guillot, 2002).

fitting our H and J-band emission ($f=\frac{1}{2}$: $\chi^2=5$); nevertheless it proves a quantitatively better fit than the modest redistribution model ($f=0.35$: $\chi^2=34$), which generally underpredicts the observed emission.

In Figure 6.7 we also compare our measurements to a series of one-dimensional, radiative transfer, spectral models (Fortney et al., 2005, 2006, 2008) with different reradiation factors that specifically include or exclude gaseous TiO/VO into the chemical equilibrium and opacity calculations. In these models when TiO/VO are present in gaseous form in the upper atmosphere they act as absorbers at high altitudes and lead to hot stratospheres and temperature inversions (Hubeny et al., 2003). We present models with modest redistribution ($f=0.35$) and dayside only emission ($f=\frac{1}{2}$) with and without TiO/VO. The associated χ^2 for the $f=\frac{1}{2}$ models with and without TiO/VO are $\chi^2=20$ and $\chi^2=20$, while the $f=0.35$ models with and without TiO/VO are $\chi^2=72$ and $\chi^2=83$. None of these models provide quantitative improvements over the $f=\frac{1}{2}$ blackbody model, as they do not do as good of job of matching the longer wavelength Ks-band thermal emission, nor do they feature reduced emission in H and J-band.

Our near-infrared measurements also allow us to estimate the bolometric dayside luminosity of WASP-12b, L_{day}. We use a blackbody model with a total reradiation factor equal to the best-fit value we calculate from our three near-infrared bands ($f_{tot}=0.441$); by integrating over this model we can estimate L_{day} as $1.12\times10^{-3}L_{\odot}$. Another way of parameterizing the efficiency of the day-to-nightside heat redistribution rather than the reradiation factor is comparing the bolometric dayside luminosity, L_{day}, to the nightside luminosity, L_{night}. By following elementary thermal equilibrium calculations one can deduce that WASP-12b should display a total bolometric luminosity of $L_{tot} = 1.25\times10^{-3}L_{\odot}$. This suggests that 89% of the incident stellar irradiation is reradiated by the dayside, leaving a mere 11% to be advected to the nightside and reradiated. However, caution is encouraged with this conclusion as shorter and longer wavelength emission for this planet may deviate significantly from that of a blackbody.

4.5.4   Future Prospects

We lastly note that the combination of thermal emission as prominent as that displayed here with near-infrared photometry this precise suggests the possibility that thermal phase curve measurements may be possible from the ground. For the shortest period exoplanets ($P\sim1d$ or less) even in a single night of observing (8-9 hours) one could conceivably view the flux maximum of the phase curve where hot gas is advected downwind on the planet, the decrement in flux during the secondary eclipse, and then view a significant fraction of the near-sinusoidal decrease as the cool nightside face of the exoplanet rotates into sight. WASP-12b is an ideal target for such observations with its short $1.09d$ period, and its bright dayside emission suggests that thermal phase curve observations for this planet should reveal a large asymmetry over the

course of the orbit as WASP-12b's nightside should be cold. Thermal phase curve observations from the ground in the near-infrared would require one to control the background systematic trends that are present in our near-infrared photometry even after we correct the flux of our target star with a great many reference stars; the feasibility of this task is, as of yet, unproven. Nevertheless, we will be investigating the possibility of obtaining such near-infrared phase curve information in this photometry as well as with future observations of WASP-12b. These near-infrared phase curve observations will be accompanied by near-simultaneous, 3.6 and 4.5 μm Spitzer/IRAC thermal phase curve observations of a full orbit of WASP-12b (P.I. P. Machalek) that will allow for an unprecedented understanding of the characteristics of the day and nightside deep atmosphere of this planet.

We also plan to reobserve a full, rather than partial, eclipse of WASP-12b in J-band so as to better define its thermal emission at that wavelength. Lastly we plan to observe the transit of WASP-12b in the near-infrared Ks and H-bands, combined with our aforementioned planned reobservations of the eclipse of WASP-12b in these bands. These combined transit and eclipse observations will allow us to confirm if the Ks-band eclipse is indeed longer in duration than the optical transit, and if so whether this is due to material tidally stripped from the planet that may or may not form a circumstellar disk in this system.

Chapter 5

Broadband Transmission Spectroscopy of the super-Earth GJ 1214b suggests a Low Mean Molecular Weight Atmosphere

5.1   Abstract

We used the Wide-field Infrared Camera on the Canada-France-Hawaii telescope to observe four transits of the super-Earth planet GJ 1214b in the near-infrared. For each transit we observed in two bands nearly-simultaneously by rapidly switching the WIRCam filter wheel back and forth for the duration of the observations. By combining all our J-band ($\sim$1.25 μm) observations we find a transit depth, analogous to the planet-to-star radius ratio squared, in this band of $(R_{PJ}/R_*)^2$=1.338$\pm$0.013% – a value consistent with the optical transit depth reported by Charbonneau and collaborators. However, our best-fit combined Ks-band ($\sim$2.15 μm) transit depth is deeper: $(R_{PKs}/R_*)^2$=1.438$\pm$0.019%. Formally our Ks-band transits are deeper than the J-band transits observed simultaneously by a factor of $(R_{PKs}/R_{PJ})^2$=1.072$\pm$0.018 - a 4σ discrepancy. The most straightforward explanation for our deeper Ks-band transit depth is a spectral absorption feature from the limb of the atmosphere of the planet; for the spectral

absorption feature to be this prominent the atmosphere of GJ 1214b must have a large scale height and a low mean molecular weight. That is, its atmosphere would have to be hydrogen/helium dominated and this planet would be better described as a mini-Neptune. However, recently published observations from 0.78 - 1.0 μm, by Bean and collaborators, show a lack of spectral features and transit depths consistent with those obtained by Charbonneau and collaborators. The most likely atmospheric composition for GJ 1214b that arises from combining all these observations is less clear; if the atmosphere of GJ 1214b is hydrogen/helium dominated then it must have either a haze layer that is obscuring transit depth differences at shorter wavelengths, or significantly different spectral features than current models predict. Our observations disfavour a water-world composition, but such a composition will remain a possibility for GJ 1214b, until observations reconfirm our deeper Ks-band transit depth or detect features at other wavelengths.

5.2   Introduction

Astronomers have been waiting for sometime for a planet remotely similar to our own Earth that could be readily investigated with current instruments. Such an object was recently announced with the seminal discovery of the super-Earth planet GJ 1214b (Charbonneau et al., 2009) with the MEarth telescope network (Nutzman & Charbonneau, 2008; Irwin et al., 2009). Although not the first transiting super-Earth announced – CoRoT-7b arguably holds that honour (Leger et al., 2009; Queloz et al., 2009; Pont et al., 2011) – GJ 1214b is in many ways more interesting as it offers the opportunity for advantageous follow-up to constrain its planetary characteristics. With a mass of 6.55 $M_\oplus$ and a radius of 2.68 $R_\oplus$, GJ 1214b's density ($\rho \sim 1.87$ g cm^{-3}; Charbonneau et al. 2009) is less than that of the terrestrial planets of our solar system and therefore GJ 1214b may have a significant gaseous atmosphere. Also, as it transits a low mass star, its equilibrium temperature ($T_{eq} \sim 500$K assuming a low Bond albedo) is much more hospitable than CoRoT-7b, and it has a much more favourable planet-to-star radius ratio; as a result, if there are significant spectral features in its atmosphere then they should be detectable with current instruments.

As there are no super-Earth analogues in our solar system, it is a pressing question whether the burgeoning class of planets with minimum masses below $10 M_\oplus$ (e.g. Udry et al. 2007; Mayor et al. 2009a,b) are predominantly scaled-down Neptunes, with large helium-hydrogen atmospheric envelopes, or scaled-up terrestrial planets with atmospheres predominately composed of heavier molecules. Fortunately, GJ 1214b is an ideal candidate to answer such questions; Miller-Ricci & Fortney (2010) showed that due to GJ 1214b's advantageous scale-height and planet-to-star radius ratio it should have readily observable water and methane spectral

features across the infrared spectrum if its atmosphere is composed primarily of hydrogen and helium. Conversely, if its atmosphere is composed predominantly of heavier molecules, then the resulting smaller scale height will mute the spectral features and current instruments will return transit depths consistent with the depths measured in the optical by Charbonneau et al. (2009).

Furthermore, recent theoretical work has shown that measurements to constrain the composition of the gaseous atmosphere of GJ 1214b will also constrain the planet's bulk composition. Rogers & Seager (2010) and later Nettelmann et al. (2011) showed that the observed mass and radius (Charbonneau et al., 2009) can be equally well fit by either a significant rocky core/mantle and a hydrogen-rich atmosphere, or a "water-world" with a small water-rich core and a significant steam atmosphere. Searches for spectral features will differentiate between these two scenarios; detections of prominent spectral features will argue for the former scenario of a rocky core to go along with the hydrogen/helium-rich gaseous planetary envelope.

Recently, Bean et al. (2010) have performed just such transit spectroscopy observations using the FORS2 instrument on the VLT; Bean et al. (2010) obtained 11 spectrophotometric light curves from 0.78 - 1.0 μm that show consistent transit depths with one another. By comparing to the Miller-Ricci & Fortney (2010) atmospheric models they were able to show that the lack of observed spectral features suggest that GJ 1214b must either have a high mean molecular weight and is likely a water-world, or its atmosphere is hydrogen/helium dominated with hazes or clouds high in the atmosphere that obscure the expected spectral features shortward of $\sim$1 micron. An additional possibility could certainly be that GJ 1214b's atmosphere is more complicated than expected, and its atmosphere could still be hydrogen/helium dominated with different spectral features than the Miller-Ricci & Fortney (2010) models suggest.

We have also performed broadband transmission spectroscopy observations searching for GJ 1214b's spectral features from $\sim$1-2.5 microns using the Wide-field Infrared Camera (WIRCam) on the Canada-France-Hawaii telescope (CFHT). We have already successfully demonstrated the precision of WIRCam on CFHT in the near-infrared through our detections of the secondary eclipses and thermal emission for TrES-2b and TrES-3b in the Ks-band (Croll et al., 2010a,b), and for WASP-12b in the J, H & Ks-bands (Croll et al., 2011). Here we report observations of several transits of the super-Earth GJ 1214b in three bands with WIRCam on CFHT; for each transit we observed near-simultaneously in two bands to allow for accurate comparisons of the transit depths between these two bands. We observe an increased transit depth in the Ks-band as compared to the J-band depth, likely indicative of absorption near $\sim$2.15 μm. The only way to achieve an absorption feature this prominent is if GJ 1214b has a large scale height, a low mean molecular weight, and thus its atmosphere is hydrogen/helium dominated. We discuss below the likely possibilities for the atmospheric make-up of GJ 1214b that result from

a combination of the Bean et al. (2010), Charbonneau et al. (2009) and our own data. Our results disfavour a water-world composition, but such a composition is possible if our Ks-band point is simply an outlier; such a composition will remain a distinct possibility until further observations either confirm our increased Ks-band depth or detect spectral features at other wavelengths. The observations to date are most qualitatively consistent with a hydrogen/helium dominated atmosphere that is either hazy or one with more complicated spectral features than our current models suggest, such as an atmosphere where non-equilibrium chemistry plays a significant role.

5.3 Observations and Data Reduction

We observed the transit of GJ 1214b on four occasions with WIRCam on CFHT. For each transit we observed GJ 1214 in two bands nearly simultaneously by rapidly switching the WIRCam filter wheel back and forth between the two filters. We observed GJ 1214 alternating between the J ($\sim$1.25 μm) and Ks ($\sim$2.15 μm) filters on the evenings of 2010 June 27, 2010 August 15 and 2010 September 22. On the evening of 2010 August 7 we observed GJ 1214 alternating between the J and CH$_4$On filters ($\sim$1.69 μm); these 2010 August 7 observations were of a partial transit only, as the airmass of GJ 1214 increased during transit and during egress reached an airmass of $\sim$2.3, close to the hard limit of the telescope, preventing further observations. For the 2010 June 27 transit the airmass was low for the duration of the observations, while for the 2010 August 15 and 2010 September 22 transits the airmass increased throughout the observations and exceeded an airmass of two by the end of the out-of-transit baseline. For these latter two observations we noticed that the data quality significantly degraded as the airmass rose above 2.0; for the analysis that follows we therefore exclude the data in the out-of-transit baseline with an airmass greater than two for the 2010 August 15 and 2010 September 22 observations.

We observed GJ 1214 in Staring Mode (Devost et al., 2010) where we use the full WIRCam array with its 21arcmin×21arcmin field-of-view and do not dither for the duration of our observations. The only exception to our normal staring mode practice was the aforementioned filter change. The exposure times and defocus amounts for our various observations were: 3.5 s and 2.0 mm for Ks-band, 4 s and 1.2 mm for the CH$_4$On-filter, and 3.5 s and 1.8 mm for J-band, respectively. The filter change during our observations induced an additional overhead of 20 seconds to switch the filter wheel, as well as an additional 60 seconds to take two acquisition images to fine-tune the target position and reinitiate guiding. We observed in data-cubes of 12 exposures to increase the observing efficiency. We took 12 exposures (one guide-cube) in a single filter, before performing the filter change and observing an additional 12 exposures in the other filter. The resulting duty cycles were: 22% for our J and Ks-band observations, and
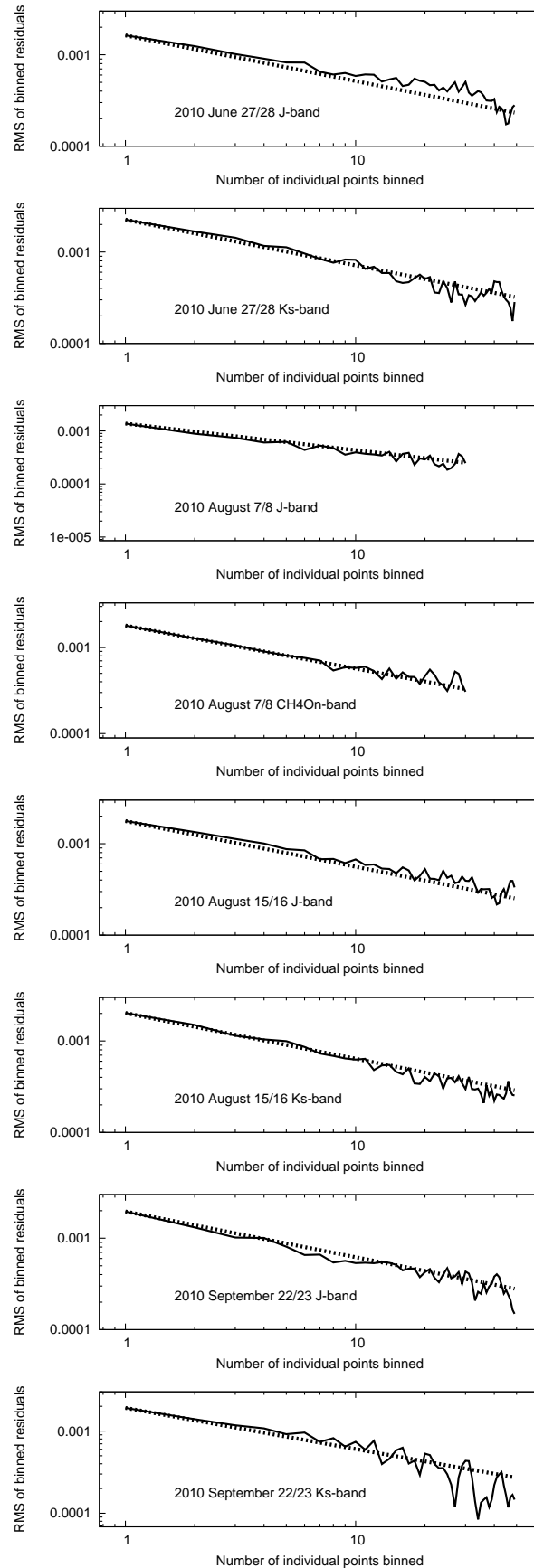
Figure 5.1 The root-mean-square of our out-of-eclipse photometry (solid line) after the subtraction of their respective background trends for our various data-sets. The dashed line in each panel displays the one over the square-root of the bin-size expectation for Gaussian noise.
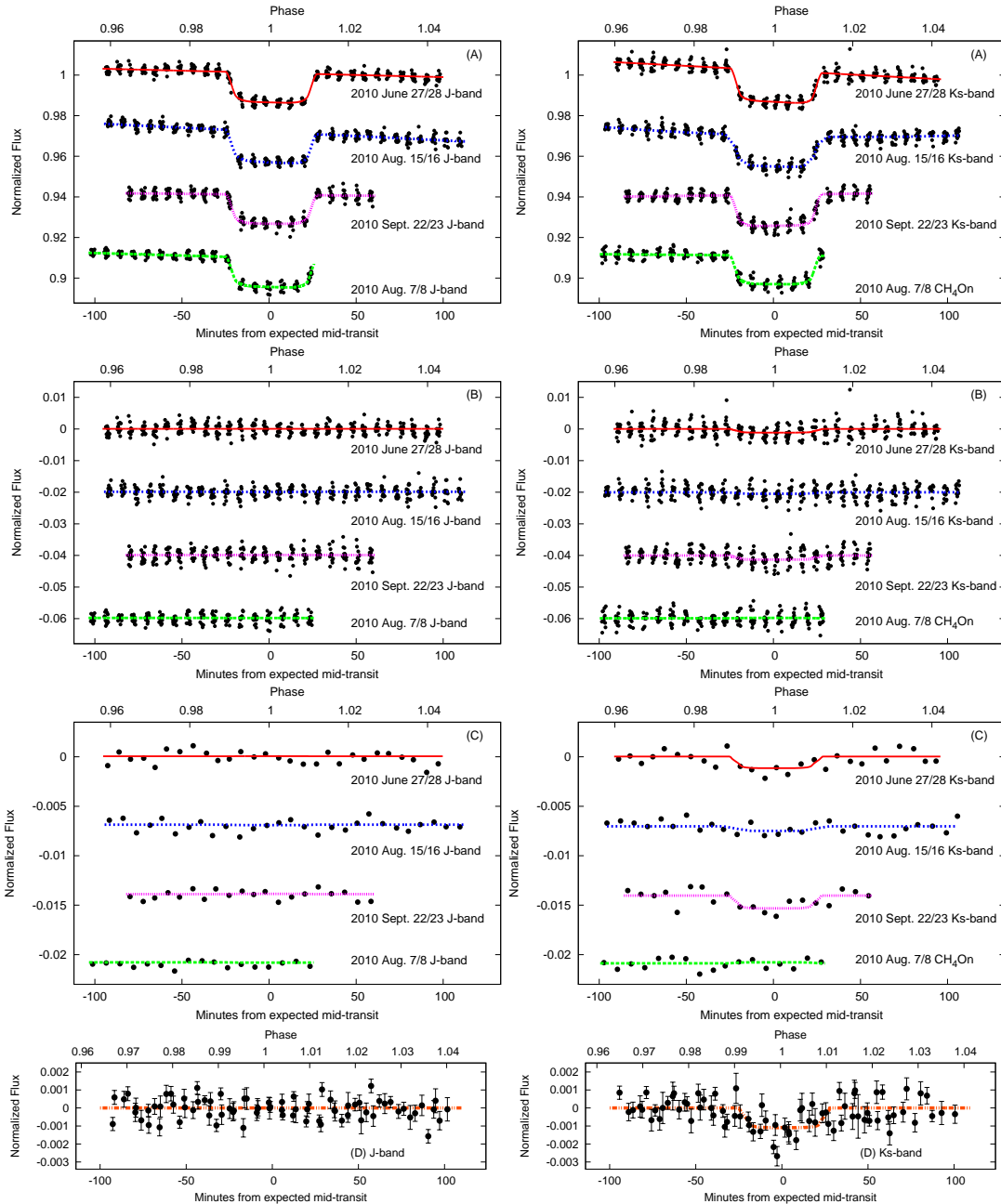
Figure 5.2 CFHT/WIRCam photometry bracketing the transit of GJ 1214 obtained nearly simultaneously on the nights denoted in the figure in the J-band (left panels) and the Ks-band and the CH$_4$On filter (right panels). The top set of panels (A) show the data and the best-fit transit model displayed with the appropriately coloured line. The second set of panels (B) show the residuals of the data and the models from a transit model with a depth given by the best-fit value of the individual J-bands transits at left. Thus the (B) left panel simply displays the residuals from the best-fit transit model from that night's data. The (B) right panel displays the residuals of the Ks and CH$_4$On filter data and model from a transit with a depth equal to the best-fit J-band transit depth observed on that night nearly simultaneously and using the appropriate Ks or CH$_4$On limb-darkening coefficients. The third set of panels (C) are the same as the (B) panels, except with the data binned every twelve points. The bottom panels (D) display all the data obtained simultaneously in the J and Ks-bands from the (C) panels binned every twelve points [that is the top three transit curves in the ABC panels]; the orange dot-dash line displays the difference from the best-fit J-band transit model using the combined J and Ks-band best-fit depths (§5.5). The errors in this panel are calculated from the standard deviation of the points within each bin. The best-fit Ks-band transits display increased transit depths, while the best-fit CH$_4$On transit displays a smaller transit depth than the J-band transits observed simultaneously. In the top three panels the different data-sets are offset vertically for clarity. Note each set of panels has a different vertical scale.

19% for our CH_4On and J-band observations.

The data were reduced and aperture photometry was performed on our target star and numerous reference stars. We used apertures with radii of 17, 18 and 15 pixels for our Ks, J and CH_4On photometry, respectively; the associated inner and outer radii for the sky annuli were 21 and 29 pixels for our Ks-band and CH_4On photometry, and 22 and 30 pixels for our J-band photometry. We preprocess our data using the I'iwi pipeline, designed specifically for WIRCam imaging. We performed differential photometry on the target star with between 13-25 reference stars for our photometry in our various bands; for further details on the method we refer the reader to Croll et al. (2010a,b). As can be seen in Figure 6.2, the out-of-transit photometry after subtraction of the background trend (§8.5) bins down near the Gaussian noise expectation with increasing bin size in all cases. Our data is therefore not seriously affected by time-correlated red-noise. We set our errors for our transits equal to the root mean square of the data outside of transit after the subtraction of a linear trend; for our J and CH_4On photometry on 2010 August 7 we scale up the errors from the RMS by a factor of $\frac{5}{4}$ as this data is of a partial transit only, and the egress of transit occurs at very high airmass, which we found to be correlated with degraded precision with our other data-sets. The resulting light curves for the various observations are displayed in the top panel of Figure 5.2.

5.4   Results

We fit each of our data-sets with a Mandel & Agol (2002) transit model, with the depth of transit, $(R_p/R_*)^2$, and the best-fit mid-transit time as free parameters[1]. For several of our GJ 1214 datasets we noticed obvious trends with time after our differential photometry was performed, similar to the trends noticed in several of our existing WIRCam datasets (e.g. Croll et al. 2010a,b, 2011). We cannot rule out that these trends are intrinsic to the target star and could be due to, for instance, long-term stellar variability as a result of rotational modulation. However, the frequency with which we observe such trends suggests that most of these trends are likely systematic in nature. We therefore refer to these trends as background trends, and we fit our datasets with linear or quadratic backgrounds of the form:

$$B_f = 1 + b_1 + b_2dt + b_3dt^2 \tag{5.1}$$

where dt is the time interval from the beginning of the observations and b_1, b_2 and b_3 are fit parameters. To determine whether a quadratic (b_3) term is justified to account for the background trend, we calculate the Bayesian information criterion (BIC; Liddle 2007), and

---

[1]We quote the barycentric Julian date in the terrestrial time standard using the routines of (Eastman et al., 2010).

ensure that the BIC is lower with the inclusion of the quadratic term. That is, the reduction in χ^2 must be sufficient to justify the extra degree of freedom. Only the August 15 Ks-band data warranted a quadratic term (b_3).

We employ Markov Chain Monte Carlo (MCMC) fitting as described in Croll (2006) and Croll et al. (2010a) using chains with 5×10^6 steps. There are four free parameters for each data-set: $(R_p/R_*)^2$, the best-fit mid-transit time, b_1, and b_2. We also fit our data with the "residual-permutation" method (Winn et al., 2009) where the residuals to the best-fit data are shifted and refit, thus preserving the time correlation of any red-noise in the data, so as to investigate the impact of time correlated systematics. We find similar results to our MCMC analysis, although in general the errors are slightly larger. The increased size of the errors otherwise is likely due to low number statistics as in this method for N data-points one can only generate $2N$-1 light curve permutations ($\sim$200-350 iterations for each of our data-sets). For these reasons we quote our MCMC results henceforth.

We employ a quadratic limb-darkening law and obtain our limb-darkening parameters from Claret et al. (1998) for the J, Ks and CH_4On filters – we adopt their H-band limb-darkening parameters for our CH_4On filter observations. The Claret et al. (1998) limb-darkening parameters are calculated through fits to the PHOENIX stellar atmosphere models (Hauschildt et al., 1997a,b). We employ the parameters c_2 and c_4 from non-linear limb darkening laws, as quoted in Table 8.1. For the input values that we use to generate the limb-darkening parameters we use approximations to the measured stellar effective temperature ($T_{eff} = 3026$ K), and log of the stellar surface gravity (log g = 4.991 [CGS units], Charbonneau et al. 2009), of $T_{eff} = 3000$ K and log g = 5.0. We adopt the period and ephemeris of GJ 1214b given in Bean et al. (2010). We use the inclination and semi-major axis to stellar radius ratio[2] determined from an analysis from the Bean et al. (2010) white-light curves (J. Bean electronic communication). All other parameters were fixed at the Charbonneau et al. (2009) values. Our best-fit MCMC transit and background fits for each of our individual transit datasets are listed in the "Ind." rows of Table 8.1 and displayed in the appropriately coloured lines of Figure 5.2.

As discussed below (§5.5) we note a small, but significant difference in the transit depths we measure in the J and Ks-bands. To confirm that this difference is significant, and not due to any uncertainty in the limb-darkening coefficients[3] we also fit our three J & Ks-band transits simultaneously while fitting the two quadratic limb-darkening coefficients for each band (c_{2J}, c_{4J}, c_{2Ks}, and c_{4Ks}). We place a priori constraints on the limb-darkening coefficients; these priors on the limb-darkening coefficients are Gaussian with a standard deviation of 0.05 from

---

[2] An inclination of i=88.94^o and a semi-major axis to stellar radius ratio of a/R_s=14.97.

[3] We also used quadratic limb darkening coefficients from Lester & Neilson (2008) and a model without limb-darkening. In both cases our Ks-band transit depths were significantly deeper than the J-band depths.

the values derived from Claret et al. (1998) (and listed in the "Ind." rows of Table 8.1 for the J and Ks-bands). For each of our three transits we fit the Ks and J-band data-sets with their own background terms (e.g. b_{1J}, b_{2J}, b_{1Ks}, and b_{2Ks} for the 2010 June 27 transit). We fit for the three mid-transit times of our three transits (to allow for possible transiting timing variations), but ensure that this value is held in common between the J and Ks-band transits observed simultaneously. We fit for the J-band transit depths, but fit the Ks-band transits with a depth that is a consistent factor $[(R_{PKs}/R_{PJ})^2]$ greater, or less than, the J-band transit observed nearly simultaneously for all three transits. By utilizing this fitting method, in addition to the methods discussed below in §5.5.3, we can directly ascertain how much deeper the Ks-band transits are than the J-band transits. The advantage of fitting for the depth of each of the J-band transits individually, rather than fitting them with a consistent depth, is that this allows for small variations in the J-band depth that could arise from rotational modulation (as discussed in §5.5.2), while still directly fitting for the ratio of the Ks to J-band transit depths. We fit for 24 parameters overall, and the best-fit results are listed in the rows marked "Joint" analysis in Table 8.1.

5.4.1 WIRCam non-linearity correction

We also ensured that any difference in the transit depth from the J to Ks-bands was not due to an ineffective non-linearity correction. During the I'iwi preprocessing step, a non-linearity correction is applied to correct the count levels for pixels that approach saturation. Near saturation this non-linearity correction can be as large as 10%. At the maximum count levels recorded in a pixel of the aperture of our target star, GJ 1214, during our observations, the detector is well below its saturation level, and the WIRCam detector is approximately 3-5% non-linear at these count levels. The vast majority of the pixels in our target star and reference stars apertures are illuminated to much lower levels and are expected to be non-linear at the 1-3% level. If this non-linearity correction was applied ineffectively then this could cause a systematic offset in our measured transit depths; although this discrepancy was expected to be much smaller than the difference in the transit depth from J to Ks that we measure, we nonetheless demonstrated this was the case by reprocessing and reanalyzing our 2010 September 22 transit data in the J and Ks-bands without applying the non-linearity correction. Any deviations in the pixel count values from the current non-linearity correction, will be more than an order of magnitude smaller than the effect induced by not applying the non-linearity correction whatsoever. Not employing the non-linearity corrections, as expected, leads to shallower transit depths than when the non-linearity correction is applied. However, the ratio of the transits depths from Ks to J are near identical whether the non-linearity correction is, or is not, applied. Overall, as this test should create a variation much larger than one due

Table 5.1.   CFHT/WIRCam near-infrared transit depths of GJ 1214b

Date in 2010	Filter	Fit Type[a]	Mid-Transit Time (BJD-2450000)	$(R_p/R_*)^2$ (%)	b1	b2	b3	c2	c4
June 27	J	Ind.	$5375.8500^{+0.0001}_{-0.0002}$	$1.334^{+0.020}_{-0.021}$	$0.00542^{+0.00017}_{-0.00020}$	$-0.034^{+0.002}_{-0.002}$	n/a	1.24	-0.67
		Joint	$5375.8501^{+0.0001}_{-0.0001}$	$1.350^{+0.022}_{-0.018}$	$0.00543^{+0.00019}_{-0.00017}$	$-0.034^{+0.002}_{-0.002}$	n/a	$1.22^{+0.05}_{-0.04}$	$-0.69^{+0.04}_{-0.04}$
June 27	Ks	Ind.	$5375.8500^{+0.0001}_{-0.0001}$	$1.459^{+0.030}_{-0.029}$	$0.00780^{+0.00026}_{-0.00026}$	$-0.064^{+0.004}_{-0.003}$	n/a	1.06	-0.59
		Joint	$5375.8501^{+0.0001}_{-0.0001}$	$1.435^{+0.034}_{-0.034}$	$0.00777^{+0.00024}_{-0.00028}$	$-0.065^{+0.003}_{-0.003}$	n/a	$1.07^{+0.03}_{-0.05}$	$-0.57^{+0.04}_{-0.03}$
August 7	J	Ind.	$5416.9404^{+0.0001}_{-0.0001}$	$1.302^{+0.044}_{-0.040}$	$0.00624^{+0.00028}_{-0.00026}$	$-0.035^{+0.007}_{-0.008}$	n/a	1.24	-0.67
		Joint	n/a	n/a	n/a	n/a	n/a	n/a	n/a
August 7	CH_4On	Ind.	$5416.9402^{+0.0002}_{-0.0004}$	$1.290^{+0.050}_{-0.043}$	$0.00512^{+0.00035}_{-0.00031}$	$-0.010^{+0.008}_{-0.009}$	n/a	1.22	-0.66
		Joint	n/a	n/a	n/a	n/a	n/a	n/a	n/a
August 15	J	Ind.	$5424.8424^{+0.0004}_{-0.0002}$	$1.368^{+0.026}_{-0.021}$	$0.00739^{+0.00020}_{-0.00023}$	$-0.060^{+0.002}_{-0.003}$	n/a	1.24	-0.67
		Joint	$5424.8423^{+0.0001}_{-0.0001}$	$1.364^{+0.021}_{-0.024}$	$0.00734^{+0.00020}_{-0.00021}$	$-0.060^{+0.002}_{-0.002}$	n/a	$1.22^{+0.05}_{-0.04}$	$-0.69^{+0.04}_{-0.04}$
August 15	Ks	Ind.	$5424.8423^{+0.0001}_{-0.0001}$	$1.422^{+0.032}_{-0.034}$	$0.00703^{+0.00007}_{-0.00026}$	$-0.098^{+0.007}_{-0.002}$	$0.442^{+0.029}_{-0.056}$	1.06	-0.59
		Joint	$5424.8423^{+0.0001}_{-0.0001}$	$1.450^{+0.036}_{-0.036}$	$0.00708^{+0.00024}_{-0.00029}$	$-0.097^{+0.010}_{-0.003}$	$0.426^{+0.037}_{-0.066}$	$1.07^{+0.03}_{-0.05}$	$-0.57^{+0.04}_{-0.03}$
September 22	J	Ind.	$5462.7722^{+0.0002}_{-0.0002}$	$1.307^{+0.034}_{-0.031}$	$0.00493^{+0.00030}_{-0.00031}$	$-0.013^{+0.005}_{-0.005}$	n/a	1.24	-0.67
		Joint	$5462.7722^{+0.0001}_{-0.0001}$	$1.329^{+0.026}_{-0.028}$	$0.00497^{+0.00027}_{-0.00031}$	$-0.012^{+0.005}_{-0.006}$	n/a	$1.22^{+0.05}_{-0.04}$	$-0.69^{+0.04}_{-0.04}$
September 22	Ks	Ind.	$5462.7722^{+0.0002}_{-0.0002}$	$1.424^{+0.044}_{-0.031}$	$0.00406^{+0.00032}_{-0.00035}$	$0.016^{+0.006}_{-0.007}$	n/a	1.06	-0.59
		Joint	$5462.7722^{+0.0001}_{-0.0001}$	$1.412^{+0.039}_{-0.039}$	$0.00406^{+0.00028}_{-0.00038}$	$0.015^{+0.006}_{-0.006}$	n/a	$1.07^{+0.03}_{-0.05}$	$-0.57^{+0.04}_{-0.03}$

[a]Fit Type stands for the joint or individual (Ind.) analyses.

to an ineffective non-linearity correction, it is safe to conclude that the greater Ks-band than J-band transit depth does not arise from the non-linearity correction.

5.5   Discussion

5.5.1   GJ 1214b's transit depth in the near-infrared

We display our best-fit transit depths in Figure 5.3 and Table 8.1. The J-band transit depths are largely consistent with one another and are also consistent, or at most insignificantly shallower, than the depths reported by (Charbonneau et al., 2009) and Bean et al. (2010) in the optical and very near-infrared. The Ks-band transits also display similar depths to one another. However, the Ks-band transits appear to be deeper than the J-band transits; this is a small effect, but is clearly visible in the bottom panel of Figure 5.2 where we present the residuals of our observations from the best-fit J-band transit depths observed nearly simultaneously.

The CH_4On transit depth, on the other hand, appears to have a similar transit depth to the the J-band transit observed simultaneously on 2011 August 7. As this is a partial transit only, and as much of the transit and the egress of transit occurs at very high airmass, caution is warranted in any robust comparison of the J to CH_4On transit depth and to other wavelengths.

By combining all the Ks-band and J-band transits, we find the weighted means and the associated errors on the transit depths are $(R_{pJ}/R_*)^2$=1.338±0.013% for J-band, and $(R_{pKs}/R_*)^2$=1.438±0.019%

for Ks-band. As we only have one partial transit of GJ 1214 in the CH_4On filter, the depth in that band is simply the value from the 2010 Aug. 7 transit: $(R_{pCH_4On}/R_*)^2=1.290^{+0.050}_{-0.043}\%$. We determine the error on the weighted mean of our J-band and Ks-band points by determining the weighted error of all our observations in that particular band and then scaling that error upwards by a factor of ζ. To determine ζ we calculate the χ^2 of all our data in a single band compared to a model with a consistent transit depth equal to the weighted mean of the transit depths in that band; we then scale up the errors to ensure the reduced χ^2 is equal to one[4]. The Ks-band data-points are consistent with one another, so only the J-band errors are scaled upwards. The resulting value is $\zeta_J=1.02$ for the J-band photometry, so this suggests that both the Ks and J-band weighted errors are already appropriately sized, or close to it. Overall, this analysis suggests that our Ks-band and J-band transit depths are inconsistent with one another; the Ks-band transit depth is deeper than the J-band depth with 5σ confidence.

5.5.2   The effect of stellar spots on transit observations of GJ 1214b

Charbonneau et al. (2009) reported that GJ 1214 is an active star and displays longer term variability with a period of several weeks at the 2% level in the MEarth bandpass. More recently, Berta et al. (2010) presented and analyzed MEarth photometry of GJ 1214 from 2008 to 2010 and observed long-term photometric variability at the 1% level with a period of approximately 50 days. This variability is presumably due to rotational modulation from spots rotating in and out of view. As the long-term photometric monitoring presented in Berta et al. (2010) ends in 2010 July (in the midst of the observations we present here) we assume the more conservative limit of 2% variability for our calculations henceforth.

Transit observations obtained at different epochs may show small differences in the transit depth due to rotational modulation arising from both occulted and unocculted spots (Czesla et al., 2009; Berta et al., 2010; Carter et al., 2011). In the case of unocculted spots, if the 2% observed rotational modulation represents the full range from a spotted to unspotted photosphere[5] then we may expect measurements of the transit depth of GJ 1214b will vary by as much as 0.03% of the stellar signal in the MEarth bandpass (assuming an unspotted transit depth of 1.35%) from observations taken at epochs spanning the maximum and the minimum of the observed rotational modulation. On the other hand, occulted spots will cause small brightening events during the transit that may lead one to underestimate the true transit depth. Thus,

---

[4]Andrae et al. (2010) notes that there are several hidden assumptions one should be careful to address when applying reduced χ^2 to one's data; we feel the method we apply here should be useful nonetheless as a first-order approximation to indicate the appropriate size of the weighted error bars

[5]There is no reason to expect we ever observe a hemisphere of the star free of spots altogether, and indeed the analysis of Carter et al. (2011) and Berta et al. (2010) suggest we very well may not, which would lead to larger transit depth differences from epoch to epoch. Exact analytical expressions are available in Carter et al. (2011).
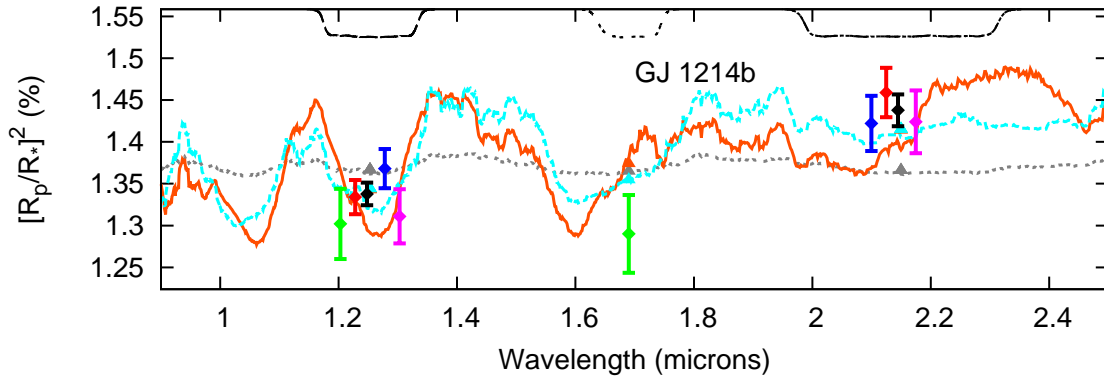
Figure 5.3 WIRCam transit observations of the super-Earth GJ 1214b. The WIRCam response functions are displayed inverted at the top of the plot using the black dotted lines at an arbitrary scale; these are from left to right: J-band ($\sim$1.25 μm), the CH$_4$On filter ($\sim$1.69 μm), and Ks-band ($\sim$2.15 μm). Our J and Ks-band observations are indicated by the red diamonds for our 2010 June 27 observations, the blue diamonds for our 2010 August 15 observations, and the magenta diamonds for our 2010 September 22 observations. Our 2010 August 7 J-band and CH$_4$On filter observations are indicated by the green diamonds. We offset our measured J and Ks observations slightly in wavelength for clarity. For the Ks and J-band we display the weighted mean and error of the observations in these bands with the black diamonds. The orange solid and cyan dashed curves are the Miller-Ricci & Fortney (2010) GJ 1214b atmospheric models for solar metallicity hydrogen/helium dominated atmospheres (with and without methane, respectively). The grey dotted curve is the Miller-Ricci & Fortney (2010) models for an H$_2$O/steam atmosphere. We integrate the Miller-Ricci & Fortney (2010) atmospheric models over the WIRCam response functions and display these values in the appropriately coloured solid triangles.

for transit depth measurements obtained at different epochs, such as our own, it is possible that the variability caused by rotational modulation creates small differences in the measured depths for observations taken at different epochs.

However, for our data obtained nearly simultaneously in two different bands, the effect of spots should be reduced for the following reasons. First of all, as the stellar rotation period of GJ 1214 appears to be much longer (Charbonneau et al., 2009; Berta et al., 2010) than the $\sim$1 hour duration of the transit, the spot pattern should be essentially static during a single transit. Secondly, even if the star is very spotted during our own observations, the difference between the transit depths measured nearly simultaneously in our two bands will be minute. This small difference will arise due to the differing ratio of the Planck function of the spot and the star due to their different temperatures; however, this difference will be muted as we move into the near infrared. For instance, assuming that GJ 1214 has spots 500 K cooler – a value supposedly consistent with another M4.5 dwarf (Zboril et al., 2003) – than GJ 1214's $\sim$3000 K effective temperature (Charbonneau et al., 2009), the 2.0% variability due to rotational modulation in the MEarth bandpass ($\sim$780 nm), will translate into 1.5%, and 1.0% variability in J-band and Ks-band, respectively. Assuming the unspotted transit depth is 1.350% in these bands then the maximum transit depths from unocculted spots, which would results from measurements at the minimum flux of the observed rotational modulation, would be 1.369% in J and 1.364% in Ks-band. The variation in the transit depth between the J and Ks-bands that we observe is both much larger than this predicted effect due to starspots, and also would serve to create a deeper transit in J-band, rather than Ks-band; we, of course, observe the opposite phenomenon.

A deeper Ks-band than J-band transit could arise from spots along the transit chord that are occulted during the observations. Occultation of spots by a planet will create anomalous brightenings during transit, as has been observed for the transiting planets HD 189733b (Pont et al., 2007), TrES-1b (Rabus et al., 2009; Dittmann et al., 2010), and more recently for GJ 1214b (Bean et al., 2010; Berta et al., 2010; Carter et al., 2011). However, due to the near-simultaneous nature of our photometry, it is unlikely that occulting spots could account for the variation in Ks to J-band transit depth that we observe, again due to the small difference in the Planck functions of the spot relative to the star between our two bands. For instance, occulting a spot 500 K cooler than the surrounding photosphere that is 30% of the planetary size, will lead to transits that are 0.07% shallower for the duration of the occultation than the presumed 1.35% transit depth in J-band. However the Ks-band transit depth will also be 0.05% shallower; the 0.02% relative difference between the two bands expected from a spot occultation is much less than the observed transit depth difference we observe. Lastly, as spot occultations will lead to overall shallower transit depths, one would require the true transit depth of GJ 1214b to be deeper than that observed in our own J-band observations and in the optical and
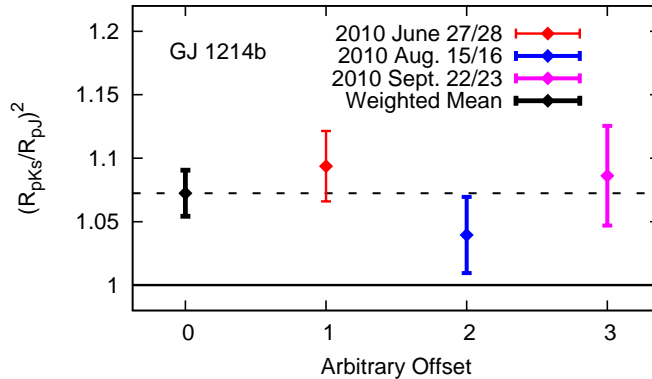
Figure 5.4 The measured Ks-band transit depth divided by the measured J-band transit depth for the "Ind." analysis of our various observations (see the legend). The horizontal dotted line denotes the weighted mean of the Ks divided by J-band transit depth, $(R_{PKs}/R_{PJ})^2$. The solid horizontal solid line denotes the value if the Ks-band transits were the same depth as the J-band transits.

very near-infrared (Charbonneau et al., 2009; Bean et al., 2010). For these reasons we find it unlikely that the transit depth difference we observe arises from occulted or unocculted spots.

5.5.3 A larger transit depth in Ks-band than J-band

Due to the aforementioned possible variations in the transit depths from epoch to epoch induced by spots, a more straightforward method to compare the depths of transits in our bands is to directly compare the depth of the transit in one band to the depth obtained simultaneously in another - that is $(R_{PKs}/R_{PJ})^2$ for each one of our transits observed simultaneously in the Ks and J-bands. We ignore our data observed on 2010 August 7 for this analysis, as GJ 1214 was observed in the J-band and the CH_4On filter, rather than in J and Ks.

We attempt to measure the fraction that the Ks-band transits are deeper than the J-band transits, $(R_{PKs}/R_{PJ})^2$, by two methods. In the first method, we display the best-fit MCMC transit depth of our Ks-band photometry divided by the J-band transit depth from our individual analysis ("Ind.") in Figure 5.4. The associated errors displayed in this figure are generated by propagating through the associated errors on the individual best-fit MCMC transit depths as displayed in Table 8.1. The weighted mean and error of these data indicates that the Ks-band transits are deeper than the J-band transits by a factor of: $(R_{PKs}/R_{PJ})^2=1.072\pm0.018$. The associated errors do not need to be scaled up, as the reduced χ^2 is near one for a comparison of our three $(R_{PKs}/R_{PJ})^2$ data-points as compared to the weighted mean of these observations; specifically $\chi^2=1.92$, which is reasonable given the two degrees of freedom[6] By analyzing the

---

[6] We again note there are several hidden assumptions one should be aware of when applying reduced χ^2 as
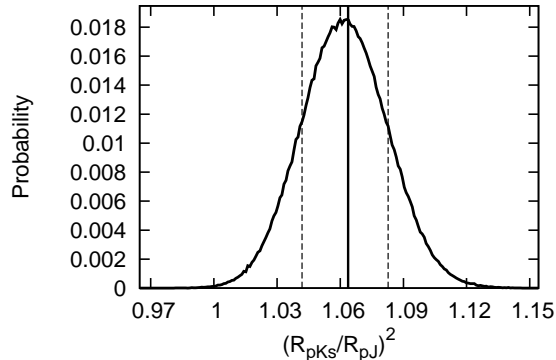
Figure 5.5 The measured Ks-band transit depth divided by the measured J-band transit depth from our "Joint" analysis. The vertical solid line denotes the best-fit value, while the dotted vertical lines indicate the 68% credible regions.

individual transits, our Ks-band photometry displays a deeper transit depth than our J-band photometry observed nearly simultaneously with a confidence in excess of 4σ.

In the second method we use the "Joint" MCMC analysis described above where we simultaneously fit the three three data-sets that observe in Ks-band and J-band simultaneously. We fit each J-band transit with an independent transit depths, but assume all the Ks-band transits were a consistent factor deeper (or shallower) than the J-band transits observed nearly simultaneously, $(R_{PKs}/R_{PJ})^2$. We also fit the limb-darkening parameters after applying a Gaussian a priori assumption as described in §8.5. We display this ratio for our "Joint" analysis in Figure 5.5; we measured this fraction as $(R_{PKs}/R_{PJ})^2 = 1.063^{+0.019}_{-0.021}$. This distribution is not a perfect Gaussian, and therefore, according to this method our Ks-band transits are deeper than our J-band transits with greater than 3σ confidence.

Both methods return reasonably similar results, and argue for a deeper Ks-band transit depth than J-band transit depth with a confidence in excess of 3σ. We quote the value of $(R_{PKs}/R_{PJ})^2$ from our "Ind." results henceforth.

5.5.4 WIRCam transit depths suggest a low mean molecular weight

The transit depths from our CFHT/WIRCam photometry suggests that GJ 1214b should have a large scale height, low mean molecular weight and thus a hydrogen/helium dominated atmosphere. These conclusions arise from the fact that our Ks-band transit depths are deeper than our J-band transit depths by a factor of $(R_{PKs}/R_{PJ})^2 = 1.072 \pm 0.018$. This corresponds to a relative change in the radius of GJ 1214b from the Ks-band to the J-band of 1.04%, or ~ 610 km compared to GJ 1214b's radius of ~ 17070 km. Using its equilibrium temperature

---

documented in §5.5.1.
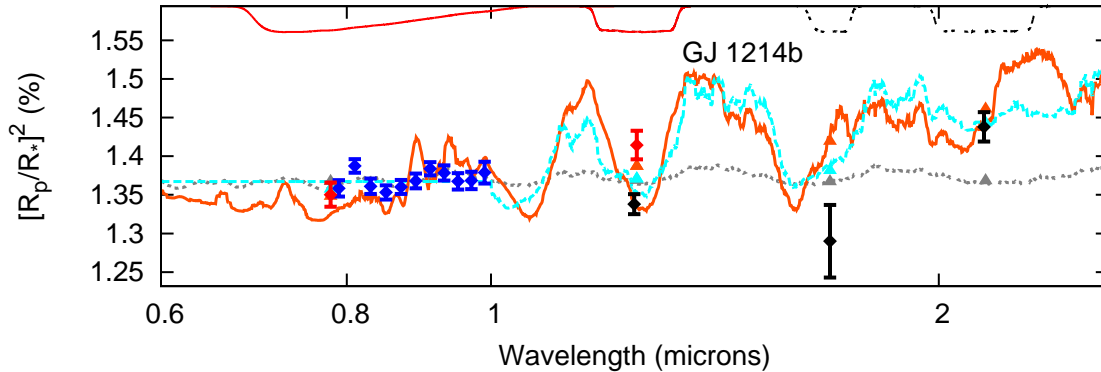
Figure 5.6 Transit observations of the super-Earth GJ 1214b. The response functions are displayed inverted at the top of the plot at arbitrary scale. These are from left-to-right the MEarth ($\sim$0.78 μm), and Kitt-peak J-band ($\sim$1.25 μm) displayed in the red-curves, and the WIRCam J-band ($\sim$1.25 μm), CH$_4$On filter ($\sim$1.69 μm), and Ks-band ($\sim$2.15 μm) displayed in the black dotted curves. The Kitt-peak J-band bandpass overlaps the CFHT J-band bandpass. The VLT/FORS2 response functions are not included, as they essentially overlap with the points. The weighted mean of our J-band, Ks-band and CH$_4$On filter observations are displayed by the black diamonds. The MEarth (Charbonneau et al., 2009), and the Kitt-peak Sada et al. (2010) transit depth are displayed with the red diamonds, while the VLT/FORS2 points Bean et al. (2010) are displayed with blue diamonds. We display two Miller-Ricci & Fortney (2010) GJ 1214b atmospheric models (a water-world model [grey dotted curve], and a solar-metallicity model [orange solid curve]); the other model we present in the cyan dashed curve is a Miller-Ricci & Fortney (2010) solar-metallicity no methane model at wavelengths longer than one micron, while at shorter wavelengths we arbitrarily cut off the predicted absoprtion to simulate the impact of putative hazes. We integrate these atmospheric models over the WIRCam response functions and display these values in the appropriately coloured solid triangles. We caution that this comparison does not correct the depths for possible variability due to rotational modulation and thus any comparison should be considered illustrative, rather than definitive.

of $T_{eq} \sim 560$ K (the value obtained assuming zero bond albedo) this amounts to absorption increasing the radius of GJ 1214b by ~ 2 atmospheric scale heights for a hydrogen gas envelope (H_2). As, the molecular weight of H_2O is approximately nine times greater than hydrogen gas, a spectral feature this prominent assuming a water world composition would require an increase in the planetary radius of ~ 20 atmospheric scale heights. This suggests that an atmosphere dominated by light elements is much more probable than one composed of heavier elements.

The change in transit depth due to a change in planetary radius between the line, R_{PL}, and the continuum, R_{PC}, can be related to the scale height, H, and the opacities in the absorption line, κ_l, and the continuum, κ_c; this value can be approximated by the ratio of the opacities multiplied by the area of an annulus one scale height thick relative to that of the stellar disk:

$$(R_{PL}/R_*)^2 - (R_{PC}/R_*)^2 = \frac{2\pi R_P H}{\pi R_*^2} \ln(\kappa_l/\kappa_c). \qquad (5.2)$$

(Brown et al., 2001). To cause the observed transit depth difference in a hydrogen gas atmosphere would require line opacity marginally greater than that of the continuum ($\kappa_l/\kappa_c \sim 8$); the water-world composition would require an opacity that is unrealistically larger than that of the continuum ($\kappa_l/\kappa_c \sim 2\times 10^8$). Therefore from our CFHT/WIRCam observations, one would expect that the atmosphere of GJ 1214b must have a low mean molecular weight, a large scale height, and thus an atmosphere dominated by hydrogen and/or helium.

We compare our data to the Miller-Ricci & Fortney (2010) atmospheric models of GJ 1214b in Figure 5.3. We first employ the most conservative scenario and assume that due to rotational modulation, or other systematic errors, that we cannot directly compare our measured transit depths to the Charbonneau et al. (2009) or Bean et al. (2010) depths. We thus scale-up or down the predicted absorption of the Miller-Ricci & Fortney (2010) models by a multiplicative factor, analogous to an increase or decrease of the squared ratio of the planetary to stellar radius, to produce the best-fit (minimum χ^2) compared to our observations. We display the Miller-Ricci & Fortney (2010) water-world model (an H_2O dominated world) in the dotted grey line. We compare to two hydrogen-helium dominated atmospheres; the first has solar-metallicity (orange dot-dash line) while the second has solar metallicity but does not feature methane (cyan dot-dashed line). We integrate these models over the WIRCam response functions and calculate the associated χ^2 of our data compared to the model. Although, we cannot strongly differentiate between hydrogen-helium envelopes with solar metallicity ($\chi^2_{solar}=9$) from those without methane ($\chi^2_{no-methane}=7$), the water-world composition is disfavoured ($\chi^2_{H_2O}=26$) by greater than 2σ for our seven degrees of freedom. Other high mean molecular weight models (e.g. the Miller-Ricci & Fortney (2010) CO_2-dominated or H_2O/CO_2-mixture atmospheres) are disfavoured with similar confidence. The support for the hydrogen/helium composition arises from the observed increased absorption in Ks-band as opposed to our J-band observations. The

CH_4On filter is nominally 1σ discrepant from the observed models; it is unclear at this present time whether this discrepancy is physical or simply due to low signal-to-noise.

5.5.5 Comparison to observations at other wavelengths

Arguably, completely excluding the constraints imposed by transit depth observations at other wavelengths, because of the effects of spots or systematic effects, is unnecessarily conservative. Therefore, we also compare the weighted means of our transit depth measurements and the Miller-Ricci & Fortney (2010) models to the Charbonneau et al. (2009) depth measurement in the MEarth bandpass, the J-band measurement of Sada et al. (2010), and the Bean et al. (2010) measurements from 0.78-1.0 μm in Figure 5.6. We do not attempt to make a correction for the possibly variable spot activity between the various epochs at which the data were obtained; as discussed above in §5.5.2 rotational modulation can be expected to induce spurious transit depth variations as large as 0.03% of the ~1.35% transit depth of GJ 1214b near 1 μm, and will cause smaller variations at longer wavelengths. Also, a small discrepancy will be induced by the fact that Sada et al. (2010) and Charbonneau et al. (2009) transit depth measurements were produced with the original Charbonneau et al. (2009) estimates of the inclination and other parameters for this system, rather than the values derived from the Bean et al. (2010) white light photometry that we use here and that have been applied to the Bean et al. (2010) spectrophotometry. For these reasons we caution that this comparison should be considered illustrative, rather than definitive.

Of the original Miller-Ricci & Fortney (2010) atmospheric models the heavy mean molecular weight models, such as the water-world composition model ($\chi^2_{H_2O}$=40), are highly favoured over the low mean molecular weight compositions (χ^2_{solar}=101 for the solar metallicity hydrogen/helium dominated envelope).[7] The water-world composition is favoured over the solar metallicity hydrogen/helium dominated model with more than 5σ confidence. This is unsurprising, as it is largely the conclusion of the Bean et al. (2010) paper, and results from the high precision of the VLT/FORS2 spectrophotometry and the lack of observed spectral features in the very near-infrared. The Bean et al. (2010) paper excludes the expected methane and water spectral absorption features from a hydrogen/helium dominated atmosphere from 0.78 - 1.0 μm with high confidence.

Another possibility to explain the lack of observed spectral features are high altitude hazes (Fortney et al., 2005) in the atmosphere of GJ 1214b that could mute the spectral features at shorter wavelengths. We discuss this possibility further below (§5.5.6). We thus also compare our observations to a no methane model where we cut off the absorption below 1 μm and set it

---

[7]As explained above in §5.5.4, we scale the radii of the planet in the models up or down to achieve the minimum χ^2 compared to the data.

equal to a nominal value of 1.35%. At wavelengths greater than 1 μm, the values are identical to the no methane model. This abrupt transition is not intended to be physical, but simply illustrative of the impact hazes could have on the expected transmission spectrum at shorter wavelengths[8]. This model has the lowest χ^2 ($\chi^2_{hazy-hydrogen}$=34) of any of the models as it is able to address the lack of observed spectral features in the Bean et al. (2010) spectrophotometry, and our deeper Ks-band depth compared to our J-band depth[9]. We note that the improvement in the χ^2 of this haze model to the water-world model is not significant, and both remain leading candidates to explain all the observations of GJ 1214 to date, as discussed below.

5.5.6   Possible atmospheric compositions of GJ 1214b

All the transmission spectroscopy observations of GJ 1214b to date could be explained by a high mean molecular weight atmosphere if our deeper Ks-band transit is simply an outlier. If GJ 1214b's atmosphere does have a high mean molecular weight, a water vapour atmosphere is a leading possibility. This water-world scenario will remain a viable candidate until observations are performed to either confirm that our Ks-band transit depths are indeed deeper, or spectral features are detected at other wavelengths.

A scenario that would qualitatively explain all the observations to date, is a hydrogen/helium dominated atmosphere with thick hazes that would mute the presence of spectral features arising from shorter wavelengths due to scattering. This haze layer would have to be at high altitudes, and low pressures (<200 mbar), to effectively mute the expected spectral features that would arise from being able to stare deep into the atmosphere of the planet in opacity windows in the very near-infrared. The efficiency of scattering diminishes for wavelengths longer than the approximate particle size (Hansen & Travis, 1974). The haze particles could not be much smaller than sub-micron size to account for the the lack of observed spectral features in the Bean et al. (2010) spectrophotometry in the very near-infrared. Due to the expected size of these putative haze particles, shorter wavelength optical observations would not be expected to show simply the monotonic increase in planetary radius expected from a Rayleigh scattering signal, but instead the more complicated transmission spectrum signal of Mie scattering (see for example Lecavelier des Etangs et al. 2008).

Such a haze or cloud layer is certainly not inconceivable. A cloud deck or haze has been

---

[8]Depending on the size of the particles one would expect the observed transit radius to increase at very short wavelengths due to Rayleigh scattering or have a more complicated behaviour due to Mie scattering.

[9]While this paper was in the late stages of revision, Desert et al. (2011) presented Spitzer 3.6 and 4.5 μm channel observations of the transit of GJ 1214b. They find similar transit depths in these bands to those found by Bean et al. (2010) and Charbonneau et al. (2009) in the very near-infrared. If methane is present in the atmosphere of GJ 1214b it should cause increased absorption in the 3.6 μm channel; as this is not observed, if the atmosphere of GJ 1214b is hydrogen/helium dominated, the combination of all the observations to date argues in favour of the hazy hydrogen/helium dominated model without methane.

reported to mute the optical transmission spectrum from 0.29 - 1.05 μm of the hot Jupiter HD 189733b (Pont et al., 2008; Sing et al., 2011); in the infrared HD 189733b may have absorption features with an opacity even greater than those that result from the haze at those wavelengths (Desert et al., 2010). The hazes of Jupiter and Titan may be other suitable analogies. Titan has a haze layer that is optically thick in the optical, but has transparent windows as one moves into the near-infrared (Tomasko et al., 2008; Griffith et al., 1993). The opacity of hazes on Jupiter are high at short optical wavelengths, but are much smaller as one moves into longer optical wavelengths and into the near-infrared (Rages et al., 1999).

A potential culprit for the particle causing this haze is a hydrocarbon derived from the photochemical destruction of methane (Moses et al., 2005; Zahnle et al., 2009a). Methane is found in the atmospheres of all the solar system's giant planets, as well as Titan. The end product of the breakdown of methane are higher order hydrocarbons that condense as solids (Rages et al., 1999). Since GJ1214b should be relatively cool ($T_{eq}\sim$500K) its atmospheric carbon inventory could feature abundant methane, like Jupiter. Particulates with a relatively small mixing ratio can have important effects at the slant viewing geometry appropriate for transits (Fortney et al., 2005), and thus hydrocarbons in a high altitude haze are one possible explanation the lack of observed features in the Bean et al. (2010) spectrophotometry.

We lastly note, that the actual spectral features of GJ 1214b, whether its atmosphere is hydrogen/helium dominated or not, could be more complicated and thus very different than the Miller-Ricci & Fortney (2010) models predict. One such reason could be the impact of non-equilibrium chemistry, which will be explored in a forthcoming publication (Miller-Ricci Kempton et al. in prep.).

Clearly further observations are required to differentiate between these scenarios and determine the true atmospheric makeup of GJ 1214b.

An opacity source at $\sim$2.15 μm

The increased transit depths we note in our Ks-band observations, argue for an opacity source near $\sim$2.15 microns that is causing increased absorption along the limb of the planet. One such, possible opacity source is methane, which is predicted to cause absorption from $\sim$2.2 to $\sim$2.4 μm in the Miller-Ricci & Fortney (2010) hydrogen-helium dominated atmospheric models. Although our Ks-band transit depth is qualitatively consistent with this methane spectral absorption feature, we note that the Miller-Ricci & Fortney (2010) hydrogen/helium model with solar metallicity but without methane, provides a near-identical goodness-of-fit as compared to the solar metallicity model with methane. This is because the methane absorption feature is present at the red-edge of our Ks-band only; on the blue edge of the Ks-band the hydrogen/helium model with methane actually features less absorption than the model without methane, so overall the

predicted transit depth is similar whether methane is or is not present according to the Miller-Ricci & Fortney (2010) prediction. Also, greater concentrations of methane in the atmosphere are not expected to cause increased absorption at these wavelengths. In the no methane model, the increased Ks-band absorption compared to J-band results from water opacity. Thus both water and methane remain viable candidates for this increased absorption. Both these molecules should also lead to spectral features from 0.78 - 1.0 μm that have been ruled out by the Bean et al. (2010) spectrophotometry at high confidence. Thus for these chemicals to remain viable opacity sources, one requires the presence of hazes in the atmosphere of GJ 1214b, or that the spectral features are more complicated than the Miller-Ricci & Fortney (2010) models predict. We encourage further modelling to elucidate whether this ~2.15 μm feature is due to methane, water or another opacity source.

5.5.7   Consequences of a hydrogen/helium dominated atmosphere

A hydrogen/helium dominated atmosphere on GJ 1214b would be expected to undergo significant hydrodynamic escape. Therefore, if GJ 1214b is hydrogen/helium dominated then it may have lost or is losing a significant fraction of its gaseous envelope. Charbonneau et al. (2009) and Rogers & Seager (2010) predicted that if GJ 1214b's atmosphere is dominated by hydrogen gas then it will lose on the order of ~10^9 gs^{-1}, or ~0.02 $M_\oplus$ on a 4 Gyr timescale[10]. As its host star may have been more active earlier in its life, and thus brighter in the ultraviolet, its cumulative mass loss may be higher. Thus, either if GJ 1214b's hydrogen/helium envelope is primordial or due to outgassing we may expect it to have lost and will be losing a non-negligible fraction of its atmosphere.

Also, Carter et al. (2011) have pointed out that the radius of the star, GJ 1214, that one obtains from stellar evolutionary models is very different than the radius one obtains from an analysis of the light curve. As a result the density of GJ 1214b varies accordingly, from one where a significant gaseous atmosphere is likely, to a much higher density where one would only expect a thin gaseous atmosphere on top of a solid terrestrial planet. Our increased Ks-band transit depth argues in favour of the lighter density and the stellar radius suggested by fits to light curve parameters.

Constraints on GJ 1214b's bulk composition

If the atmosphere of GJ 1214b is hydrogen/helium dominated then this allows us to place a constraint on the planet's bulk composition, namely its core, mantle and possibly its ice layer (Rogers & Seager, 2010; Nettelmann et al., 2011). This is because the lighter atmospheric

---

[10]Charbonneau et al. (2009) report a 3-10 Gyr age for this system

composition of a hydrogen/helium atmosphere, compared to for instance a water-world composition, requires a heavier interior composition of silicates, ferrous material or ices to compensate in order to fit the observed mass and radius – and thus density – constraints of Charbonneau et al. (2009). We compare our results to two numerical models (Rogers & Seager, 2010; Nettelmann et al., 2011) that attempt to determine the range of realistic bulk compositions that agree with the observed mass and radius constraints. Regardless of whether the planet's hydrogen/helium envelope is primordial or due to outgassing, it is expected that this atmospheric layer will be a small percentage ($\sim$5%) of this planet's total mass (Rogers & Seager, 2010; Nettelmann et al., 2011). Nettelmann et al. (2011) and Rogers & Seager (2010) predict, under their hydrogen/helium atmosphere scenarios, that a wide range of core/mantle masses is still viable (from a few percent to $\sim$99% of the mass of GJ 1214b). The higher core/mantle masses result from a planet with very little water, while for the lower masses it would entail a massive interior water/ice layer. Nettelmann et al. (2011) suggest that if this planet's atmosphere is dominated by hydrogen and helium then one can place an upper limit on the water to rock ratio of approximately six-to-one; the true value of this quantity is expected to be much lower, and thus the core mass is expected to make-up at least $\sim$14% of the planet's mass and likely much more (Nettelmann et al., 2011).

5.6   Conclusions

We report observations of four transits of GJ 1214b using WIRCam on CFHT. We observed nearly simultaneously in J-band and in Ks-band for three of the transits, and in J-band and the CH_4On filter in another. Our best-fit J-band transit depth is consistent with the values obtained in the optical and very near-infrared: $(R_{PJ}/R_*)^2$=1.338$\pm$0.013%. Our Ks-band transit is deeper: $(R_{PKs}/R_*)^2$=1.438$\pm$0.019%. Our J and Ks-band transit depths are inconsistent at the 5σ level. The impact of spots and rotational modulation on the transit depths we observe should be small; nevertheless spots will induce small changes in the transit depths we measure from epoch to epoch, and as a result a better metric to quantify our observations may be the factor that the Ks-band transits are deeper than the J-band transits observed simultaneously. Our Ks-band transits display a deeper depth than our J-band transits by a factor of $(R_{PKs}/R_{PJ})^2$=1.072$\pm$0.018. We thus detect increased transit depths in our broadband Ks-band ($\sim$2.15 μm) as compared to J-band ($\sim$1.25 μm) with 4σ confidence. The difference in transit depth between the two bands that we measure is best explained due to a spectral absorption feature from the atmosphere of GJ 1214b; the only way to get a spectral absorption feature this prominent is if the atmosphere of GJ 1214b has a large scale height, low mean molecular weight and is thus hydrogen/helium dominated. Water or methane are possible opacity sources

to explain this absorption. If GJ 1214b's atmosphere is hydrogen/helium dominated a range of core/mantle masses and ice layers is still viable, but the planet must have a large rocky core/mantle interior to its gaseous envelope. In this case, our increased Ks-band transit depth would be the first detection of a spectral feature in a super-Earth atmosphere, and GJ 1214b would best be described as a mini-Neptune.

However, when combining our observations with other observations of GJ 1214b, most specifically the lack of spectral features observed in the Bean et al. (2010) VLT/FORS2 spectrophotometry from 0.78 - 1.0 μm, the atmospheric composition of GJ 1214b is less clear. There are several leading possibilities. One possibility remains that the atmosphere of GJ 1214b is water-vapour dominated and our increased Ks-band transit depth is simply an outlier; our increased Ks-band transit depth will have to be reconfirmed or spectral features at other wavelengths will have to be detected before this scenario can be confidently ruled out. The possibility that is arguably the most consistent with all the observed data to date, is that GJ 1214b has a hydrogen/helium dominated atmosphere with a haze layer at high altitude consisting of particles that can be no smaller than approximately sub-micron in size; such a scenario would explain the lack of observed spectral absorption features in the very near-infrared in the Bean et al. (2010) spectrophotometry and our own increased Ks-band transit depth if there is an opacity source at $\sim$2.15 μm. Lastly, we note that the true spectrum of GJ 1214b could be more complicated than our models predict for a variety of reasons - one such possibility is the importance of non-equilibrium chemistry in GJ 1214b's atmosphere which would alter GJ 1214b's predicted transmission spectrum (Miller-Ricci Kempton et al. in prep.).

Clearly, further observations are required to precisely determine the nature of GJ 1214b's atmosphere. We encourage further observations to confirm our increased Ks-band transit depth. We plan to use CFHT/WIRCam to reobserve the transit of GJ 1214b in Ks-band on several occasions in the Spring/Summer 2011 observing season.

Chapter 6

A limit on the Temporal Variability of two Ks-band Secondary Eclipses of WASP-3b

6.1 Abstract

We present Ks-band photometry bracketing two secondary eclipses of the hot Jupiter WASP-3b using the Wide-field Infrared Camera on the Canada-France-Hawaii Telescope. We detect the secondary eclipse of WASP-3b on both occasions with a depth of $0.176^{+0.015}_{-0.014}\%$ (12σ) from an analysis of both eclipses. Our best-fit secondary eclipses are consistent with a circular orbit (a 3σ upper limit on the eccentricity, e, and argument or periastron, ω, of $|e\cos\omega| < 0.0042$), suggesting that tidal heating is not responsible for inflating this planet's radius. A secondary eclipse of this depth corresponds to a day-side brightness temperature of $T_B = 2686^{+83}_{-86}$ K, and suggests the planet exhibits extremely inefficient day to night-side redistribution of heat at this wavelength. Our Ks-band eclipse depths are so deep that our analysis suggests that the atmospheric depths probed by our observations likely reradiate much of the incoming stellar flux right at the sub-stellar point without redistributing the heat over WASP-3b's dayside face; even so this layer of the atmosphere appears to be uniformly hotter than suggested by simple arguments. We also find that our two Ks-band eclipses display a consistent depth to within 0.028% or $160K$, ruling out violent differences in weather at the epochs of our two observations. This is the first reported detection of thermal emission for this planet. We note, however, that the depth of secondary eclipse we observe for WASP-3b is dependent on the size of aperture we choose for our aperture photometry; thus further study and investigation of this technique is required before we can be confident that systematic errors are not biasing our measurement

of the thermal emission of this planet.

6.2   Introduction

It is increasingly apparent that multi-wavelength constraints on the thermal emission of hot Jupiters will be necessary for us to understand the global reradiation and advection of heat in these exotic worlds. Single wavelength constraints are eminently useful, but ultimately they only probe a single depth and pressure in the atmospheres of these worlds – atmospheres that could be highly vertically stratified (Langton & Laughlin, 2008; Menou & Rauscher, 2009). Obtaining a well-sampled spectral energy distribution at a series of wavelengths is the most straightforward path forward to understand the energy budgets of these worlds. The Spitzer Space Telescope has allowed such multi-wavelength constraints for a series of hot Jupiters at wavelengths greater than 3 μm (e.g. Knutson et al. 2008; Charbonneau et al. 2008; Machalek et al. 2008). A limitation on measurements with Spitzer, however, is that most hot Jupiters with detectable thermal emission are so hot that the Spitzer wavelengths are longwards of the blackbody peaks of these worlds and thus on the Rayleigh-Jeans tail of these planets' blackbodies. Shorter wavelength constraints, at the peak of these planets' blackbodies, provide measurements of these planets' thermal emission at depth, and better, more model-independent constraints on these planets bolometric luminosities, and energy budgets. Such thermal emission detections have recently been performed from the ground by other researchers (e.g. de Mooij & Snellen 2009; Sing & Lopez-Morales 2009; Rogers et al. 2009; Gillon et al. 2009; Lopez-Morales et al. 2010; Anderson et al. 2010; Gibson et al. 2010; de Mooij et al. 2011), in addition to our program using the Wide-field Infrared Camera (WIRCam) on the Canada-France-Hawaii telescope (CFHT). To date, we've detected the thermal emission of TrES-2b (Croll et al., 2010a), and TrES-3b Croll et al. (2010b) in the Ks-band, and that of WASP-12b in the J, H and Ks-bands (Croll et al., 2011).

To-date multiwavelength constraints have largely been obtained at different epochs, and thus the effective comparison of these measurements relies on the assumption that the thermal emission of these planets is consistent from epoch to epoch. One reason that this may not be the case is if these planets have variable weather and intense storms, such as those that have been theoretically predicted by dynamical atmospheric models of hot Jupiters with simplified radiative transfer. Examples include the two-dimensional shallow water models of Langton & Laughlin (2008) and more recently the three-dimensional Intermediate General Circulation model simulations of Menou & Rauscher (2009); the latter predict brightness temperature variations of $\sim100K$ for a hot Jupiter similar to HD 209458. In addition, there are growing tentative observational signs in favour of epoch to epoch variability, that could be interpreted as
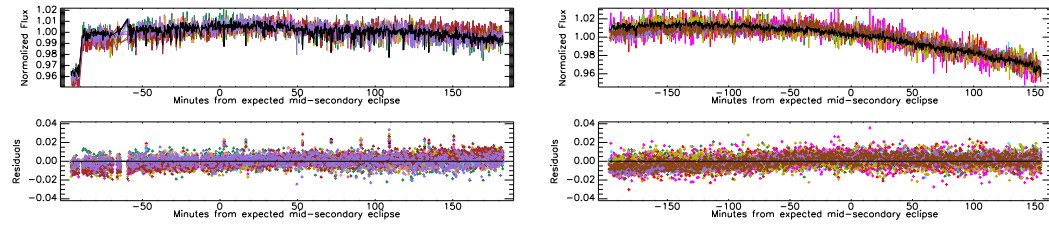
Figure 6.1 Top panels: The flux from the target star (black) and the reference stars (various colours) that are used to calibrate the flux of WASP-3b for our first eclipse (left) and second eclipse (right). Bottom panels: The residuals from the normalized flux of the target star of the normalized flux of the reference stars for our two eclipses (left and right).
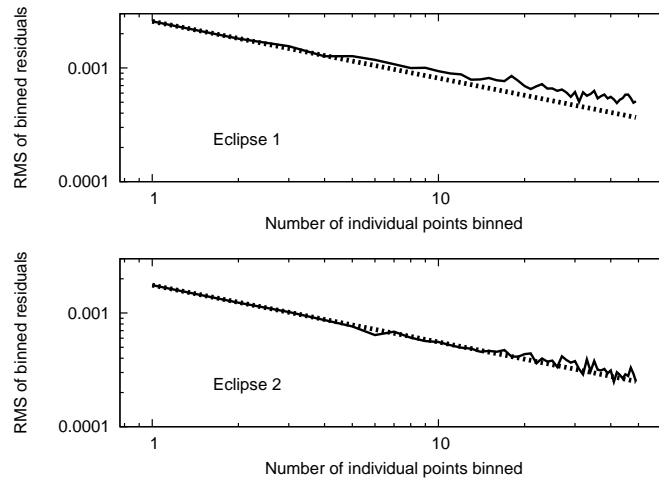
Figure 6.2 The root-mean-square of our out-of-eclipse photometry (solid line) following the various corrections documented in §6.3 for our first Ks-band eclipse (top) and our second eclipse (bottom). In both cases the dashed line displays the one over the square-root of the bin-size expectation for Gaussian noise.

arising from systematic errors or inconsistencies in various analyses, or as the tell-tale signs of weather on hot Jupiters. Although, Agol et al. (2010) place a stringent limit on the variability of HD 189733b, other researchers have presented a number of possible detections of variability for this planet (Madhusudhan & Seager 2009 & references therein). If these variations are real (rather than due to systematic errors), then this casts doubt on many of the aforementioned conclusions that utilize multiwavelength comparisons from observations at different epochs. For these reasons, gaining a better handle as to whether storms and temporal variability are common in the atmospheres of hot Jupiters is paramount.

One method to constrain the temporal variability of a hot Jupiter is to detect its thermal emission in a single band at multiple epochs. This has already been performed with Spitzer in the mid-infrared; the aforementioned Agol et al. (2010) study placed a stringent 2.7% limit (68% confidence) on HD 189733b's temporal variability of its thermal emission from seven eclipses in the 8.0 μm Spitzer/IRAC (Fazio et al., 2004) channel. However, it arguably makes more sense to search for temporal variability in the near-infrared. If we assume blackbody emission, then for a given temperature difference on the planet, the difference in the Planck function will be much greater at shorter wavelengths, than at longer wavelengths (Rauscher et al., 2008). If we assume that observations at $\sim$8.0 μm and observations at $\sim$2.15 μm (Ks-band) probe the same atmospheric layer, then the $\sim$100K temperature difference observed in the Menou & Rauscher (2009) model from eclipse to eclipse for a canonical HD 209458-like atmosphere, will result in eclipse to eclipse variations on the order of 33% of the eclipse depth in Ks-band, compared to 11% of the eclipse depth at 8.0 μm. That is, although the eclipse depth will obviously be much smaller in Ks-band ($F_P/F_* \sim 0.4 \times 10^{-3}$), than at 8.0 μm ($F_P/F_* \sim 2.5 \times 10^{-3}$), the percentage change in this eclipse depth will be larger at shorter wavelengths. There is a competing phenomenon, however; it is generally thought that near-infrared wavelengths probe deeper into the atmosphere of hot Jupiters, as the JHK-bands are windows in the water opacity (Seager et al., 2005b; Fortney et al., 2008; Burrows et al., 2008b). As the radiative timescale is generally thought to increase with pressure, while the advective timescale should be relatively constant (Showman & Guillot, 2002), our shorter wavelength observations may in fact be probing atmospheric layers that are more homogenized, and will therefore display reduced temporal variability. Thus, clearly observations that detect or constrain the temporal variability of hot Jupiters in the near-infrared will inform our understanding of the deep atmosphere of these worlds.

One favourable target for thermal emission measurements in the near-infrared is the transiting hot Jupiter WASP-3b. WASP-3b orbits a F7V star with a period of only $\sim$1.85 d (Pollacco et al., 2008); it also has an advantageous planet-to-star radius ratio ($R_P/R_* \sim 0.10$). It is one of the most highly irradiated hot Jupiters discovered to date, with an incident flux

of $3.5 \times 10^9 \; ergs^{-1}cm^{-2}$, and is therefore a member of the hottest class (the pM-class) of hot Jupiters according to the Fortney et al. (2008) theory. This means this planet is predicted to: redistribute little of its heat from the tidally locked dayside to its nightside, harbour a temperature inversion and a hot stratosphere, and experience increased emission at wavelengths longer than its blackbody peak (Burrows et al., 2008a; Fortney et al., 2008). Even though our near-infrared measurements should be probing deeper pressure regions than the mid-infrared, temperature inversions are still thought to play a role in the intensity of emission one expects in the near-infrared; planets with hot stratospheres are expected to display increased emission in the mid-infrared, and are therefore thought to reradiate less shortwards and at its blackbody peak (Hubeny et al., 2003), in the optical and near-infrared.

WASP-3b was included among our targets to detect thermal emission from the ground using WIRCam on CFHT in the near-infrared. We present here two detections of the Ks-band thermal emission of WASP-3b obtained less than two weeks apart. We detect both eclipses and report a combined 12σ detection of WASP-3b's Ks-band thermal emission. The Ks-band eclipse depth we find for WASP-3b is so deep that it argues for very inefficient redistribution of heat at the atmospheric depth our observations probe, and that this layer is hotter than simple arguments would suggest. As our observations are at a single wavelength it is unclear if this behaviour is isolated to the atmospheric depth and pressure probed by our observations, or if these are global phenomena on WASP-3b. We also find the depths of our two eclipses are consistent, thus ruling out violent storms and significant temperature differences on WASP-3b at the epochs of our two observations.

6.3   Observations and data reduction

6.3.1   Canada-France-Hawaii Observations

The secondary eclipse of WASP-3b (K=9.361) was observed with WIRCam (Puget et al., 2004) on CFHT on two occasions in 2009 June. On 2009 June 3 WASP-3b was observed under photometric conditions for ∼4.7 hours, beginning ∼15 minutes before the predicted start of the eclipse and continuing for ∼2.3 hours after the end of the eclipse (PI B. Croll). On 2009 June 14 WASP-3b was again observed with WIRCam/CFHT (PI M. Cushing) for ∼5.9 hours fairly evenly bracketing the predicted secondary eclipse of the planet. In both cases numerous reference stars were also observed in the 21x21 arcmin field of view of WIRCam.

For the first observation we obtained cubes of twelve 5-second exposures for the first five minutes of the observations and we obtained cubes of twelve 4-second exposures after this point. The shorter exposure time was used after the first few minutes, as we found that during periods of particularly good seeing the pixels of our target were close to saturation. To minimize the

impact of individual pixel flat fielding errors and to keep the flux well below detector saturation the telescope was defocused to 1.0 mm so that the flux of our target star was spread over a ring ∼13 pixels (4 arcsec) in diameter. The effective duty cycle after accounting for readout and for saving exposures was 39%. For the second observation, due to the saturation issue just mentioned, the exposure time was shortened to 3.5 seconds and the telescope was defocused to 1.5 mm such that the flux was spread over an even larger ring 19 pixels (6 arcsec) in diameter. The observations were otherwise identical.

For both observations the data was reduced and aperture photometry was performed as in Croll et al. (2010b) (with the details provided in Croll et al. 2010a). For the first eclipse for our aperture photometry we used an aperture with a radius of 22 pixels, with an annulus with an inner and outer radius of 25 and 35 pixels, respectively, to estimate the sky background. For the second eclipse the aperture radius, and inner and outer radius of the annulus were 18, 23 and 33 pixels, respectively. We tested smaller and larger apertures in increments of 0.5 pixels in a systematic fashion and determined that these aforementioned choices were optimal. Saturated pixels were removed using the I'iwi pipeline[1]. After performing aperture photometry on our target star and a number of suitably bright reference stars we corrected the flux of our target star for each eclipse by normalizing it by a number of nearby reference stars as described in Croll et al. (2010a). We used 11 reference stars for our first eclipse, and 15 reference stars for the second eclipse. The different number of reference stars in each case was chosen such that our photometry displayed the smallest possible point-to-point root-mean-square (RMS) outside of occultation. Following these corrections the point-to-point scatter of our data outside occultation improved from a root-mean-square of 13.7×10^{-3} to 0.71×10^{-3} per 60 sec for our first eclipse and 19.47×10^{-3} to 1.37×10^{-3} per 60 sec for the second eclipse (Figure 6.1). There appears to be some time-correlated red-noise in our photometry, especially in the first eclipse. The out-of-eclipse photometry of our first eclipse bins down marginally above the one-over the square-root of the bin size expectation for Gaussian noise, while that of our second eclipse bins at this limit (Figure 6.2). However, we note that our observations are still well above the predicted photon noise limit of 2.5×10^{-4} per 60 seconds.

6.3.2 Variation of the eclipse depth with aperture size

With our WASP-3 data-sets we noticed that the depth of the eclipse we measure is dependent on the radius of the aperture we choose for our aperture photometry. We note that the effect is particularly pronounced for our 2009 June 14 photometry; this effect is largely negligible for our 2009 June 3 photometry. The origin of this trend is unknown. This effect will require further

---

[1]http://www.cfht.hawaii.edu/Instruments/Imaging/WIRCam/ IiwiVersion1Doc.html
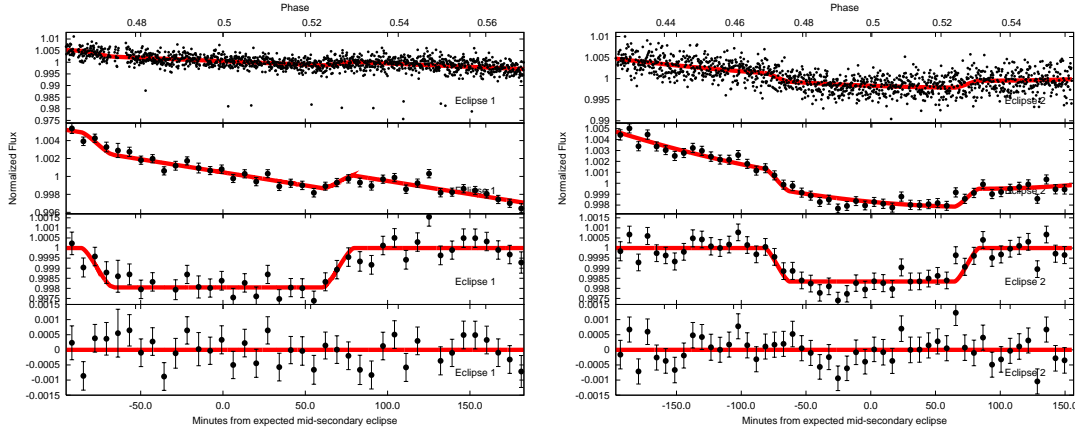
Figure 6.3 WIRCam/CFHT Ks-band photometry of the secondary eclipse of WASP-3b for our first eclipse (left) and our second eclipse (right). The top panels show the unbinned lightcurve, the second panels show the data binned every ∼7.0 minutes. The third panels show the binned data after the subtraction of the best-fit backgrounds, B_f, while the bottom panels show the binned residuals from the best-fit model of each eclipse. The best-fit secondary eclipse and background, B_f, is displayed for each eclipse and panel with the red line.

study before we can be confident that an unaccounted for systematic error is not biasing the depth of the eclipses that we report here. We present the eclipse depths for the aperture sizes we report above below. Further efforts are required to determine whether we can eliminate this variation in the eclipse depth with aperture size, or better quantify the uncertainties in the eclipse depth that results.
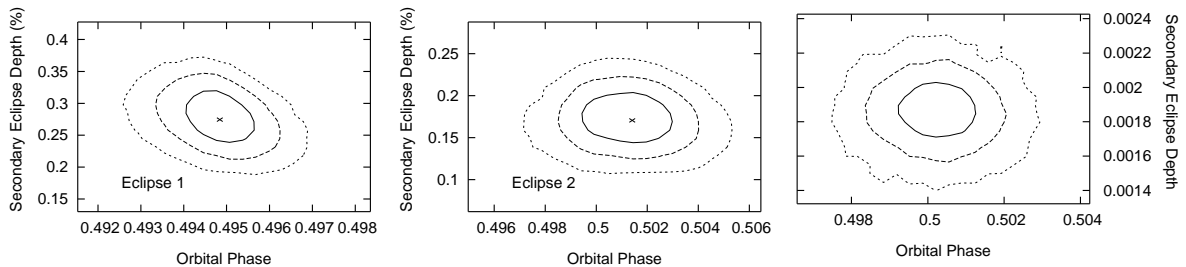
Figure 6.4 The 68.3% (1σ; solid-line), 95.5% (2σ; dashed-line), and 99.7% (3σ; dotted-line) credible regions from independent MCMC analyses for our first eclipse (left), second eclipse (middle), and for a joint analysis of the two eclipses (right). The "x" in the middle of the plots marks the best-fit point from our MCMC analysis.

Table 6.1. WASP-3b's best-fit secondary eclipse parameters

Parameter	MCMC 1st eclipse solution	MCMC 2nd eclipse solution	MCMC joint analysis solution
reduced χ^2	$1.018^{+0.002}_{-0.001}$	$1.048^{+0.002}_{-0.002}$	$1.028^{+0.002}_{-0.001}$
ΔF	$0.195^{+0.021}_{-0.025}$	$0.171^{+0.022}_{-0.017}$	$0.176^{+0.015}_{-0.017}$
t_{offset} min[a]	$-3.5^{+2.8}_{-3.2}$	$3.2^{+2.4}_{-3.7}$	$-0.7^{+1.7}_{-2.8}$
$t_{eclipse1}$[b]	$14986.9201^{+0.0009}_{-0.0009}$	n/a	$14998.0133^{+0.0017}_{-0.0026}$
$t_{eclipse2}$[b]	n/a	$14998.0133^{+0.0017}_{-0.0026}$	$14996.0133^{+0.0017}_{-0.0026}$
ϕ	$0.4989^{+0.0010}_{-0.0012}$	$0.5014^{+0.0009}_{-0.0014}$	$0.4999^{+0.0006}_{-0.0010}$
T_B (K)	2793^{+10}_{-113}	2656^{+120}_{-126}	2686^{+83}_{-86}
$e\cos(\omega)$	$-0.0021^{+0.0016}_{-0.0019}$	$0.0019^{+0.0014}_{-0.0014}$	$-0.0004^{+0.0010}_{-0.0016}$
f	$0.984^{+0.015}_{-0.151}$	$0.804^{+0.156}_{-0.142}$	$0.84^{+0.11}_{-0.10}$
c_1	$0.00521^{+0.00029}_{-0.00037}$	n/a	$0.00493^{+0.00025}_{-0.00021}$
c_2	$-0.042^{+0.002}_{-0.002}$	n/a	$-0.040^{+0.002}_{-0.002}$
d_1	n/a	$0.00485^{+0.00022}_{-0.00020}$	$0.00448^{+0.00022}_{-0.00018}$
d_2	n/a	$-0.051^{+0.005}_{-0.006}$	$-0.052^{+0.005}_{-0.005}$
d_3	n/a	$0.114^{+0.017}_{-0.024}$	$0.128^{+0.018}_{-0.018}$

[a]We account for the increased light travel-time in the system (Loeb, 2005).

[b]$t_{eclipse1}$ and $t_{eclipse2}$ are the barycentric Julian Dates of the mid-eclipse of the first and second eclipses calculated using the terrestrial time standard (BJD-2440000; as calculated using the routines of Eastman et al. 2010).

6.4   Analysis

We first perform independent analyses of our two eclipse data-sets. For our other WIRCam data-sets (Croll et al., 2010a,b, 2011) we have noticed trends in the reduced data that are likely due to unaccounted for variations in the atmospheric transmission, seeing and airmass, guiding errors and/or other effects that affect our target star differently than the reference stars. Although we cannot rule out that some of these trends are intrinsic to our stellar targets, most of these trends are likely systematic and thus we term these trends background trends, B_f, and fit for the effects of these trends in our fitting process. The background of the first eclipse appears linear and thus we fit for its background, B_{f1}, with a function of the form:

$$B_{f1} = 1 + c_1 + c_2 dt \tag{6.1}$$

where dt is the interval from the start of observations and c_1 and c_2 are fit parameters. The background of the second-eclipse displays a concave upwards curve throughout the observations and thus we fit for the background, B_{f2} with a function of the form:

$$B_{f2} = 1 + d_1 + d_2 dt + d_3 dt^2 \tag{6.2}$$

where d_1, d_2 and d_3 are again fit parameters. We confirm that the inclusion of a quadratic term for our second eclipse improves the χ^2 sufficiently, despite the extra degree of freedom, by ensuring that it results in an improved Bayesian information criterion (BIC; Liddle 2007). We also ensure that our first eclipse does not require a quadratic term, by showing that it does not result in an improved BIC.

We perform Markov Chain Monte Carlo fitting for the background, the depth of the secondary eclipse (ΔF) and the offset that the eclipse occurs later than the expected eclipse center (t_{offset}). Our Markov Chain Monte Carlo method is discussed in Croll (2006) and Croll et al. (2010a). We use the Mandel & Agol (2002) algorithm without limb darkening to generate our best-fit secondary eclipse model. We obtain our planetary parameters for WASP-3b from Gibson et al. (2008) and our stellar parameters for WASP-3 from Pollacco et al. (2008).

The best-fit secondary eclipes parameters of each eclipse fit independently are listed in Table 6.1 and presented in Figure 6.3. The phase dependence of these fits is presented in the left panels of Figure 6.4. We also perform a joint analysis of the two secondary eclipses; the fit parameters are thus c_1, c_2, d_1, d_2, d_3, ΔF, and t_{offset}. The resulting best-fit secondary eclipse parameters are listed in Table 6.1. The phase dependence of this joint analysis is displayed in the right panel of Figure 6.4.
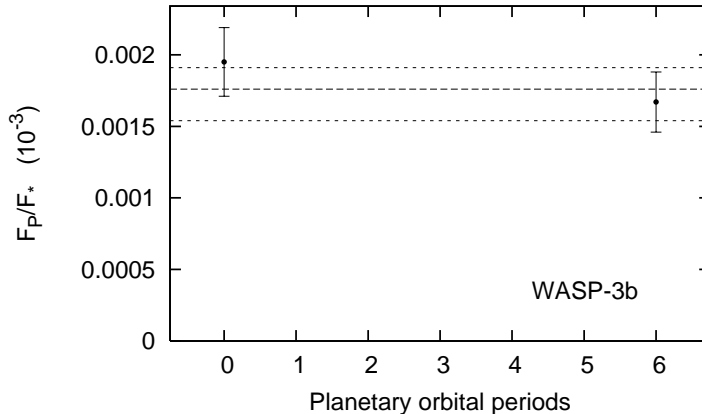
Figure 6.5 Eclipse depths of our two Ks-band eclipses. The dashed-horizontal line is the eclipse depth from our joint analysis, while the dotted-horizontal lines are the 1σ uncertainties on this value.

6.5 Discussion

6.5.1 WASP-3b's near-infrared thermal emssion

We strongly detect both secondary eclipses we observed. The depth of the first eclipse is $0.195^{+0.021}_{-0.025}\%$ (7σ), while the depth of the second is $0.171^{+0.022}_{-0.017}\%$ (10σ). Our Ks-band secondary eclipses are consistent with a circular orbit. The two eclipses are best-fit at a phase of $\phi=0.4989^{+0.0010}_{-0.0012}$ and $\phi=0.5014^{+0.0009}_{-0.0014}$, or at a phase of $\phi=0.4999^{+0.0006}_{-0.0010}$ for the joint analysis. The offsets in phase for the two eclipses are consistent with one another and thus we quote the parameters from the joint analysis here. The corresponding limit on the eccentricity and argument of periastron is $e\cos\omega = -0.0004^{+0.0010}_{-0.0016}$, or a 3σ limit of $|e\cos\omega| < 0.0042$. Thus unless the argument of periastron is close to 90 or 270 degrees, this limit suggests that the "puffed-up" radius of WASP-3b is not due to tidal damping of the orbital eccentricity as has been suggested for similarly inflated hot Jupiters (Bodenheimer et al., 2001, 2003; Liu et al., 2008; Ibgui et al., 2010).

A lack of eclipse to eclipse variability

The depths of our two eclipses have consistent depths to within 0.028% of the stellar flux or $160K$ (Figure 6.5). This rules out violent differences in weather at the epochs of our two observations. In comparison Menou & Rauscher (2009) predict temperature changes on the order of $100\ K$ for a canonical HD 209458-like hot Jupiter from a three-dimensional numerical model. Thus, we can only rule out temperature variations larger than those predicted in Menou & Rauscher (2009). We lastly note that our observations are likely probing a higher pressure
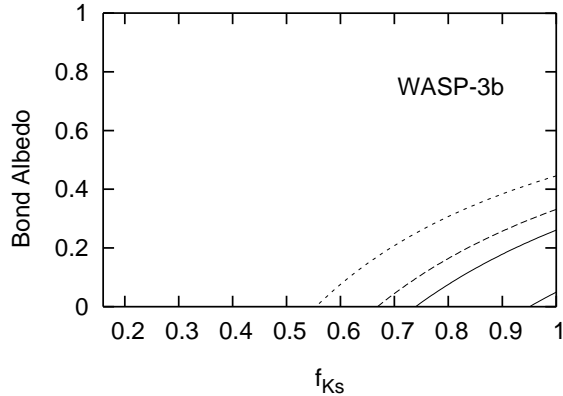
Figure 6.6 The 68.3% (1σ; solid-line), 95.5% (2σ; dashed-line) and 99.7% (3σ; short dashed-line) χ^2 confidence regions on the Ks-band reradiation factor, f_{Ks}, and Bond albedo from the joint analysis of our Ks-band eclipses. Obviously our observations favour a low Bond albedo and inefficient day-to-nightside redistributon of heat.

atmospheric layer, than the lower pressure layer than that simulated in Menou & Rauscher (2009); as explained above, the higher pressure region probed by our observations may be more homogenized than lower pressure, higher altitude atmospheric layers.

WASP-3b's atmosphere

Our joint analysis reveals an eclipse depth of $0.176^{+0.015}_{-0.014}\%$ (12σ). A secondary eclipse this bright necessitates both a near-zero Bond albedo, A_B[2], and very inefficient day to nightside redistribution at the atmospheric depth probed by our observations (Figure 6.6). We parameterize the level of redistributon from the day to nightside by the reradiation factor, f, following the Lopez-Morales & Seager (2007) definition[3]. Although one expects the overall reradiation factor of an exoplanet, f_{tot}, to fall between isotropic reradiation ($f_{tot}=\frac{1}{4}$), and no redistribution and reradiation right at the substellar point ($f_{tot}=\frac{2}{3}$; Burrows et al. 2008a), individual atmospheric layers may display reradiation factors well above or below these values. A single wavelength observation can only constrain the reradiation factor, f_i, at the atmospheric layer probed by that wavelength. We note, as documented in §6.5.2, there are numerous examples of other exoplanets whose eclipses suggest reradiation factors exceeding this nominal $f=\frac{2}{3}$ value at a single wavelength, and thus atmospheric layer. Our best-fit reradiation factor for our Ks-band observations is $f_K=0.84^{+0.11}_{-0.10}$ assuming a zero Bond albedo. Thus even a model that displays

---

[2]The Bond albedo, A_B is the fraction of the bolometric flux reflected from the planet compared to the incident bolometric radiation.

[3]f relates the dayside temperature of the planet, T_p to the stellar effective temperature (T_*), stellar radius (R_*), and semi-major axis of the planet (a): $T_p = T_* \ (R_*/a)^{1/2}[f(1-A_B)]^{1/4}$, in the absence of any intrinsic flux (which for hot Jupiters is much smller than the absorbed and reradiated stellar flux).
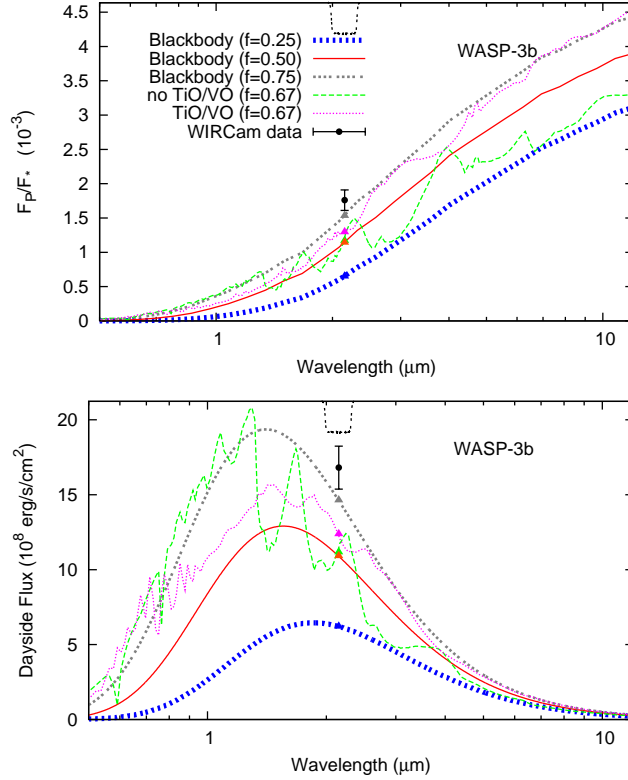
Figure 6.7 Dayside planet-to-star flux ratios (top) and dayside flux at the planet's surface (bottom). The Ks-band point (~2.15 μm) is from our joint analysis of our two eclipses. Blackbody curves for isotropic reradiation ($f=\frac{1}{4}$; $T_{eq}\sim1984$ K; blue dashed line), dayside only emission ($f=\frac{1}{2}$; $T_{eq}\sim2359$ K; red line) and highly peaked dayside emission ($f=\frac{3}{4}$; $T_{eq}\sim2611$ K; grey dotted line) are also plotted. We also plot one-dimensional, radiative transfer spectral models (Fortney et al., 2006, 2008) for various reradiation factors and with and without TiO/VO. We plot models with a reradiation factor indicative of no redistribution (f=0.67) with and without TiO/VO (magenta-dotted and green-dashed lines, respectively). The models with TiO/VO display temperature inversions. The models on the top panel are divided by a stellar atmosphere model (Hauschildt et al., 1999) of WASP-3 using the parameters from Pollacco et al. (2008). (M_*=1.24 $M_\odot$, R_*=1.31 $R_\odot$, T_{eff}=6400 K, and log g= 4.25). We plot the Ks transmission curves inverted at arbitrary scale at the top of both panels (dotted black lines).

no heat redistribution, and full reradiation at the substellar point ($f=\frac{2}{3}$), underpredicts the observed emission in this band. If our best-fit reradiation factor, f_{Ks}, is similar to the total reradiation factor for this planet, than WASP-3b must have a Bond albedo near zero.

The most likely explanation for the very bright emission is that our Ks-band observations are probing a deep atmospheric layer through holes in the water opacity; this layer likely both poorly redistributes heat to the nightside, and is uniformly hotter than expected from simple arguments. An alternative explanation for the inefficient redistribution we observe could be a broad emission feature on top of thermal emission from an atmosphere that redistributes heat inefficiently, such as dayside only emission ($f=\frac{1}{2}$). Such an emission feature would have to be very broad given the relatively broad Ks-bandpass we use for our observations and thus we favour the former explanation.

We also compare the depth of our joint analysis of our Ks-band eclipses to a series of planetary atmosphere models in Figure 6.7. Unfortunately for our understanding of the energy budget and atmospheric dynamics and radiative transfer of this planet's atmosphere, our Ks-band eclipse detections are the first detections of thermal emission of this planet. We thus lack multi-wavelength constraints, and our understanding of this planet's atmosphere is limited to a single atmospheric depth and pressure. We first plot a series of blackbody models featuring isotropic reradiation ($f=\frac{1}{4}$; blue dotted line; $T_{eq}\sim1984$ K), emission from the dayside only ($f=\frac{1}{2}$; red solid line; $T_{eq}\sim2359$ K), and a model with highly peaked reradiation right at the substellar point ($f=\frac{3}{4}$; grey dotted line; $T_{eq}\sim2611$ K). Although, it adds a level of complexity that likely is not necessary with only one thermal emission measurement, we also compare our measurement to a series of one-dimensional, radiative transfer, spectral models (Fortney et al., 2005, 2006, 2008) with different reradiation factors that specifically include or exclude gaseous TiO/VO into the chemical equilibrium and opacity calculations. In these models when TiO/VO are present in gaseous form in the upper atmosphere they act as absorbers at high altitudes and lead to hot stratospheres and temperature inversions (Hubeny et al., 2003). We present models with no heat redistribution ($f=0.67$), with and without TiO/VO and note that these models underpredict the observed emission. We note that the models with and without a temperature inversion and a hot stratosphere are similar in the Ks-band, as this wavelength is still longwards of the blackbody peak of this planet. Thus our observations are unable to provide constraints on whether the planet does or does not harbour a temperature inversion.

It will be intriguing to combine our Ks-band observations with thermal emission measurements at other wavelengths. We plan to shortly reobserve this planet in the J & H near-infrared bands in order to detect its thermal emission, as we have recently done for the very highly irradiated hot Jupiter WASP-12b (Croll et al., 2011). Also, WASP-3 has already been observed with Spitzer in each of the IRAC bands (PI Wheatley), and follow-up observations have been

performed during the warm Spitzer mission (PI Knutson). Spitzer/IRAC observations will also shed light on whether this planet does or does not seem to have a temperature inversion. Also, it will be interesting to note whether the planet redistributes heat inefficiently throughout its atmosphere as probed by multiwavelength observations, or whether this extremely inefficient redistribution of heat we observe occurs only at the atmospheric depth we probe with our Ks-band observations.

6.5.2 Comparison of near-infrared detection of the thermal emission of hot Jupiters to date

There have been a wealth of recent detections from the ground of the thermal emission of hot Jupiters in the near-infrared. Detections with greater than 3σ confidence include[4]: TrES-3b in Ks-band (de Mooij & Snellen, 2009; Croll et al., 2010b), OGLE-TR-56b in z'-band (Sing & Lopez-Morales, 2009), WASP-12b in z'-band (Lopez-Morales et al., 2010) and in J, H & Ks (Croll et al., 2011), CoRoT-1b at $\sim$2.1 μm (Gillon et al., 2009) and in Ks (Rogers et al., 2009), TrES-2 in Ks (Croll et al., 2010a), WASP-19 in H (Anderson et al., 2010) and Ks (Gibson et al., 2010), HAT-P-1 in Ks (de Mooij et al., 2011), as well as our own WASP-3 detection in Ks-band reported here. Given this recent flurry of detections it is high-time to search for possible trends revealed by these observations.

One such possible correlation is between the incident stellar flux and the efficiency of redistribution of heat from the day to the nightside, which we parameterize with a joint constraint on the Bond albedo and the reradiation factor of the atmospheric layer probed by that wavelength of observation, $f_i \times (1 - A_B)$. As, the geometric and Bond albedoes of many hot Jupiters have been measured (Rowe et al., 2008; Snellen et al., 2009; Alonso et al., 2009,b; Snellen et al., 2010b) or inferred to be close to zero (Cowan & Agol, 2011), this joint constraint should be in most cases largely identical to a constraint on the reradiation factor of that atmospheric layer, f_i. Fortney et al. (2008) predicted that more highly irradiated hot Jupiters would have temperature inversions and feature more inefficient redistribution of heat to their nightsides than their less highly irradiated cousins, which were predicted to lack such inversions; although, Spitzer observations have not universally supported this theory (i.e. Machalek et al. 2008; Fressin et al. 2010), it is worth investigating if at least the redistribution of heat is supported at near-infrared wavelengths. We thus plot the correlation between the inferred equilibrium

---

[4]We note that we do not include detections from space using the NICMOS instrument on the Hubble Space Telescope (of HD 189733b [Swain et al. 2009a], and HD 209458b [Swain et al. 2009b]), as the analysis of this data has recently been called into question (Gibson et al., 2011). Also, we do not include the spectroscopic detection of the dayside spectrum of HD 189733b in the near-infrared using the SPEX instrument on the NASA Infrared Telescope Facility, as some of the features in this spectrum have likely been ruled out with another data-set with high confidence (Mandell et al., 2011).
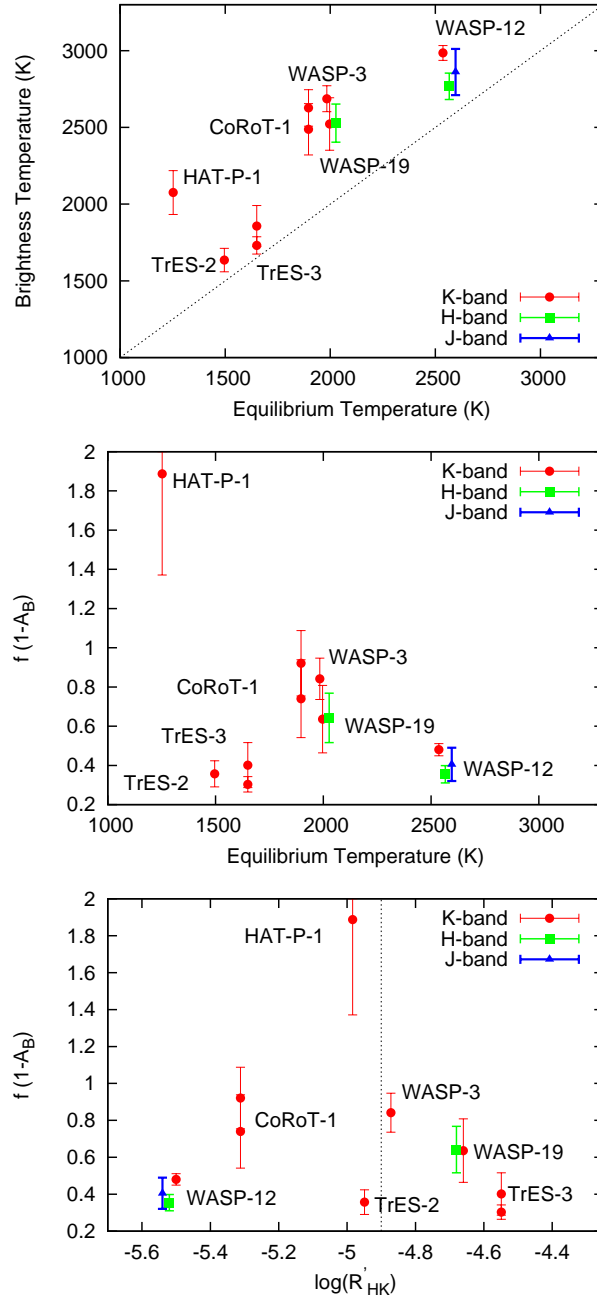
Figure 6.8 Various thermal emission detections from broadband, ground-based photometry in the JHK-bands (or at wavelengths that overlap with those filters). Top: The observed brightness temperatures compared to the equilibrium temperatures of the planets. The dashed line indicates a one-to-one correlation between brightness and equilibrium temperatures. Middle: The joint Bond albedo reradiation factors, $f_i \times (1 - A_B)$, compared to the equilibrium temperatures. Bottom: $f_i \times (1 - A_B)$ compared to the Ca II H & K activity index obtained from Knutson et al. (2010). The dotted vertical line indicates the dichotomy between hot Jupiters that Knutson et al. (2010) (and references therein) observed to have temperature inversions ($log(R'_{HK} <$-4.9; to the left of the line) and those that did not ($log(R'_{HK} >$-4.9; to the right of the line). In all plots we marginally offset the thermal emission measurements of the same planet in different near-infrared bands (JHK) along the x-axis for clarity.

temperatures of these planets, a proxy for incident stellar flux, and their observed near-infrared brightness temperatures, and joint constraints on $f_i \times (1 - A_B)$ (Figure 6.8, top and middle panel). HAT-P-1b's Ks-band thermal emission is an obvious outlier; we note that de Mooij et al. (2011) highlighted the possibility that unaccounted for systematic errors may have affected their measurement of the Ks-band thermal emission of this planet. Even ignoring, the HAT-P-1b measurement the efficiency of day-to-nightside redistribution in the atmospheric layers probed by the near-infrared does not decrease monotonically with increasing effective temperature. With still so few near-infrared thermal emission measurements it is unclear whether there is or is not a trend with increasing equilibrium temperature.

Recently, Knutson et al. (2010) suggested that there was a trend between the activity of the hot Jupiter host stars (as measured by the Ca II H & K activity index, $log[R'_{HK}]$), and the depths of the Spitzer/IRAC secondary eclipses. Specifically, Knutson et al. (2010) suggested that hot Jupiters orbiting active stars (higher $log[R'_{HK}]$ values) lacked temperature inversions, while those orbiting less active stars (lower $log[R'_{HK}]$ values) displayed signs of a temperature inversion[5]. One possible explanation for this phenomenon is that active stars should have increased UV flux, which may destroy the high altitude absorber that would otherwise cause the hot stratosphere and the temperature inversion. It is predicted that planets with and without temperature inversions, should have observable differences in the near-infrared as well; as already mentioned, planets with a hot stratosphere, should have increased thermal emission in the mid-infrared, and are therefore expected to reradiate less at shorter wavelengths in the near-infrared (Hubeny et al., 2003). We note that all those planets orbiting less active stars with ground-based near-infrared detections have been reported to have temperature inversions: CoRoT-1b (Deming et al., 2011), HAT-P-1b (Todorov et al. 2010 report a modest temperature inversion), WASP-12b (Madhusudhan et al. 2010 report a weak inversion) and TrES-2b (O'Donovan et al. 2010, although see Madhusudhan & Seager 2010). Of the sample orbiting active stars with near-infrared thermal emission detections, TrES-3b (Fressin et al., 2010) has been reported to lack an inversion as expected, while the Spitzer/IRAC eclipse depths of WASP-19b and WASP-3b have yet to be reported. However, as Figure 6.8 (bottom panel) shows there is no clear trend between more active hot Jupiter hosts and increased near-infrared thermal emission.

A greater number of near-infrared thermal emission detections of hot Jupiters, along with confirmation of the current detections, will be required to elucidate whether any of the predicted trends have been observed or can be confidently ruled out.

---

[5]Knutson et al. (2010) use the slope compared to a blackbody of the flux in the 3.6 to 4.5 μm IRAC channels as a proxy for temperature inversions or lack thereof; planets with temperature inversion generally display greater flux in the 4.5 μm channel than the 3.6 μm compared to a blackbody, while planets without temperature inversions display the opposite phenomenon.

Chapter 7

The Limits on Precise Photometry in the Near-infrared from the Ground

It is notoriously tricky to obtain accurate photometry from the ground in the near-infrared. To my knowledge we have achieved the most accurate photometry to date from the ground in the near-infrared with our ongoing program to detect the thermal emission of hot Jupiters using CFHT/WIRCam. For instance, with our observations of TrES-2 (Chapter 2) we were able to achieve an RMS precision of $\sim 0.7 \times 10^{-3}$ on timescales of one minute; also, our photometry in this instance is relatively free of time-correlated systematics as it bins down near the Gaussian noise limit with increasing bin size. Although photometry this precise from the ground is a significant achievement, our photometry is still a factor of two to three times higher than the photon noise. Clearly there is still an unaccounted for systematic (or two or three) arising from either the instrument or the sky, that prevents us from achieving photon-limited precision. The obvious question that arises is: what is this limiting systematic?

We have noticed several unexplained systematics in our CFHT/WIRCam photometry that warrant further inspection. As we perform differential photometry with ten or more reference stars, the systematics that we observe must arise from things that affect the reference stars differentially from our target stars; possibilities include: instrumental variations from one WIRCam chip to another, or portion of a chip to another (such as one amplifier to another), or physical differences of the atmosphere that vary across the sky on a several arcminute spatial scale. In the following chapter, I discuss: the various systematics arising from both the instrument/telescope and the sky that often frustrate efforts in the near-infrared to achieve near photon-limited precision (§7.1), the systematics that we have observed in our CFHT/WIRCam

photometry and I speculate as to their possible origins (§7.2), and finally I present possible avenues forward to address these issues in the hopes that we may achieve near-photon limited precision in the near-infrared in the future (§7.3).

7.1 Systematics that hinder near-infrared precision

There are a variety of systematics that frustrate attempts to achieve precise near-infrared photometry; these systematics include strong molecular absorption (water, and carbon dioxide being too prominent examples), Rayleigh scattering and aerosol scattering that play a particularly important role in J-band, and sky background variations. Sky background variations arise from both variability in airglow emission, which is particularly pernicious in H-band, and thermal background variations that play an increasingly important role at longer wavelengths and thus dominant by Ks-band.

Water vapour is the dominant opacity source across wide swaths of the near-infrared; as a result many of the infrared bands that we know and love (JHKLM etc.) fall within water opacity windows. Atmospheric water vapour varies considerably from night to night and also seasonally; the effects of extinction arising from water opacity are generally reduced in winter when the temperature is low and the atmosphere is typically able to hold less water (Glass, 1999). Although water vapour variations have been reported to play a large role in variations in the extinction in J-band, and to a lesser extent in H-band, they are thought to play an insignificant role by Ks-band and at longer wavelengths (Lombardi et al., 2011). At the sub-millimagnitude level it is less clear if precipitable water variations play a role in limiting the photometric precision we reach with CFHT/WIRCam, as it is unclear if this water vapour variability causes differential extinction between our target star and our reference stars separated by only a few arcminutes on the sky. Humidity should be a useful proxy for the water vapour column density, and there are no obvious correlations between humidity and our photometric precision (see Table 7.1).

Rayleigh scattering from air molecules, and scattering from aerosols in the atmosphere also play a role in contributing to near-infrared extinction (Glass, 1999). However, aerosol scattering is generally negligible at wavelengths greater than 1 μm. Rayleigh scattering from air molecules is the dominant source of extinction in J-band, but is insignificant as one moves to longer wavelengths (Lombardi et al., 2011).

Molecular absorption plays a prominent role in the variability of extinction across the near-infrared spectrum. Lombardi et al. (2011) applied a radiative transfer code that indicated that molecular absorption plays the dominant role in both the H and Ks-bands; in H-band the dominant absorber is water, while in Ks-band the dominant absorber is carbon-dioxide,

followed by methane (Lombardi et al., 2011).

Airglow, radiated by excited levels of the hydroxyl radical OH-, is a prominent source of background variability; in H-band it is the dominant source, while its effects are reduced in both J and Ks (Glass, 1999). Airglow observations may be of particular interest to individuals performing differential photometry, as the timescales and angular scales of airglow variability may induce systematics into one's differential photometry. Airglow varies on large and small angular scales as well as long and short timescales. It is known to vary on 5-15 minute timescales (Moreels et al., 2008), as well as day-long timescales due to diurnal variations in temperature; it varies across the sky, as well as due to the passage of gravity waves in the ionosphere (Glass, 1999; Ellis & Bland-Hawthorn, 2008). Gravity waves may be of particular interest to observers utilizing CFHT/WIRCam or other wide-field infrared imagers, as they create variations on small enough spatial scales (a few arcminutes) that it is conceivable that they could cause differential variability from one's reference stars to one's target star.

Attempts to devise a filter to avoid these sharp airglow lines, has thus far not proved feasible (Herbst et al., 1994; Jones et al., 1996). Rugate filters, which are designed to block out many of the most pernicious OH lines by laying a thin dielectric of varying composition, were predicted to show particular promise in J-band (Offer & Bland-Hawthorn, 1998); however such filters have proved difficult to manufacture (Ellis & Bland-Hawthorn, 2008). A fibre Briggs grating[1], which should suppress OH lines while maintaining high throughput between these lines, may be a better solution (Ellis & Bland-Hawthorn, 2008). Conceivably, constructing specialized filters to avoid these OH lines, or the molecular absorption lines that plague that JHK bands may significantly improve our photometric precision. We discuss this possibility in §7.3.

The dominant background source in Ks-band and at longer wavelengths is the thermal background. These variations arise from the blackbodies of the sky, and often the telescope/instrument or other objects within the dome. Typically by approximately 2.3 μm the thermal background begins to dominate over all other sources of noise (Glass, 1999). Obviously, cooler environments, such as those afforded by the High Arctic (Steinbring et al., 2010) and Antarctica, reduce the importance of this background until one reaches even longer wavelengths (up to 2.4 μm and out of the K-band altogether for Antarctic winter environments; Ellis & Bland-Hawthorn 2008).

---

[1]Fibre Briggs gratings are composed of optical fibres where the core has a slowly varying refractive index. By precisely controlling this variation, strong Fresnel reflections at specific wavelengths effectively block this light, while allowing high throughput elsewhere.

7.2 Systematics in our CFHT/WIRCam photometry

We discuss here three systematics of unknown origin that seem to limit the precision we are able to reach with our CFHT/WIRCam photometry.

7.2.1 Differential Electronic Response

In the 2008B semester we observed the secondary eclipses of the hot Jupiters WASP-3b, and XO-3b. We did not observe these targets using "Staring Mode" (Devost et al., 2010); instead we placed the target star in one of the WIRCam guide windows, and placed three specifically chosen reference stars in the other guide windows on the adjacent WIRCam chips. For an unexplained reason, we did not reach the precision we expected, but instead observed large 2% variations in the target star flux, after correcting with the three other reference stars, over the 4-hour duration of the secondary eclipse and baseline. Given the precision we have since demonstrated with "Staring Mode," the most straight-forward explanation for the poor precision we achieve with this guide-cube technique is a differential electronic response from guide window to guide window. This response may play a role in our "Staring Mode" observations as well; for some of our data-sets there appears to be an abundance of the most useful reference stars on the same chip as the target star (i.e. Figure 2.3 for our TrES-2b observations). However, this overabundance of suitable reference stars on the same chip could arise from instrumental variations, or due to atmospheric variations. Also, other "Staring Mode" observations show no such overabundance on the same chip, and thus it is unclear what role, if any, any sort of differential electronic response plays in limiting our "Staring Mode" observations. We note that the Gillon et al. (2009) and Gibson et al. (2010) observations using the HAWK-I instrument on the VLT (which also features HAWAII-2RG detectors), also find that the best reference stars are on the same chip as their target star; thus, it seems safe to conclude that this differential electronic response, instrumental variation or atmospheric effect leading to this tendency to find suitable reference stars on the same chip as the target, is not unique to CFHT/WIRCam.

7.2.2 Background trends

For many of our CFHT/WIRCam data-sets we observe linear or quadratic trends in our differential photometry over the duration of the observations. We cannot rule out that these trends are intrinsic to the star themselves, such as trends that could arise from rotational modulation or due to another source of astrophysical variability; however, given the frequency with which we observe these trends we believe them to be instrumental in nature. Examples of these background trends can be seen in Figures 2.7, 3.4, 4.3, 4.4, 4.5, 5.2 and 6.3. As these trends occur after correcting the flux of our target with our various reference stars, it is likely

that these trends arise from a systematic that is affecting our target star differentially than our reference stars. Unfortunately, the possible explanations for this systematic are numerous, as it could be instrumental in nature or due to atmospheric effects. Instrumental possibilities include chip to chip, or amplifier to amplifier variations of the WIRCam array. We also observe small variations in the x and y centroid of the PSF in our photometry over the duration of our observations; as a result, the variability we observe could be due to inter- or intra-pixel sensitivity, or due to centroiding inaccuracies during our aperture photometry. Any sort of atmospheric variability due to extinction, airglow or thermal background variations that affect our target stars differentially than our reference stars are another possibility. We note that the Gibson et al. (2010) VLT/HAWK-I photometry shows an obvious background trend[2], but other ground-based, near-infrared secondary eclipse detections do not show strong background trends. These background trends seem to be unique to our instrumental setup[3].

Tests have been performed to determine how these background trends varied when only reference stars on the same chip as the target were used; the results were inconclusive, as there was no clear pattern that was consistent from data-set to data-set. Further tests are in the midst of being performed to test how these background trends vary when only reference stars with the following properties are used: of similar colours, on the same amplifier, or close in angular separation to the target star.

7.2.3 Variable photometric precision

We have observed that data taken on one night can be considerably worse or better than data taken on another night; this is true even for observations of the exact same target obtained on two different occasions that is reduced in a similar manner (Figure 7.1). The reason for this discrepancy is unknown, but presumably is due to atmospheric effects, although instrumental trends cannot be ruled out. We have presented the out-of-eclipse photometric precision from a number of our observations in Table 7.1, along with other atmospheric data. There are no obvious correlations between the photometric precision we are able to reach in Ks-band and the atmospheric and instrumental variables we present here. Further study is clearly required to determine the variable that leads to reduced photometric precision on one night compared to another.

---

[2]Gibson et al. (2010) speculate that the source of their background trend is due to the fact that PSFs of the target and reference stars seemed to gradually increase during their observations; presumably this effect would have to affect the target star more than the reference stars to display the downward trend in flux in their differential photometry.

[3]As we use many more reference stars than other observers, the fact that the background trends are unique to our photometry does not wholly rule out the possibility that these trends arise from atmospheric effects.
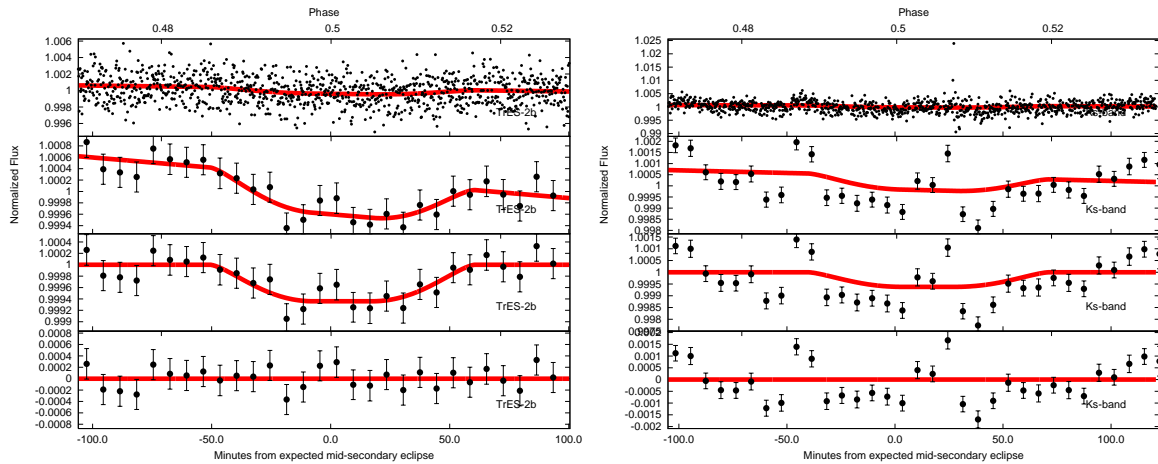
Figure 7.1 CFHT/WIRCam Ks-band photometry of the secondary eclipse of TrES-2b obtained on 2009 June 10 (left) and 2010 July 4 (right). In the left panel the red line displays the best-fit secondary eclipse model with its associated background trend; in the right panel we fit for the background trend, but we fix the depth of the secondary eclipse at the value observed in 2009 (left panel). Note the different vertical scales in the two panels. The format is otherwise identical to Figure 2.7. Obviously, the photometric precision is superior in the 2009 photometry (left panel).

Table 7.1. Photometric Precision of CFHT/WIRCam data-sets

Target	Date[a]	K Magnitude	Photometric precision (RMS $\times 10^{-3}$)	Mean Humidity (%)	Weather Tower Temperature (^{o}C)	Cage Temperature[b] (^{o}C)	WIRCam chip #[c]
TrES-2	2009 June 10/11	9.85	0.748	37	3.1	6.2	2
TrES-2	2010 July 3/4	9.85	0.966	14	5.2	8.2	1
TrES-3	2009 June 2/3	10.61	1.603	36	1.6	4.9	1
WASP-2	2010 July 4/5	9.63	1.238	13	5.2	7.8	1
WASP-3	2009 June 3/4	9.36	0.929	25	0.8	4.1	2
WASP-3	2009 June 14/15	9.36	1.353	37	2.7	5.4	2
WASP-12	2009 December 28/29	10.19	0.854	8	2.9	5.5	1
WASP-12	2011 January 14/15	10.19	1.340	54	-0.7	0.4	1
WASP-12[d]	2011 January 20/21	10.19	1.553	43	-0.7	3.2	1

[a]All dates in Hawaiian Standard Time.

[b]The Cage Temperature is the temperature just outside the Prime Focus cage of the telescope, and is thus a good indicator of the temperature of the air that the telescope will be staring through during our observations.

[c]This column denotes the WIRCam chip that the target star fell on. Chip 2 displays more significant persistence than chip 1.

[d]These data were of the transit of WASP-12b, rather than the secondary eclipse.

7.3 Possible avenues to achieve even more accurate photometry

Without properly identifying the limiting systematic or systematics that are preventing us from reaching even higher photometric precision, it is difficult to identify obvious avenues forward. A few possibilities include reducing thermal background sources in the dome, improving the guiding and exploring alternative filters to avoid emission and absorption lines.

For our Ks-band photometry in particular, thermal background variations are one likely source of the limiting systematic that prevents us from reaching high precision. A number of heat sources have recently been identified in the CFHT dome, that may actually contribute significantly to the thermal background (Kevin Ho, personal communication). Relatively low-cost changes could be implemented to insulate these heat sources, or eliminate the electronic inefficiencies causing this thermal noise. It will be interesting to compare the precision we reach from before to after these changes are hopefully made.

Our H-band observations of WASP-12b (Chapter 4) mistakenly used micro-dithering. Although we have not extensively tested the photometric precision that we are able to reach in H-band yet, it appeared that the micro-dithering decreased our photometric precision. One possible explanation for this decreased precision is inter- or intra-pixel sensitivity variations. In our normal "Staring Mode" observations we also observe small variations in the x and y centroid of the target and reference PSFs (Figure 2.1). Thus it is conceivable that improvements to the guiding, may also improve our photometric precision. The current "Staring Mode" guiding strategy involves picking four guide windows on each WIRCam chip, and creating a combined PSF that assigns equal weight to each guide window, and then correcting for variations from this combined PSF. As opposed to other wide-field WIRCam observations, our photometric observations should place more emphasis on guiding in the vicinity of our target star. Thus, a revised guiding scheme could provide superior precision. One such scheme would be to ensure that the guider picks a guide window relatively nearby to that of our target star, and that this revised guiding procedure assigns extra weight to the guide window on the same chip as our target. However, our TrES-3 Ks-band observations (Chapter 3) featured large shifts (up to ten pixels) in the x and y centroid of the PSF; we were nonetheless able to reach impressive precision and an 8σ detection of its thermal emission. Therefore, variations induced by intra- or inter-pixel sensitivity may be already well accounted for by the flat-field, and our defocus, and may thus be negligible. Indeed, the intra-pixel response of HAWAII-2RG detectors appears to be smooth (Hardy et al., 2008).

If the limiting systematic is due to absorption or emission at a specific wavelength or wavelengths one could imagine constructing a new filter to suppress these wavelengths. Medium-band filters may prove particularly promising. For instance, if variability due to either molec-

ular absorption or airglow emission at specific wavelengths limits our photometric precision, one could imagine constructing a Rugate filter or a fibre Briggs grating to suppress specific absorption or emission lines while still providing high throughput at adjacent wavelengths and for the rest of the filter. Narrow band filters, however, may be of limited use. We've already attempted to observe with narrow band filters on several occasions; these observations were of brighter stars (K_{mag}~7-8) and did not reach sufficient precision. For these brighter targets when the target star is properly illuminated, in general there are not a sufficient number of properly illuminated reference stars to perform differential photometry at the level necessary to achieve detections of the thermal emission of hot Jupiters. Repeating these narrow band observations on a fainter target with a higher defocus and a longer exposure time, such that our target and reference stars are properly illuminated, without approaching saturation, may be an avenue to explore. Nonetheless, medium-band filters that are specifically constructed to avoid the most pernicious telluric lines, are still a promising avenue for progress; they should provide sufficient through-put to properly expose both our target and reference stars, and they could be constructed such that they avoid lines of airglow emission or molecular absorption that limit our photometric precision.

We conclude that these are just the most obvious avenues that warrant exploration that may significantly improve our near-infrared photometric precision.

Chapter 8

The hot Jupiter Kozai Mechanism Connection Constrained with Radial Velocity data

8.1 Abstract

We have performed a systematic analysis to search for long-term trends in the radial velocity residuals of more than ~100 exoplanetary hosts from the California & Carnegie Planet Search team to constrain the role that the Kozai mechanism plays in migrating hot Jupiters inwards and halting these exoplanets at the ~3-4 d periods where they are seen to pile-up. These long-term linear trends are likely indicative of outer stellar or substellar companions (P ~ 30 - 5000 yr); if originally inclined from the known planet by 40° - 140° these companions could have induced the known exoplanet to migrate to its present position via the Kozai mechanism with tidal heating. We find that the frequency of long-term linear trends in the radial velocity residuals are comparable in the hot Jupiter sample and the rest of the exoplanetary sample, thus providing no evidence in favour of the theory that suggests that hot Jupiters migrate to their present positions as a result of the Kozai mechanism with tidal heating. These results constrain the claim of Triaud and collaborators that many if not nearly all hot Jupiters migrated via the Kozai mechanism rather than via other migration mechanisms.

8.2 Introduction

The discovery of the first exoplanet around a Sun-like star (51 Peg b; Mayor & Queloz 1995) was simply the first in an ever-expanding list of surprises in the field of extrasolar planets. This was because this planet - rather than being the Jupiter analog that planetary theorists had

116

expected - was a hot Jupiter: a Jupiter-mass planet orbiting a mere few stellar radii away from its parent star. Ever since the seminal discoveries of these first few hot Jupiter exoplanets, the question of how these planets formed, migrated inwards, and were then halted at their present positions have been subjects of ongoing interest, and debate.

Hot Jupiters are believed to have formed, not where they are currently found, but out at several AU beyond the snow line (Bodenheimer et al., 2000), requiring a migration mechanism to bring them to their present distances. The traditional type-I (Goldreich & Tremaine, 1980; Ward et al., 1986), and type-II (Papaloizou & Lin, 1984; Lin et al., 1996) migration mechanisms migrate the gaseous planet inwards by trading angular momentum with the protoplanetary disk that the planet is either embedded within (type-I), or within which it has opened a gap (type-II). These migration mechanisms leave unanswered the question of how these planets halted their inward plunge at a few stellar radii away from their stars. An additional twist in the story, is the so-called hot-Jupiter "pile-up", a statistically significant excess of planets found with ~3-4 d periods even after observational biases are taken into account (Gaudi et al. 2006; Butler et al. 2006; Cumming et al. 2008; although see Howard et al. 2011 for recent results from the Kepler mission). Thus, any method that seeks to explain how the inward migration of these massive exoplanets are halted, must also explain why they are preferentially halted at this specific distance from their stars. Possibilities that have been invoked to explain this discrepancy include tidal interactions with the spin of the star (Trilling et al., 1998), the evaporation of the inner disk from stellar irradiation (Baraffe et al., 2005), or the clearing of the inner protoplanetary disk by the stellar magnetosphere (Lin et al., 1996).

One such theory to explain both the inward migration and halting of these hot exoplanets at the ~3-4 d periods where they are found, has come to be known as the Kozai mechanism with tidal friction (Wu et al., 2007; Fabrycky & Tremaine, 2007). The first part of the story invokes the Kozai mechanism; the Kozai mechanism was first proposed by Kozai (1962) in the context of asteroids gravitationally influenced by Jupiter and independently by Lidov (1962) in the context of satellites of the Earth perturbed by the Sun and the moon. Through this mechanism a planet orbiting one member of a binary system, where the companion is highly inclined compared to the plane of the exoplanetary system, will experience large cyclical variations in its eccentricity, and inclination angle, by trading angular momentum with the outer companion (Harrington, 1968; Holman et al., 1997; Innanen et al., 1997; Wu & Murray, 2003). The second part of the story is tidal heating. During periods of high eccentricity, orbital energy is lost near periastron due to tidal heating of the planet. The planet eventually stalls when eccentricity forcing from the distant outer companion is counteracted by eccentricity damping from tidal dissipation from the primary. The result is that for a wide range of stellar masses, companion masses, and initial orbital configurations of the planet, the planet stalls at a radius corresponding to a ~3-4

d orbital period (Wu et al., 2007). The Kozai mechanism with tidal friction thus predicts that one would expect a greater frequency of outer stellar or substellar companions in hot Jupiter systems compared to the rest of the exoplanetary sample; in addition, hot Jupiters that have migrated via this mechanism should experience significant misalignment between the the orbit normal of the planet and the stellar spin axis (Fabrycky & Tremaine, 2007; Wu et al., 2007).

The Rossiter-McLaughlin effect (Rossiter, 1924; McLaughlin, 1924; Gaudi et al., 2006) allows researchers to measure the sky-projected angle, λ, between the stellar rotation axes and the orbital normal of the planet for transiting hot Jupiters. Most of the first exoplanetary systems for which λ was measured were consistent with zero suggesting that most, but not all, hot Jupiters migrated via mechanisms that led to spin-orbit alignment, rather than misalignment (Fabrycky & Winn, 2009). Combined with the fact that a comparison of exoplanetary host systems with and without stellar companions showed no excess of such companions for hot Jupiter systems versus the rest of the exoplanetary systems (Fabrycky & Tremaine, 2007), made it seem unlikely that the majority of hot Jupiters migrated to their present positions via the Kozai mechanism.

The Rossiter-McLaughlin effect has since been used to measure λ for a flurry of new systems and a number of these have been misaligned (Triaud et al. , 2010). Based on the fact that the then current λ distribution for hot Jupiters was consistent with what one would expect if hot Jupiters migrated solely via the Kozai mechanism, Triaud et al. (2010) thus suggested that many if not all hot Jupiters may have migrated via this very mechanism. A more recent work by Morton & Johnson (2011) suggests that the ensemble of hot Jupiter Rossiter-McLaughlin measurements to date strongly favour a two-mode migration scenario, combining a mode that preserves alignment (such as disk migration) and a migration mechanism that causes misalignment (Kozai being one possibility); in fact, of the two mechanisms that Morton & Johnson (2011) examine that may cause misalignment, the authors find that the expected λ distribution from planet-planet scattering with tidal friction (Nagasawa et al., 2008) is a better fit to the observed Rossiter-McLaughlin measurements than that of Kozai. With these various and sometimes conflicting constraints on the connection between hot Jupiters and Kozai migration, it is high time to present an updated analysis that determines what fraction of hot Jupiters likely migrated to their present position via the Kozai mechanism with tidal heating, by synthesizing all the evidence including Rossiter-McLaughlin measurements, Direct Imaging statistics and from the presence or lack thereof of long-term RV trends that we discuss below.

Here, we search for observational evidence in support of the theory that hot Jupiters have resulted from the Kozai mechanism with tidal heating in the radial-velocity data-sets of the California & Carnegie Planet Search group (§8.3.1). We search for long-term linear trends in the radial velocity (RV) residuals that are likely indicative of a (usually undiscovered) stellar or

substellar companion; the methods that we apply to perform this task are discussed in §8.3.2. In §8.4 we perform Monte Carlo tests to determine the parameter space of outer companion mass and orbital period that we would be able to detect using this data-set and our methods. In §8.5 we compare the frequency of long-term linear radial-velocity trends in the hot Jupiter sample versus the rest of the exoplanetary sample, and correct for biases as revealed from the Monte Carlo tests. We find that the binary frequency detected in our two samples are statistically identical, and thus we do not find evidence in favour of the theory that a significant fraction of hot Jupiters migrated and were halted at the present positions via the Kozai mechanism with tidal heating. We compare our results to the current ensemble of Rossiter-McLaughlin measurements for hot Jupiters, and statistics on the frequency of directly imaged stellar companions in hot Jupiter systems and the rest of the exoplanet sample in §8.6. We lastly discuss the combined constraints from these three methods and the implications this has on the fraction of hot Jupiters that may have migrated via the Kozai mechanism in §8.7.

8.3   Data & Methods

8.3.1   California & Carnegie Radial Velocity Data

We use an updated radial-velocity data-set provided by the California & Carnegie Planet Search group (Butler et al., 1996) The California & Carnegie Planet Search group has been observing sun-like stars for evidence of RV signatures of extrasolar planets and binary companions since the early 1990s. For over a decade from 1997 onwards this group continuously monitored over ∼1000 of the brightest and closest FGKM dwarfs. The telescopes that were used to observe these stars were the Keck, Lick, and Anglo-Australian Telescope (Marcy et al., 2005), using the HIRES, Hamilton, and UCLES instruments, respectively. The sample that we employ here includes RV data from ∼105 exoplanetary host stars mostly in single exoplanetary systems, with median values of ∼77 RV data points per star over a duration of ∼7.2 years. Our sample from the California & Carnegie group includes observations up to 2007 July.

8.3.2   Methods

In the context of this work we search for long-term linear trends in the RV residuals to the best-fit Keplerian orbit of the data of the California & Carnegie Planet Search group; these trends are indicative of stellar or substellar outer companions in these systems. As the orbital periods of these outer companions are much longer than the duration of the RV observations, the trends are therefore explicitly minor deviations to the best-fit Keplerian orbit. Thus, we employ the best-fit Keplerian orbital parameters from the Catalog of Nearby Exoplanets (CNE;

Butler et al. 2006) as an initial guess for our fitting process. Also, as we are not specifically searching for new exoplanets here we also restrict the number of planets in our fitting process searches to the number of exoplanets reported in the CNE.

We fit the RV data for the best-fit Keplerian orbital solution in addition to a linear trend for all our candidates. Thus for each exoplanetary system with a single exoplanet we fit for seven parameters - five related to the exoplanet: P (the orbital period), K (the velocity semiamplitude), T_p (the time of perisatron), e (the eccentricity), and ω (the argument of periastron), and two parameters related to the presumed outer companion: A (the slope of the RV trend) and B (the velocity offset of the trend). We employ Markov Chain Monte Carlo (MCMC; Ford 2005; Croll 2006) fitting. Flat priors in all parameters are used. We employed 10000 step MCMC chains in our fitting process; extensive numerical tests indicated that a MCMC chain of this length starting from the known parameters listed in the CNE was sufficient to reach the χ^2 minimum.

To determine if the long-term linear trend is statistically significant or not we use the False-Alarm probability (FAP) analysis as described by Marcy et al. (2005) and for our purposes in Wright et al. (2007). The Wright et al. (2007) FAP method compares the hypothesis that the data is best described by a Keplerian orbit and a long-term linear trend to the null-hypothesis that the data is suitably described by a Keplerian orbit and noise; it attempts to prove the null-hypothesis, that the linear-trend is not statistically significant, by testing if by randomly scrambling the residuals from the best-fit Keplerian orbit (without the linear trend) one can produce a linear-trend with as low as χ^2 as the original iteration. The first step in this FAP process is to fit for the best-fit Keplerian-orbit and linear-trend to the given RV data, while recording the associated χ^2: χ^2_{trend}. The residuals to the best-fit Keplerian orbit (not including the linear trend) are then randomly scrambled (completely interchanged for one another), and are then added to the best-fit Keplerian orbital solution. If there was a significant linear-trend it should then have been completely scrambled and will now appear as noise. The fitting process is then repeated with this modified data to determine the best-fit Keplerian orbital solution and linear-trend of the ith iteration: $\chi^2_{i\_trend}$. If the χ^2 has improved ($\chi^2_{i\_trend} < \chi^2_{trend}$) than this reaffirms the null-hypothesis, and thus suggests the linear-trend is not significant. This latter case counts as a false alarm. On the other hand, if the χ^2 of the ith iteration has increased ($\chi^2_{i\_trend} > \chi^2_{trend}$) then this rules against the null-hypothesis, and indicates that the data is best described with the inclusion of the linear-trend. We perform 400 iterations, and only classify linear-trends as significant when their FAPs are less than or equal to 1%.

8.4   Monte Carlo tests

To determine the types of outer companions our data and techniques are sensitive to, we performed Monte Carlo simulations on each of the target stars investigated in our sample. For each of the target stars we calculated the Keplerian RV signature of outer companions with varying orbital periods and minimum masses (P_{outer} and $m_{outer}\sin i$, respectively); the original RV data was then modified by adding these RV signals to the existing data. We then submitted these modified data to the same analysis methods described in §8.3.2.

We inserted outer companions with periods between 30 and 5000 yr. The minimum masses of the outer companions increased with increasing orbital period so that we efficiently explored the P_{outer}-$m_{outer}\sin i$ parameter space of interest. The minimum masses of the outer companion that were inserted were between 0.005 - 0.25 $M_{\odot}$ at the minimum period (30 yr) of the outer companion, and between 0.01 - 0.45 $M_{\odot}$ for the maximum period (5000 yr) of this companion; between these minimum and maximum orbital period extremes the minimum mass increased linearly in logarithmic period space. We inserted companions of varying orbital periods and minimum masses in a 6×6 grid between these maximum and minimum outer companion period and mass values. 36 different minimum mass and orbital period combinations were thus inserted for each star in our sample.

The minimum period in our grid space was chosen so that any companion with this period would result in the RV residuals having significant curvature; the maximum period was chosen such that it was long enough that we would be unable to reliably detect the RV signal as a long-term linear-trend for all but the most massive outer companions. The minimum outer companion mass in our grid space was chosen so that such a small mass companion would escape detection for all but the shortest periods; the maximum mass was chosen to be a star massive enough (spectral type earlier than K) that it would have likely been detectable with even the most cursory Adaptive Optics imaging.

The phase compared to the time of periastron and the argument of periastron for the outer companion were inserted drawing from uniform random distributions between 0-360°. The eccentricity for the outer companion was drawn from a random distribution between 0.0 and 0.6. The choice of this eccentricity distributed was arbitrary; modest changes in this eccentricity distribution should not significantly bias our results. A minimum of 10 iterations with random values of the eccentricity, and phase of the outer companion were generated at each minimum mass-orbital period grid point; we thus analyzed in excess of ∼360 iterations for each star in our sample. Excess of ∼45000 total long-term linear trends were searched for and submitted to the analysis process detailed in §8.3.2.

For the Monte Carlo analysis an extra analysis step was added for those stars that already

displayed a significant RV trend. This step was to remove the existing best-fit long-term linear RV trend prior to the reinsertion of a different linear-trend so as to determine the sensitivity of the data-set to outer companions for the Monte Carlo iterations. This process is necessary as it should allow for accurate comparisons between the systems with and without significant RV trends as long as the long-term trends are approximately linear. There was only one case - in the known binary system γ Cep with a non-hot Jupiter exoplanet [$P \sim 900$ d] - where the long-term trend displayed noticeable curvature in the long-term residuals in our sample for single exoplanetary systems. The effect of the inadequate removal of this curvature prior to the Monte Carlo analysis for this one target should only minimally bias the below Monte Carlo results.

To determine the sensitivity of the California & Carnegie data and our methods to outer companions we compare the frequency that Monte Carlo iterations of the outer companion were reliably detected in both the hot Jupiter and the rest of the exoplanetary sample. For the sake of this analysis we define hot Jupiters as those planets with periods less than 10 days ($P < 10$ d). We do not set a formal mass limit for "Jupiters," but note that the most massive planet in our sample has a mass of 11 M_J; our sample also includes seven planets with masses less than 0.3 M_J and thus planets with masses that would be better classified as "Saturns" (and even one "Neptune").

In the hot Jupiter sample we recovered 43.8% of the total Monte Carlo iterations inserted (η_{HJ}=43.8%), compared to 53.7% in the rest of the exoplanetary sample (η_{Rest}=53.7%). This number allows us to estimate the approximate fraction of long-term linear trends that would be detectable in our data for our two samples. A representative figure comparing our ability to detect outer companions in the hot Jupiter sample versus the rest of the exoplanetary sample is shown in Figure 8.1. The reduced recovery rate for hot Jupiters versus other exoplanets appears to be due to the fact that for hot Jupiters small changes in the best-fit orbital parameters can mask the effects of the long-term linear trend - that is the FAP rises above 1% a greater fraction of the time for the hot Jupiter sample with inserted long-term RV trends.

8.5   Results

We subjected the California & Carnegie RV data to the analysis methods discussed above in §8.3.2. Our goal was to search for significant linear-trends (FAPs < 1%) in the residuals to the best-fit Keplerian orbits that would likely be indicative of stellar or substellar outer companions in these systems.

We first compare the frequency of long-term linear trends in hot Jupiter systems to the rest of the exoplanetary sample for those systems with one single exoplanet only. The reason
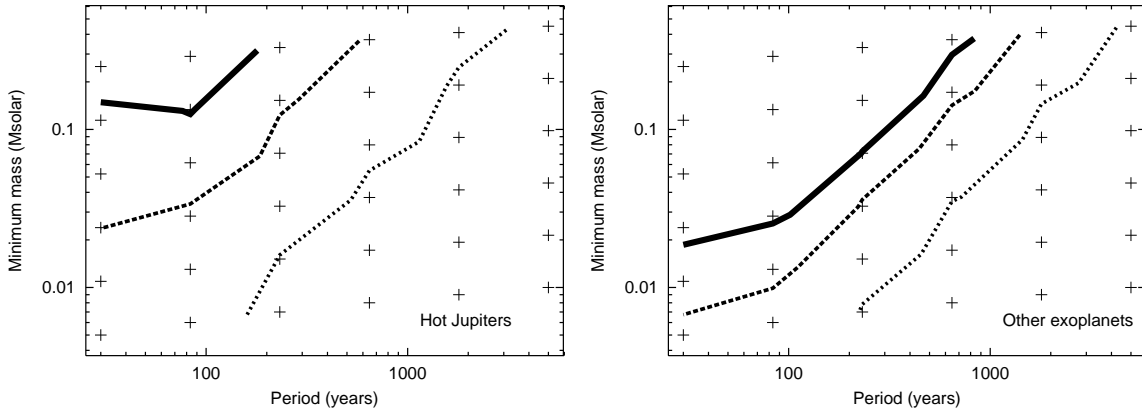
Figure 8.1 Confidence limits from our Monte Carlo simulations of detecting significant (FAP < 1%) long-term linear trends for the hot Jupiter systems (P<10d; left) and the rest of the exoplanetary sample (P>10d; right). The solid, dashed, and dotted lines denote the 80%, 68% and 33% confidence contours, respectively. The crosses indicate the periods (P_{outer}) and minimum masses ($m_{outer}\sin i$) at which the RV signatures of outer companions were inserted into the data. The fraction of the inserted trends that were detected in the hot Jupiter sample was 43.8% (left), compared to 53.7% for the rest of the exoplanetary sample (right).

multiple exoplanetary systems are not included is that the presence of other planets in these systems may serve to either inhibit the Kozai mechanism or cause planets to undergo Kozai migration when they otherwise would not. On the one hand, precession due to the other planets in the system may inhibit the Kozai mechanism as it will compete with the precession due to the outer companion that would otherwise induce the Kozai mechanism (Takeda & Rasio, 2005); alternatively excitation of a planet's inclination in a multi-planet system may cause a planet to undergo Kozai migration that originally would not have (Takeda, Kita & Rasio, 2008), because its original mutual inclination angle to that of the companion was too low (i<39.2^o).

We also, repeat our analysis with all single exoplanetary systems as well as three multiple exoplanetary systems; these three multiple exoplanetary systems are systems where the second exoplanet is a distant outer planetary companion (P > 3000 d [8.2 yr]) that may have induced the inner planet to migrate via the Kozai mechanism if the orbital planes of the two planets are misaligned. Thus in these systems, the already known outer companion causes the observed RV trend. Although one might still expect that these exoplanets were originally coaligned as they formed from a protoplanetary disk, planet-planet scattering (Rasio & Ford, 1996; Juric & Tremaine, 2008; Nagasawa et al., 2008) could have caused these planets to become mutually misaligned nonetheless, and Kozai migration with tidal circularization may have followed.

8.5.1   Frequency of Exoplanet systems with long-term linear trends

The frequencies of long-term linear trends in single exoplanetary systems in the hot Jupiter sample versus the rest of the exoplanetary sample are 5.6% (1 out of 18 systems), and 31.8% (27 out of 85 systems), respectively. For single exoplanetary systems and the aforementioned select three exoplanet systems with a distant planetary companion the frequencies are 14.3% (3 out of 21 systems) for hot Jupiters, and the same 31.8% (27 out of 85 systems), respectively. These frequencies are summarized in Table 8.1. As the frequency of trends in the hot Jupiter sample is not greater than (and is in fact significantly less than) the rest of the exoplantary sample, the frequency of long-term RV trends does not support the hypothesis that there is a connection between hot Jupiters and the Kozai mechanism.

However, this does not take into account the possible bias, illustrated above from our Monte Carlo statistics (§8.4), that we are slightly more sensitive to long-term trends in the rest of the exoplanetary sample than in our hot Jupiter sample. This small bias, however, is not enough to account for the much lower frequency of RV trends we observe in our hot Jupiter sample; to first-order even if we corrected the frequency of trends in both the hot Jupiter sample and the rest of the exoplanetary sample, the frequency of long-term trends we observe is still less for the hot Jupiters (12.7%) than in the rest of the exoplanetary sample (59.2%; see Table 8.1). However, one could imagine that the true period and mass distribution of outer companions could be very different than what we assume in our Monte Carlo statistics (§8.4). If the true distribution is very skewed from what we assume, it is possible that we could be even less sensitive to long-term trends in hot Jupiter systems than we estimate; regardless, it is unlikely to be a large enough bias to suggest that the frequency of long-term trends we observe in our hot Jupiter sample compared to the rest of the exoplanetary sample supports the connection between hot Jupiters and the Kozai mechanism with tidal heating.

We now attempt to quantify the constraint that the frequencies of long-term RV trends we observe in both our hot Jupiter and the rest of our exoplanetary sample places on the connection between hot Jupiters and Kozai migration. We first employ a Kolomogorov-Smirnov test (§8.5.1) to test if there is a discernible difference between the two samples in a direction that would support the hot Jupiter Kozai mechanism connection. We then attempt to quantify the percentage of hot Jupiters that can still arise via the Kozai mechanism in §8.5.1.

Kolomogorov-Smirnov Test

We perform a Kolomogorov-Smirnov test to determine whether our sample of exoplanets with and without long-term linear trends in the RV residuals are statistically indistinguishable. Figure 8.2 displays the cumulative probability function compared to the period of exoplanets

Table 8.1.   Fraction of exoplanetary systems displaying RV linear trends

Description	Total # of exoplanetary systems	# of hot systems with RV trends	# of other systems with RV trends
Single Exoplanetary Systems	103	1/18 (5.6%)	27/85 (31.8%)
Including two exoplanetary systems with P > 3000d	106	3/21 (14.3%)	27/85 (31.8%)
Single Exoplanetary Systems Adjusted for Monte Carlo results	103	(12.7%)	(59.2%)
Including two exoplanetary systems with P > 3000d adjusted for Monte Carlo results.	106	(32.6%)	(59.2%)

with and without long-term linear trends in their RV residuals. We present two samples in Figure 8.2; those system that contain a single exoplanet only and the other sample that contains single exoplanetary systems and the aforementioned select multiple exoplanetary sample. The largest difference in the cumulative distribution function of these two distributions for the first-sample of single exoplanetary systems is at a period of $P\sim15d$, with a Kolomogorov-Smirnov statistic of $D_n\sim0.218$. For single exoplanetary systems and the aforementioned select sample of multiple exoplanetary systems the largest difference in the cumulative distribution function is at $P\sim428d$, with a Kolomogorov-Smirnov statistic of $D_n\sim0.179$. The probabilities that the two distributions are drawn from the same distribution are 42.9% for single exoplanetary systems, and 64.8% for single plus the select multiple exoplanetary systems, respectively. The discrepancy between the two distributions in both cases is in the direction opposite to what one would expect under the Kozai mechanism with tidal heating hypothesis. That is, there is a *deficit*, rather than an *excess*, of short-period exoplanets that display long-term linear trends compared to the rest of the exoplanetary sample. Thus, we cannot provide evidence that the hot Jupiter sample is drawn from a different population than the rest of the exoplanetary sample.
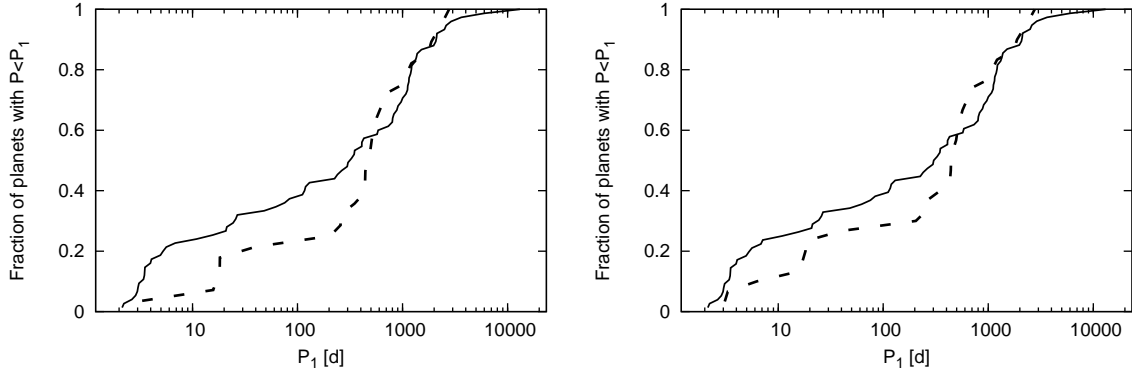
Figure 8.2 The cumulative distributions of exoplanets with long-term linear trends in the RV residuals (dashed-line) compared to those exoplanets without such trends (sold-line) for single exoplanetary systems (left) and single and the aforementioned select sample of multiple exoplanetary systems (right). In both cases, the cumulative probability is smaller at short periods (P $<$ 10 d) in those exoplanetary systems with significant long-term linear trends in the RV residuals compared to those without such trends - opposite to the prediction that there is a connection between hot Jupiters and the Kozai mechanism with tidal heating.

Monte Carlo limit on the fraction of hot Jupiters test migrated via the Kozai mechanism with tidal heating

Here we attempt to quantify with what certainty we can rule out the hypothesis that all hot Jupiters migrated to their present positions via the Kozai mechanism with tidal heating, and what percentage of hot Jupiters may still have arisen via Kozai. We start be attempting to lay out a pathway to determine the fraction of hot Jupiters that we should have detected to have long-term linear trends - which we term $f_{measure}$.

In a hot Jupiter system the long-term trends we detect will arise from a combination of the fraction of the total hot Jupiter population that have migrated via the Kozai mechanism, $f_{HJKozai}$, and those that have not, $1 - f_{HJKozai}$. That is:

$$f_{measure} = \quad (1 - f_{HJKozai}) * \eta_{HJ} * \eta_{Bias} * \eta_{Other}$$
$$+ f_{HJKozai} * \eta_{HJ} * \eta_{Kozai} \tag{8.1}$$

where η_{HJ} is the fraction of hot Jupiters systems with outer companions that we can detect to have long-term linear trends, η_{Kozai} is the fraction of Kozai systems that have an outer companion, η_{Other} is the fraction of non-Kozai systems that have an outer companion, and η_{Bias} is explained below. We may estimate that $\eta_{HJ} = 43.8\%$ presuming that these outer companions have similar mass and semi-major axis distributions as to those we assumed above for our Monte Carlo tests (§8.4). η_{Kozai} should be 100%, as the Kozai mechanism requires an

outer companion to operate. Considering that close binaries are often excluded in RV surveys, η_{Other} should be slightly less than the $\sim$65% observed frequency of binary companions from RV observations around stars whose brightest component is a G dwarf (Duquennoy & Mayor, 1991). Once we've excluded binaries with periods less than P$\sim$300 d, the period distribution of Duquennoy & Mayor (1991) suggests $\eta_{Other}\sim$46%. The last term that should be estimated is η_{Bias}, which is meant to encapsulate the fact that our long-term radial velocity trend method will be less sensitive to outer companions that do not cause the exoplanet to migrate via the Kozai mechanism than those that do. As the Kozai period scales as the square of the outer companion's period, only reasonably nearby outer companions will cause the planet to undergo Kozai migration in the age of the system. Thus, unlike outer companions that have caused the exoplanet to migrate via Kozai, binaries in other exoplanetary systems are more likely to be very wide companions that will not be detectable as a long-term RV trend. From the Monte Carlo statistics our long-term RV trend method is not sensitive to periods greater than $\sim$2500 years, and has greatly reduced sensitivity for periods greater than $\sim$1000 years. Duquennoy & Mayor (1991) suggests that approximately 30% of known binaries have periods greater than $\sim$2500 years; combining this fact with our reduced sensitivity for these long-term trends we estimate η_{Bias} as 65%. We emphasize that more quantitative estimates of the above parameters would improve the following analysis.

Using equation 8.1 we are able to estimate with what percentage confidence we are able to rule out the theory that all hot Jupiters migrated via the Kozai mechanism ($f_{HJKozai}$=1.0). First, we randomly draw 50000 samples of a distribution of 18 (the number of hot Jupiters in our sample) to see what fraction of these Monte Carlo samples display a greater frequency of trends than our 5.6% observed value just be chance for a given $f_{HJKozai}$. Under the paradigm that all hot Jupiters migrated via the Kozai mechanism ($f_{HJKozai}$=1.0), we would expect to detect η_{HJ} long-term linear trends ($\sim$43.8%). By drawing these random Monte Carlo distributions we are able to rule out the theory that all hot Jupiters result from the Kozai mechanism with tidal heating with 99.95% certainty.

With equation 8.1 and our observed frequency of long-term RV trends in the hot Jupiter sample, we are also able to place an upper limit on the fraction of hot Jupiters, $f_{HJKozai}$, that have migrated via the Kozai mechanism. By again drawing 50000 samples we are able to place a 2σ upper-limit of $f_{HJKozai}$=$\sim$36.7% on the fraction of hot Jupiters that could have migrated via the Kozai mechanism and still be consistent with the observed 1/18 frequency of long-term trends.

We note that given that our estimates of the quantities in equation 8.1 are at best educated guesses, we encourage that the above analysis should be considered illustrative, rather than definitive.

8.6   Constraints from other methods

8.6.1   Rossiter-McLaughlin measurements of hot Jupiters

Morton & Johnson (2011) has recently performed an analysis of the ensemble of Rossiter-McLaughlin measurements of the two-dimensional sky projected angle between the stellar spin and the orbit normal, λ, for hot Jupiter systems, and compared this distribution to the λ distribution expected from planet-planet scattering, Kozai migration with tidal friction, and disk migration. These authors find that if a single mechanism is responsible for migrating all planets than the λ distribution is most consistent with this mode being Kozai migration with tidal friction; however, a two-mode migration channel provides a quantitatively superior fit to the observed λ distribution, even after the extra degrees of freedom are taken into account. The authors demonstrate that these two modes are most likely one that preserves alignment (presumably disk migration), and one that does not; of the possible migration modes that do not preserve alignment, Morton & Johnson (2011) demonstrate that the observed λ ensemble is better fit by planet-planet scattering than Kozai migration. That is, a disk migration and planet-planet scattering model is favoured over a single channel Kozai migration model with 99% confidence.

8.6.2   Directly imaged companions to exoplanetary systems

Another constraint on the frequency of exoplanets that may have migrated due to the Kozai mechanism can be placed by analyzing the frequency of stellar and substellar companions to exoplanetary systems as revealed by Direct Imaging observations. Fabrycky & Tremaine (2007) presented such a comparison by analyzing the results of Raghavan et al. (2006), and showed that there were a statistically similar number, and actually fewer, short period planets in systems with multiple stars, than in single star systems - contrary to the expectation that hot Jupiters resulted from Kozai migration with tidal friction. With the much larger exoplanetary sample, and the great number of new stellar and substellar companions discovered in these exoplanetary systems from the past few years, this analysis deserves to be updated such that a firm constraint can be placed from these statistics on this theory connecting Kozai migration and hot Jupiters.

8.7   Discussion

8.7.1   Constraints from long-term RV trends

We have found a lack of observational support for the connection between the Kozai mechanism with tidal friction and the hot Jupiter pile-up by showing that the frequency of long-term linear trends in the RV residuals of the California & Carnegie Planet Search group data are not significantly greater in the hot Jupiter sample versus the rest of the exoplanetary sample. These long-term linear trends should be indicative of (usually undiscovered) outer companions in these systems that could cause the known planet to migrate and be tidally circularized via the Kozai mechanism. In the context of this work we found that the frequency of long-term linear trends in the hot Jupiter versus the rest of the exoplanetary sample was comparable - 5.6% compared to 31.8%, respectively - for single exoplanetary systems. That is, we observe fewer long-term trends in the hot Jupiter sample compared to the rest of the exoplanetary sample - the opposite to the trend one would expect if hot Jupiters migrated to their present positions via the Kozai mechanism with tidal friction.

We can furthermore weight the frequency of long-term linear trends that we observed by the percentage of outer companions that our data and methods are sensitive to, as determined from our Monte Carlo simulations. After making these corrections, our best estimate of the actual frequency of long-term linear trends, as a proxy for outer companion frequency, in the hot Jupiter versus the rest of the exoplanetary sample is 12.7%, and 59.2%, respectively. As these frequencies are comparable in single exoplanetary systems, there is no evidence that hot Jupiters and the rest of the exoplanetary sample are drawn from different distributions. The largest discrepancy between the frequency of long-term trends compared to the period of exoplanets is in the direction opposite to what one would expect if all or even most hot Jupiters migrated to their present position via the Kozai mechanism with tidal heating.

This work also allows us to place an upper-limit on the number of exoplanets that may have migrated via the Kozai mechanism with tidal heating. Based on a simple relation, and a number of assumptions that merit confirmation to ensure that they are valid, the low frequency of long-term radial velocity trends we observe in our hot Jupiter sample allows us to rule out the possibility that all hot Jupiters migrated via the Kozai mechanism with 99.95% certainty. We are also able to place a 2σ upper limit of $\sim$36.7% on the fraction of hot Jupiters that have migrated to their present positions via the Kozai mechanism. We note this upper-limit is still consistent with the theoretical prediction of Wu et al. (2007) that suggests at least 10% of hot Jupiters resulted from Kozai migration.

The results we present here inform our understanding of how the great number of hot Jupiters migrated to their present positions. Possibilities for this migration mechanism that

have been suggested in the literature include the Kozai mechanism with tidal heating (Kozai, 1962; Wu et al., 2007; Fabrycky & Tremaine, 2007), type I (Goldreich & Tremaine, 1980; Ward et al., 1986), or II migration (Papaloizou & Lin, 1984; Lin et al., 1996), planet-planet scattering (Rasio & Ford, 1996; Juric & Tremaine, 2008; Nagasawa et al., 2008), and secular chaos (Wu & Lithwick, 2010). As the RV long term trends we observe could originate from substellar objects, and even planetary size objects, the results we present here should also be useful in constraining the fraction of planets that may have experienced planet-planet scattering followed by tidal circularization, if this second planet was not ejected. For instance, it should be noted that for the three two-exoplanet systems that were included in our analysis because the outer companion had a period in excess of $\sim 8\ yr$ ($P > 3000\ d$), the innermost planet in each case was a hot Jupiter (HD 68988b, HD 187123b & HD 217107b). The innermost planet in these systems could have been migrated inwards by the Kozai mechanism if the planets originally formed at large mutual inclination angles, or could have been scattered to large mutual inclination angles by planet-planet scattering (Rasio & Ford, 1996; Juric & Tremaine, 2008; Takeda, Kita & Rasio, 2008) and then been subsequently migrated inwards by Kozai.

8.7.2 Combined constraints from Rossiter-McLaughlin measurements, directly imaged companions and long-term RV trends

Further work is encouraged to synthesize the results from these three methods (Rossiter-McLaughlin measurement, directly imaged companions and long-term RV trends), so one can place an upper limit on the fraction of hot Jupiters that have migrated to their present position via the Kozai mechanism with tidal friction.

8.7.3 Fate of the connection between hot Jupiters and the Kozai Mechanism with Tidal Heating

The fact that a large fraction of hot Jupiters do not appear to migrate to their present positions as a result of the Kozai mechanism raises the question of whether the Kozai mechnism operates in exoplanetary systems at all? The fact that the three highest eccentricity planets (all with $e>0.9$) discovered to date are all members of wide binary systems (HD 80606 [Naef et al. 2001]; HD 20782 [Jones et al. 2006; Desidera & Barbieri 2007a]; and HD 4113 [Tamuz et al. 2008]), certainly suggests the possibility that the Kozai mechanism is indeed driving exoplanets into very eccentric states. If one assumes that these three planets did reach such high eccentricity by undergoing Kozai cycles, and since such a small fraction of planets undergoing Kozai cycles will be in such high eccentricity states at any one time, then it is likely that a significant fraction of the ~ 500 currently known exoplanets are likely undergoing Kozai cycles. If this analysis was

performed in a quantitative fashion, it would be useful in helping to elucidate whether there is missing piece of the story that currently suggests that the Kozai mechanism with tidal heating should result in exoplanets being tidally circularized close to their host stars and becoming hot Jupiters via Kozai.

Bibliography

Agol, E. et al. 2010, ApJ, 721, 1861

Alonso, R. et al. 2009, A&A, 501, L23

Alonso, R. et al. 2009b, A&A, 506, 353

Andrae, R. et al. 2010, arXiv:astro-ph/1012.3754

Anderson, D.R. et al. 2010, A&A, 513, L3

Baraffe, I. et al. 2005, A&A, 436, L47

Barman, T.S. 2008, ApJ, 676, L61

Bean, J.L., Kempton, E.M.-R., Homeier, D. 2010, Nature, 468, 669

Berta, Z., et al. 2010, arXiv:astro-ph/1012.0518

Benedict, G.F. et al. 2006, AJ, 123, 2206

Beaulieu, J.P., et al. 2008, ApJ, 677, 1343

Birkmann, S.M. et al. 2010, Proc. SPIE, 7731, edited by Jacobus M. Oschmann Jr., Mark C.
    Clampin, and Howard A. MacEwen

Bodenheimer, P. et al. (2000), Icarus, 143, 2

Bodenheimer, P. et al. 2001, ApJ, 548, 466

Bodenheimer, P. et al. 2003, ApJ, 592, 555

Borucki, W. et al. 2008, in IAU Symp. 253, Transiting Planets (Cambridge: Cambridge Univ.
    Press), 289 Transiting Planets, Proceedings IAU Symposium No. IAUS253, 289

Borucki, W.J. et al. 2011, arXiv:astro-ph/1102.0541

Brown, T.M. et al. 2001, ApJ, 553, 1006

Burrows, A. et al. 2007, ApJ, 668, L171

Burrows, A. et al. 2008, ApJ, 678, 1436

Burrows, A. et al. 2008b, ApJ, 682, 1277

Butler, R. P. et al. 1996, PASP, 108, 500

Butler, R.P. & Marcy, G.W. 1996, ApJ, 464, L153

Butler, R. P. et al. 2006, ApJ, 646, 505

Campbell, B.E. & Walker, G.A.H. 1979, PASP, 91, 540

Campbell, B.E., Walker, G.A.H. & Yang, S. 1988, ApJ, 331, 902

Campo, C.J. et al. 2011, ApJ, 727, 125

Carter, J.A. et al. 2011, arXiv:astro-ph/1012.0376

Charbonneau, D. et al. 1999, ApJ, 522, L145

Charbonneau, D. et al. 2000, ApJ, 529, L45

Charbonneau, D. et al. 2002, ApJ, 568, 377

Charbonneau, D. et al. 2005, ApJ, 626, 523

Charbonneau, D. et al. 2008, ApJ, 686, 1341

Charbonneau, D. et al. 2009, Nature, 462, 891

Christensen, N. et al. 2001, Classical Quantum Gravity, 18, 2677

Claret, A. 1998, A&A, 335,647.

Cowan, N.B. et al. 2009, ApJ, 700, 915

Cowan, N.B. & Agol, E. 2011, ApJ, 729, 54

Croll, B. 2006, PASP, 118, 1351

Croll, B. et al. 2010a, ApJ, 717, 1084

Croll, B. et al. 2010b, ApJ, 718, 920

Croll, B. et al. in preparation

Croll, B. et al. 2011, AJ, 141, 30

Crossfield, I.J.M. et al. 2010, ApJ, 723, 1436

Cumming, A. et al. 2008, PASP, 120, 531

Cushing, M.C. et al. 2008, ApJ, 678, 1372

Czesla, S. et al. 2009, A&A, 505, 1277

de Mooij, E.J.W. & Snellen, I.A.G. 2009, A&A, 493, L35

de Mooij, E.J.W. et al. 2011, A&A, 528, A49

Deming, D. et al. 2005, *Nature*, 434, 740

Deming, D. et al. 2005b, ApJ, 622, 1149

Deming, D. et al. 2007, MNRAS, 378, 148

Deming, D. et al. 2011, ApJ, 726, 95

Deroo, P., Swain, M.R., & Vasisht, G. 2010, arXiv:astro-ph/1011.0476

Desert, J.-M. et al. 2008, A&A, 492, 585

Desert, J.-M. et al. 2010, arXiv:astro-ph/1008.2481

Desert, J.-M. et al. 2011, ApJ, accepted, arXiv:astro-ph/1103.2370

Desidera, S., Barbieri, M. 2007a, A&A, 462, 345

Devost, D. et al. 2010, Proc. SPIE, Vol. 7737, edited by David R. Silva, Alison B. Peck, B. and Thomas Soifer

Dittman, J.A. et al. 2009, 701, 756

Duquennoy, A. & Mayor, M. 1991, A&A, 248, 485

Durbin, J. & Watson, G.S. 1951, Biometrika, 38, 159

Eastman, J. et al. 2010, PASP, 122, 935

Ellis, S.C. & Bland-Hawthorn, J. 2008, MNRAS, 386, 47

Fabrycky & Tremaine, 2007, ApJ, 669, 1298

Fabrycky, D.C. & Winn, J.N. 2009, ApJ, 696, 1230

Fazio, G.G. et al. 2004, ApJS, 154, 10

Ford, E.B. 2005, AJ, 129, 1706

Fortney, J.J., et al. 2005, ApJ, 627, L69

Fortney, J.J., et al. 2006, ApJ, 642, 495

Fortney, J.J., et al. 2008, ApJ, 678, 1419

Fossati, L. et al. 2010a, ApJ, 714, L222

Fossati, L. et al. 2010b, ApJ, 720, 872

Fressin, F. et al. 2010, ApJ, 711, 374

Gaudi, B. S., Seager, S., Mallen-Ornelas, G., 2005, ApJ, 623, 472

Gaudi, B.S. & Winn, J.N. 2007, ApJ, 655, 550

Gibson, N.P., et al. 2008, A&A, 492, 603

Gibson, N.P. et al. 2010, MNRAS, 404, L114

Gibson, N.P. et al. 2010b, arXiv:astro-ph/1012.0811

Gibson, N.P. et al. 2011, MNRAS, 411, 2199

Gillon, M. et al. 2009, A&A, 506, 359

Glass, I.S. 1999, Handbook of Infrared Astronomy, United States of America, Cambridge University Press

Goldreich, P., Tremaine, S., 1980, ApJ, 241, 425

Griffith, C.A. 1993, Nature, 364, 511

Hansen, J.E. & Travis, L.D. 1974, Space Science Reviews, 16, 527

Hardy, T. et al. 2008, Proc. SPIE, Vol. 7021

Harrington, R. S. 1968, AJ, 73, 190

Hatzes, A.P. et al. 2000, ApJ, 544, L145

Hatzes, A.P. et al. 2003, ApJ, 599, 1383

Hatzes, A.P. et al. 2006, A&A, 457, 335

Hauschildt, P.H. et al. 1997a, ApJ, 483, 390

Hauschildt, P.H. et al. 1997b, ApJ, 488, 428

Hauschildt, P.H. et al. 1999, ApJ, 512, 377

Hebb, L. et al. ApJ, 2009, 693, 1920

Henry, G.W. et al. 2000, ApJ, 529, L41

Herbst, T.M. et al. ApJ, 1994, 106, 1298

Hershey, J.L. et al. AJ, 1973, 78, 421

Holman, M., Touma, J., Tremaine, S. 1997, *Nature*, 386, 254

Houck, J.R. et al. 2004, ApJS, 154, 18

Howard, A.W. et al. 2011, ApJ, submitted, arXiv:astro-ph/1103.2541

Hubeny, I. et al. 2003, ApJ, 594, 1011

Husnoo, N. et al. et al. 2010, arXiv:astro-ph/1004.1809

Ibgui, L. et al. 2010, ApJ, 713, 751

Ida, S., Lin, D. N. C. 2005, ApJ, 626, 1045

Innanen, K. A., Zheng, J. Q., Mikkola, S., Valtonen, M. J. 1997, AJ, 113, 1915

Irwin, J. et al. 2009, ApJ, 701, 1436

Jones, D.H. et al. et al. 1996, 108, 929

Jones, H.R.A., Butler, R.P., Tinney, C.G. et al. 2006, MNRAS, 369, 249

Juric, M. & Tremaine, S., ApJ, 2008, 686, 603

Kirkpatrick, J.D. et al. 1999, ApJ, 519, 802

Knutson, H. et al. 2007, PASP, 119, 616

Knutson, H. et al. 2007b, Nature, 447, 183

Knutson, H. et al. 2008, ApJ, 673, 526

Knutson, H. et al. 2009a, ApJ, 690, 822

Knutson, H. et al. 2009b, ApJ, 691, 866

Knutson, H. et al. 2009c, ApJ, 703, 769

Knutson, H. et al. 2010, ApJ, 720, 1569

Kozai, Y. AJ, 1962, 67, 591

Lai, D. et al. 2010, ApJ, 721, 923

Langton, J. & Laughlin, G. 2008, arXiv:astro-ph/0808.3118

Laughlin, G. et al. 2009, Nature, 457, 562

Latham, D. et al. 1989, Nature, 339, 38

Lecavelier des Etangs, A. et al. 2008, A&A, 481, L83

Leger, A. et al. 2009, A&A, 506, 287

Lester, J.B., & Neilson, H.R. 2008, A&A, 491, 633

Li, S. et al. 2010, Nature, 463, 1054

Liddle, A.R. 2007, MNRAS, 377, L74

Lidov, M. L. 1962, Planet. Space Sci., 9, 719

Lin, D. N. C., Bodenheimer, P., Richardson, D. C. 1996, *Nature*, 380, 606

Liu, X. et al. 2008, ApJ, 687, 1191

Lodders, K. & Fegley, B. 2002, Icarus, 155, 393

Lodders, K. 2002, ApJ, 577, 974

Loeb, A. 2005, ApJ, 623, L45

Loeillet, B. 2008, A&A, 481, 529

Lombardi, G. 2011, et al. arXiv:astro-ph/1102.1214

Lopez-Morales, M. & Seager, S. 2007, ApJ, 667, L191

Lopez-Morales, M. et al. 2010, ApJ, 716, L36

Machalek, P. 2008, ApJ, 684, 1427

Madhusudhan, N. & Seager, S. 2009, ApJ, 707, 24

Madhusudhan, N., & Seager, S. 2010, ApJ, 725, 261

Madhusudhan, N. et al. 2010, Nature, 469, 64

Mandel, K. & Agol, E. 2002, ApJ, 580, L171

Mandell, A.M. et al. 2011, ApJ, 728, 18

Marcy, G.W. et al. 2005, ApJ, 619, 570

Marcy, G.W. & Butler, R.P. 1992, PASP, 104, 270

Marcy, G.W. & Butler, R.P. 1996, ApJ, 464, L147

Marcy, G.W. & Butler, R.P. 2000, PASP, 112, 137

Mather, J.C. et al. 2010, The First Stars and Galaxies: Challenges for the Next Decade, CP 1294, edited by D.J. Whalen, V. Bromm and N. Yoshida

Mayor, M., Queloz, D. 1995, *Nature*, 378, 355

Mayor, M. et al. 2010, A&A, 493, 639

Mayor, M. et al. 2010, A&A, 507, 487

McLaughlin, D.B. 1924, ApJ, 60, 22

McLean, I.S. et al. 2008, SPIE, 7014,

Menou, K. & Rauscher, E. 2009, ApJ, 700, 887

Miller-Ricci, E. & Fortney, J.J. 2010, ApJ, 716, L74

Moreels, G. et al. 2008, Experimental Astronomy, 22, 87

Morton, T.D., Johnson, J.A. 2011, ApJ, 729, 138

Moses, J.I. et al. 2005, JGRE, 110, E8

Naef, D. et al. 2001, A&A, 375, L27

Nagasawa, N. et al. 2008, ApJ, 678, 498

Nettelmann, N. et al. 2011, arXiv:astro-ph/1010.0277v2

Nutzman, P. & Charbonneau, D. 2008, PASP, 120, 317

O'Donovan, F.T. et al. 2006, ApJ, 651, L61

O'Donovan, F.T. et al. 2007, ApJ, 663, L37

O'Donovan, F.T. et al. 2010, ApJ, 710, 1551

Offer, A.R. & Bland-Hawthorn, J. 1998, MNRAS, 299, 176

Palle, E. et al. 2011, ApJ, 728, 19

Papaloizou, J., Lin, D. N. C., 1984, ApJ, 285, 818

Poddany, S. et al. 2010, New Astron., 15, 297

Pollacco, D. et al. 2008, MNRAS, 385, 1576

Pont, F. et al. 2007, A&A, 476, 134

Pont, F. et al. 2007, MNRAS, 385, 109

Pont, F. et al. 2011, MNRAS, 411, 1953

Puget, P. et al. 2004, Proc. SPIE, 5492, 978

Queloz, D et al. 2000, A&A, 359, L13

Queloz, D. et al. 2009, A&A, 506, 303

Rabus, M. et al. 2009, A&A, 494, 391

Raghavan, D. et al. 2006, ApJ, 646, 523

Rages, K. et al. 1999, Icarus, 139, 211

Ragozzine, D. & Wolf, A.S. 2009, ApJ, 698, 1778

Rasio, F. A., Ford, E. B., 1996, Science, 274, 954

Rauscher, E. et al. 2008, ApJ, 681, 1646

Redfield, S. et al. 2008, ApJ, 673, L87

Richardson, L. J., Deming, D., & Seager, S., 2003, ApJ, 597, 581

Rieke, G.H. et al. 2004, ApJS, 154, 25

Rogers, J.C. et al. 2009, ApJ, 707,1707

Rogers, L.A. & Seager, S. 2010, ApJ, 716, 1208

Rossiter, R.A. 1924, ApJ, 60, 15

Rowe, J. F et al. 2008, ApJ, 689, 1345

Sada, P.V. et al. 2010, ApJ, 720, L215

Saumon, D. et al. 2007, ApJ, 656, 1136

Seager, S. & Sasselov, D. 1999, ApJ, 537, 916

Seager, S. et al. 2005a, Astrobiology, 5, 372

Seager, S. et al. 2005b, ApJ, 632, 1122

Shabram, M. et al. 2011, ApJ, 727, 65

Sing, D.K. & Lopez-Morales, M. 2009, A&A, 493, L31

Sing, D.K. et al. 2011, MNRAS, arXiv:astro-ph/1103.0026

Showman, A.P. & Guillot, T. 2002, A&A, 385, 166

Showman, A.P. et al. 2009, ApJ, 699, 564

Snellen, I.A.G. 2005, MNRAS, 363, 211

Snellen, I.A.G. & Covino, E. 2007, MNRAS, 375, 307

Snellen, I.A.G. et al. 2008, A&A, 487, 357

Snellen, I.A.G. et al. 2009, Nature, 459, 543

Snellen, I.A.G. et al. 2010, Nature, 465, 1049

Snellen, I.A.G. et al. 2010b, A&A, 513, 76

Sozzetti, A. et al. 2007, ApJ, 664, 1190

Sozzetti, A. et al. 2009, ApJ, 691, 1145

Spiegel, D.S. et al. 2009, ApJ, 699, 1487

Steinbring, E. et al. 2010, PASP, 122, 1092

Stephens, D.C. et al. 2009, ApJ, 702, 154

Struve, O. 1952, The Observatory, 72, 199

Swain, M.R., Vasisht, G., & Tinetti, G. 2008, Nature, 452, 329

Swain, M.R. et al. 2009a, ApJ, 690, L114

Swain, M.R. et al. 2009b, ApJ, 704, 1616

Swain, M.R. et al. 2010, Nature, 463, 637

Takeda, G., Kita, R. & Rasio, F. A., 2008, ApJ, 683, 1063

Takeda, G., Rasio, F. A., 2005, ApJ, 627, 1001

Tamuz, O. et al., 2008, A&A, 480, L33

Thompson, T.A. et al. 2005, ApJ, 630, 167

Tinetti, G. et al. 2007, Nature, 448, 169

Tinetti, G. et al. 2010, ApJ, 712, L139

Todorov, K. et al. 2010, ApJ, 708, 498

Tomasko, M.G. et al. 2008, Icarus, 56, 669

Torres, G. et al. 2008, ApJ, 677, 1324

Triaud, A. et al. 2010, A&A, 524, 25

Trilling, D. E., Benz, W., Guillot, T., Lunine, J. I., Hubbard, W. B., Burrows, A., 1998, ApJ, 500, 428

Udry, S. 2007, A&A, 469, L43

van de Kamp, P. 1969, AJ, 74, 757

van de Kamp, P. 1982, Vistas in Astronomy, 26, 141

Walker, G.A.H. et al. 1992, ApJ, 396, L91

Walker, G.A.H. et al. 1995, Icarus, 116, 359

Walker, G.A.H. 2008, arXiv:astro-ph/0812.3169

Ward, W. R., 1986, Icarus, 67, 164

Winn, J. N et al. 2008a, ApJ, 683, 1076

Winn, J. N et al. 2008, AJ, 136, 267

Winn, J. N et al. 2009, ApJ, 693, 794

Wolszczan, A. & Frail, D.A. 1992, Nature, 355, 145

Wolszczan, A. 1994, Science, 264, 538

Wright, J.T. et al. 2007, ApJ, 657, 533

Wu, Y., & Lithwick, Y. 2010, arXiv:astro-ph/1012.3475

Wu, Y., & Murray, N. 2003, ApJ, 589, 605

Wu, Y., Murray, N., & Ramsahai, J.M. 2007, ApJ, 670, 820

Youdin, A. N, & Mitchell, J.L. 2010, ApJ, 721, 1113

Zahnle, K. et al. 2009, ApJ, 701, 20

Zahnle, K., Marley, M.S., & Fortney, J.J. 2009, ApJ submitted, arXiv:astro-ph/0911.0728.

Zboril, M. 2003, Astronomische Nachrichten, 324, 527